UNIVERSITAT DE BARCELONA

Guiding active particles through surface interactions

Jaideep Katuri

UNIVERSITAT DE BARCELONA

Guiding active particles through surface interactions

Jaideep Katuri

A thesis submitted for the degree of

Doctor of Philosophy

Barcelona, 2018

Directors: Dr. Samuel Sánchez and Dr. Ignacio Pagonabarraga

Tutor: Dr. Giancarlo Franzese

The research described in this thesis was carried out in the group 'Smart nano-bio-devices' at the Max Plank Institute for Intelligent Systems in Stuttgart, Germany and Institute for Bioengineering of Catalonia, Barcelona, Spain.

Contents

List of figures 7

Abstract 13

1. Introduction 19

1.1 Emergent behaviour in active matter systems 22

1.2 Minimal models to capture collective behaviour 24

1.3 Collective behaviour in artificial active matter systems 28

1.4 Boundary induced effects in active matter systems 30

1.5 Hydrodynamic interactions of self-propelled particles with surfaces 33

1.6 Self-propulsion at the microscale 37

1.7 Motion mechanisms in biological micro-swimmers 42

1.8 Interfacial transport 46

1.8.1 Electrophoresis 47

1.8.2 Diffusiophoresis 51

1.8.3 Self-phoresis of colloidal particles 55

2. Interaction of phoretic micro-swimmers with surfaces 66

2.1 Introduction 67

2.2 Results 71

2.2.1 Orientation of phoretic Janus micro-swimmers at planar walls71

2.2.2 Orientation of phoretic Janus active particles close to side steps 76

2.2.3 Effects of the step height on the capture efficiency..... 81

2.2.4 Guidance of active particles by low-height topographic steps 82

2.3 Discussion and further experiments..... 87

2.4 Concluding remarks 91

2.5 Appendix A: Preparation of Janus particles and microstructures used for guidance experiments..... 93

2.6 Appendix B: Notes on theoretical modelling..... 95

3. Directed flow of active particles through alignment interactions 99

3.1 Introduction 100

3.2 Results..... 110

3.2.1 Active particles in symmetric structures..... 113

3.2.2 Active particles in triangular channels..... 114

3.2.3 Directed flow of active particles in asymmetric channels 117

3.2.4 Accumulation of active particles using linear ratchet structures 121

3.3 Minimal model and discussion..... 124

3.4 Concluding Remarks 128

3.5 Appendix A: Dependence of particle flow on material and chemical properties of the surface 130

3.6 Appendix B: Effect of opening width of channels and jamming 132

4. Cross-stream migration of active particles in external flow 135

4.1 Introduction 136

4.2 Results 146

4.2.1 Active particles without external flow 146

4.2.2 Passive particles in external flow 148

4.2.3 Active particles in external flow 150

4.3 Construction of theoretical model 156

4.3.1 Comparison with experimental trajectories 161

4.4 Concluding remarks 166

4.5 Appendix A: Tracking of Janus particles 168

4.6 Appendix B: Theoretical calculation of particle velocity 170

5. Conclusions and final remarks 174

5.1 Towards understanding chemiosmotic flows 176

5.2 Assembling colloidal crystals with active particles 183

5.3 Engineering new responses of active particles 184

5.4 Beyond solid interfaces 186

6. Resumen en español 188

7. References 198

List of figures

Figure 1: Emergence of orientational order. 22

Figure 2: Physics of Vicsek model. 26

Figure 3: Emergent behaviour in artificial active matter systems. 28

Figure 4: Accumulation of biological micro-swimmers close to surfaces. 31

Figure 5: Dynamics of self-propelled rods close to surfaces. 32

Figure 6: Hydrodynamic interactions of self-propelled particles with surfaces. 34

Figure 7: Control of active matter through surface properties. 36

Figure 8: Life at low Reynolds number. 39

Figure 9: Swimming at low Reynolds number. 41

Figure 10: Non-reciprocal motion mechanisms employed by biological micro-swimmers. 42

Figure 11: Artificial swimmers mimicking the motion mechanism of biological micro-swimmers. 44

Figure 12: Schematic representing the origin of electro-osmotic flow close to charged surface 47

Figure 13: Schematics representing the origin of diffusiophoretic flow close to a surface in the presence of a gradient of solvent molecules. 51

Figure 14: Diffusiophoretic migration of colloids. 55

Figure 15: Schematic of a colloidal sphere undergoing self-diffusiophoresis. 56

Figure 16: Schematic of different propulsion regimes predicted for a self-diffusiophoretic Janus particle dispersed in a peroxide solution..... 60

Figure 17: Self-phoretic particles. 62

Figure 18: Active Brownian particles in two dimensions. 64

Figure 19: Interaction of biological micro-swimmers with walls. 67

Figure 20: Wall-entrapment of bacteria close to surfaces. 69

Figure 21: Scattering of Chlamydomonas from surfaces. 70

Figure 22: Experimentally measured probability distribution of θ for active particles. 73

Figure 23: Interactions of phoretic Janus particles with surfaces..... 74

Figure 24: The phase portrait obtained from numerical simulations for a bottom-heavy particle 76

Figure 25: Interactions of phoretic Janus particles with a side step. 76

Figure 26: An active Janus particle approaching a step. 78

Figure 27: Phase portrait similar to the one in Figure 24, but in absence of gravity. 80

Figure 28: A summary of the crossing behaviour of Janus SiO_2-Pt particles of different sizes at several values of h_{step} 81

Figure 29: Janus particle trajectories close to topographical steps..... 84

Figure 30: Trapping of phoretic Janus particles around cylindrical posts..... 85

Figure 31: Schematic representation of the two possible docking events leading to a Janus particle stably propelling the microgear.[152] 88
Figure 32: Self-assembly of phoretic Janus particles around inert micro-gear structures 89
Figure 33: Change in angular speed (circles) of the microgear 90
Figure 34: Lithography based creation of patterns. 95
Figure 35: Feynman's ratchet composed of a ratchet engaged to a pawl and a spring 100
Figure 36: Schematic illustration of a flashing ratchet. 102
Figure 37: Rocking ratchet 104
Figure 38: Transport of colloidal particles in bacterial baths 105
Figure 39: Wall of funnels separate motile bacteria. 107
Figure 40: Stationary probability density of particle position in a channel compartment for particles with frictionless collisions at the walls[177]. 108
Figure 41: Self-propelled Janus particles on surfaces with topographical features. 111
Figure 42: Dynamic of self-propelled Janus particles on surfaces with potential wells. 113
Figure 43: Self-propelled Janus particles in symmetric channels. 114
Figure 44: Self-propelled Janus particles in triangular channels. 115
Figure 45: Self-propelled Janus particles in triangular channels with rounded corners. 117

Figure 46: Circular flow of active particles inside periodic ratchet-like structures. 118
Figure 47: Alignment and release of active particles influenced by topographical features. 119
Figure 48: Accumulation of active particles using linear ratchet structures. 121
Figure 49: Trajectories of active particles accumulated over different time lengths 122
Figure 50: Orientational locking of active particles in confined spaces 123
Figure 51: Directed flow of colloidal rollers in racetrack structures. 128
Figure 52: Snapshot of an experiment with self-propelled Janus particles in a ratchet structure coated with a layer of Ti. 131
Figure 53: Schematic illustrating the self-diffusiophoretic and chemiosmotic mechanisms that drive the motion of a chemical active particle 132
Figure 54: Jamming of self-propelled particles at channel openings 133
Figure 55: Bacterial chemotaxis. 137
Figure 56: System with position dependent variation of propulsion velocity. 138
Figure 57: Gravitaxis in natural and artificial micro-swimmers. 139
Figure 58: Microorganisms in flow. 140
Figure 59:Directional response of micro-swimmers to flow. 142
Figure 60: Schematic illustration of the model system. 144
Figure 61: Active particles without flow 146
Figure 62: Flow profile in the microfluidic channel. 148

Figure 63: Passive silica-Pt particles in a flow 150

Figure 64: Active particles in a flow. 151

Figure 65: Angular probability distributions of active colloidal particles in the absence of an imposed flow..... 152

Figure 66: Experimental and numerically obtained trajectories of active particles in a flow..... 153

Figure 67: Effect of particle radius on the cross-stream behaviour. 154

Figure 68: Effect of Vp on the cross-stream migrations behaviour..... 156

Figure 69: Schematic of the contributions to planar alignment steady state. 159

Figure 70: Schematic illustration of the three fixed point solutions to Eqs. 47-50..... 160

Figure 71: Dependence of $|\cos(\varphi^*)|$ on V^*..... 161

Figure 72: Numerically obtained trajectories of inactive and active particles in flow. 162

Figure 73: Phase portraits of inactive and active particles in flow..... 165

Figure 74: Brownian Dynamics Simulations. 166

Figure 75: Automated tracking of the orientation angle of Janus particles.. 169

Figure 76: Interactions of passive particles with motile active particles..... 178

Figure 77: Depletion zones formed behind an active particle in dense suspensions of passive particles. 179

Figure 78: Interactions of passive particles with active particles in a cap-down orientation. 180

Figure 79: Towards colloidal crystals using topographical structures.....184

Abstract

Active matter refers to systems composed of active units, each capable of transducing energy from its local surrounding into self-propulsion or to exert mechanical force. Due to the sustained energy uptake and dissipation at the scale of the active unit, these systems are constantly out-of-equilibrium and exhibit a number of exotic phenomenon that are inaccessible in systems at thermal equilibrium. Examples of active matter span multiple length scales, from the sub-cellular range of the cytoskeleton, where stresses and polymerization kinetics are held away from equilibrium by a plentiful supply of chemical fuel, to the micron scales of suspensions of motile micro-organisms such as bacteria which exhibit swarming and create vortices arising from their self-propulsion. More familiar examples include groups of birds which can display remarkable flocking behaviours and fish schools whose motion is dominated by collective effects.

There are two common themes that run through all these active matter systems. The first is the emergence of correlated collective phenomenon through particle-particle interactions, as exemplified in flocking of birds, swarming of bacteria, and crystallization of self-propelled particles. And the second is the ability of the active units to interact with their surroundings through self-propulsion. Common examples of this include chemotaxis and rheotaxis, observed in many biological active matter systems such as bacteria,

sperms and algae. Several studies have already reported on the collective effects in these systems. In this thesis, I will discuss results obtained from conducting experiments to understand the latter; the case of active particle interactions with its local environment.

As a model active matter system, we use a system of colloidal active particles, that propel due to self-diffusiophoresis. These particles coated with two dissimilar materials on each half are referred to as Janus particles. In a solution of H_2O_2, one side of the colloidal particle has catalytic properties (Pt), while the other half remains inert (SiO_2). This creates a concentration gradient of the reaction product along the surface of the particle and induces a phoretic slip, which propels the particle. Our experiments necessarily involve studying and understanding the dynamics of these self-phoretic particles close to surfaces. Chapter 1 includes a comprehensive general introduction to active matter systems and this artificial self-phoretic system in particular.

It has been observed in a number of biological active matter systems that confining walls introduce an accumulation effect. This accumulation effect can either arise simply as a result of statistical mechanics (self-propelled particles have a lower velocity when confined by a surface than in the bulk, increasing their positional probability distribution close to the surface), or due to active interactions, such as through hydrodynamic effects resulting from flagellar beat patterns near walls, which restricts the orientational degrees of freedom close to a surface and 'traps' the particles there.

In our experiments using spherical self-propelled particles, we find that hydrodynamic and phoretic effects combine to strongly restrict the particle's orientation to be parallel to the surface, effectively trapping them there. With this result, we show that wall accumulation effects, ubiquitous in biological active matter systems and often thought to arise from the complex hydrodynamic interactions of the beating flagella with the surface, also exist in simple artificial active matter systems composed of spherical particles. The accumulation effect is in fact stronger due to the role of active aligning induced by the phoretic field around the particle. The observed phenomenology is qualitatively captured by a simple continuum model of self-diffusiophoresis near confining boundaries, developed by our collaborators in Max Plank Institute for Intelligent Systems, Stuttgart, indicating that the chemical activity and associated hydrodynamic interactions with the nearby topography are the main physical ingredients behind the observed effect.

We further exploit this alignment effect to create a guidance system for self-propelled Janus particles. Achieving control over the directionality of active colloids is essential for their use in practical applications, such as cargo carriers in microfluidic devices. So far, guidance of spherical Janus colloids was mainly realized using specially engineered magnetic multilayer coatings combined with external magnetic fields. We demonstrate here that step-like sub-micrometre topographical features can be used as reliable docking and guiding platforms for chemically active spherical Janus colloids. For various

topographic features, docking of the colloid at the feature edge is robust and reliable. Furthermore, the colloids move along the edges for significantly long times, which systematically increase with fuel concentration. Chapter 2 contains the details of these experiments and the corresponding discussion.

We next develop a micron-scale system capable of scaling this guidance effect to a population level, and in order to control the polarity of active particle migration. To achieve control over naturally diffusive, out-of-equilibrium systems composed of self-propelled particles, such as cells or self-phoretic colloids, is a long-standing challenge in active matter physics. The inherently random motion of these active particles can be rectified in the presence of local and periodic asymmetric cues given that a non-trivial interaction exists between the self-propelled particle and the cues. Here we exploit the phoretic and hydrodynamic interactions of synthetic active particles with local topographical features to break the time-reversal symmetry of particle trajectories and to direct a macroscopic flow of particles. We then show that the orientational alignment induced on the active particles by the topographical features, together with their geometrical asymmetry, are crucial in generating directional particle flows. We specifically account for the alignment effect in designing the asymmetric topographical features to optimize the generated particle flow. We also show that our system can be used to concentrate diffusing active particles in confined spaces and identify the interactions responsible for this effect. Overall, this system allows for

robust control over both temporal and spatial distribution of synthetic micromotors and is discussed in Chapter 3.

In Chapter 4 we study the effect of an imposed flow on artificial active particles close to surfaces. For natural micro swimmers, the interplay of swimming activity and external flow can promote robust directed motion, for example, propulsion against (upstream rheotaxis) or perpendicular to the direction of flow. These effects are generally attributed to their complex body shapes and flagellar beat patterns. Using catalytic Janus particles as a model experimental system, we report on a strong directional response that occurs for spherical active particles in a channel flow. The particles align their propulsion axes to be nearly perpendicular to both the direction of flow and the normal vector of a nearby bounding surface. We show that this directional response is sensitive to both the magnitude of fluid flow and particle propulsion velocity. Deterministic theoretical modelling of spherical active particles near a planar wall that captures the experimental observations shows how the directional response emerges from the interplay of shear flow and near-surface swimming activity.

Finally, in Chapter 5, I will summarize the important conclusions from all the experimental work that was carried out during the course of this thesis and share some thoughts on the directions in which this work will progress going into the future

1.Introduction

Living organisms and systems are continually converting energy, either internally stored or transduced from their surroundings, into motion. This activity, and the resulting self-propulsion constantly push these biological systems out of thermal equilibrium. A number of exotic phenomenon result from the intrinsic non-equilibrium nature of these living systems that are not accessible in a system at thermal equilibrium. In recent years, these ubiquitous non-equilibrium systems have come to be classified as *active matter*.

Active matter, by definition, refers to systems composed of *active units*, each capable of converting ambient or stored energy into systematic movement[1]. *Active units* are in contrast with *driven particles*, which are also propelled, but derive their energy from an external source, such as an applied electric or magnetic field, and move in a co-ordinate set by this external field. The directionality of the propulsion in active units is set by an internal co-ordinate of the particle, such as an intrinsic anisotropy. A number of active units, for example, are elongated which sets the directionality of their motion.

Examples of active matter systems abound in nature, and span multiple length scales, ranging from the sub-micrometre, with microtubules associated with motor proteins[2,3], to the micrometre length scales of bacteria[4–6], and the meter-length scales of greater familiarity, such as that of fish[7–9] and birds[10–12]. In each of these systems, the energy that drives the active unit out of equilibrium is derived locally, and together with the resulting self-propulsion, each particle modifies the local environment around it. If the other active units

within the system can sense these modifications in the environment, they can interact with each other through the medium in which they exist. It is through these interactions that many of exotic phenomenon observed in these systems emerge, such as the swarming of bacteria, schooling of fish and flocking of birds[13–22].

1.1 Emergent behaviour in active matter systems

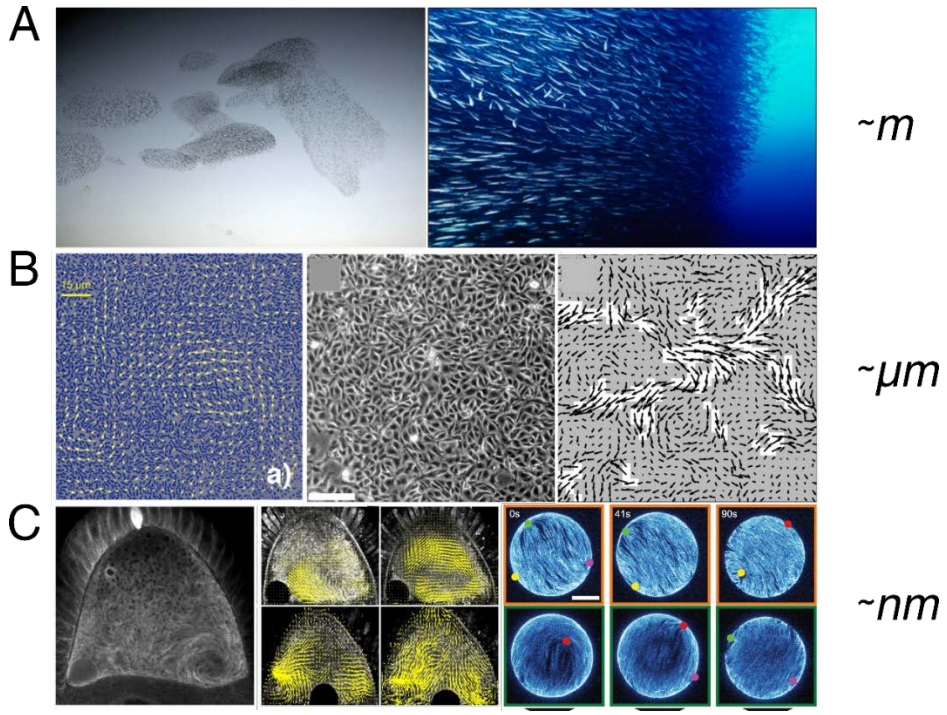

Figure 1: Emergence of orientational order. (**A**). Macroscopic examples of flocks of birds[12] and schools of fish[23]. (**B**). Emergent behaviour in active matter at the microscale as evident in dense bacterial suspensions (left)[24] and epithelial cell sheets (middle and right)[25]. (**C**). Active matter at the sub-micrometre scale where collective patterns emerge in cytoplasmic streaming in an oocyte of Drosophila melanogaster (left)[26] and bundles of microtubules associate and move due to the translation of myosin motors along the microtubule assemblies(right)[27].

A common theme that runs through all active matter systems seems to be that of orientational order. The interactions of active particles with each other and the medium in which they exist gives rise to correlated collective phenomenon. These collective phenomena, much like the active units themselves, also span multiple length scales, ranging from the emergence of polar order in dense concentration of biofilaments, to swarms and vortices of bacteria, and flocking

in birds (Figure 1). An understanding of the emergence of these correlated phenomena has relevance for many biological processes like intracellular transport[28], the migration of epithelial cells in tissue formation and wound healing[29–32], or the collective motion of spermatozoa during reproduction[33].

Biological active matter systems are, however, necessarily complex, their characteristics intricately linked with their local physiological and chemical environments and are hard to probe experimentally. And even in systems which are accessible experimentally, it is difficult to distinguish if the resulting collective phenomenon arises as a consequence of some biological stimuli, or is a purely physical phenomenon, or a combination of both. It is due to the absence of a model experimental system and since there exists a very large parameter space to be probed in active matter systems, that they have attracted considerable attention in theory and simulations. The geometry of the active particles, strength of self-propulsion, the interactions between the active particles and the medium through which they interact can all influence the collective behaviour observed in these systems, making them ideal candidates for numerical modelling[34].

Besides, the ubiquitous nature of ordered collective phenomenon at all the different length scales of biological systems hints at the existence of universal features shared among all these systems, that is indifferent to the specific properties of the individual active units. Such universal features are attractive to be captured in minimal models that neglect the specific details of the

systems but rather contain only the basic features necessary to characterize the problem.

1.2 Minimal models to capture collective behaviour

This section has been inspired from 35

The simplest and perhaps the most well-known of these minimal models that captures the collective phenomenon arising from the interactions between individual active units is the *Vicsek model*[18,35]. The model describes the *over damped* dynamins of *N* interacting self-propelled particles characterized by their position $\mathbf{r}_i^t$ and their direction of motion $\mathbf{s}_t^i$, a unit vector $|\mathbf{s}_i^t| = 1$. Here i is the particle index $i = 1, 2, \ldots\ldots N$, and t denotes time labels. In the simplest version of the model, all the particles move with the same velocity v_0, and according to time discreet dynamics

$$\boldsymbol{r}_i^{t+\Delta t} = \boldsymbol{r}_i^t + \Delta t v_0 \boldsymbol{s}_i^{t+\Delta t} \tag{1}$$

so that the orientation $\mathbf{s}$ and velocity $\mathbf{v} = v_0 \boldsymbol{s}$ coincide.

The interaction between the particles in the model is introduced through the simple condition that the particles tend to align their direction of motion with their *local* neighbours. The particle orientation $\mathbf{s}_i^t$ depends on the average orientation of all the particles in the spherical neighbourhood S_i of radius R_0 centred on i (Figure 2). This tendency to align with the local neighbours is hampered by a noise term which plays a role analogous to temperature in an equilibrium system, given by ξ_i^t. In a 2-dimensional system, the direction of

motion of the particles is defined by a single angle θ_i^t with $\mathbf{s} = (\cos\theta, \sin\theta)$ and the orientation dynamics can be written as

$$\theta_i^{t+\Delta t} = Arg\left[\sum_j n_{ij}^t \mathbf{s}_j^t\right] + \eta\xi_i^t \tag{2}$$

where ξ_i^t is a zero average, delta correlated scalar noise

$$\langle\xi_i^t\rangle = 0, \langle\xi_i^t\xi_j^k\rangle \sim \delta_{tk}\delta_{ij} \tag{3}$$

uniformly distributed in $[-\pi,\ \pi]$ and the function Arg returns the angle defining the orientation of the average vector $\sum_j n_{ij}^t \mathbf{s}_j^t$, and n_{ij}^t is the connectivity matrix,

$$n_{ij}^t = \begin{cases} 1 \text{ if } \left|\mathbf{r}_i^t - \mathbf{r}_j^t\right| < R_0 \\ 0 \text{ if } \left|\mathbf{r}_i^t - \mathbf{r}_j^t\right| > R_0 \end{cases} \tag{4}$$

This method of choosing neighbours to align with is referred to as *metric* since the alignment condition is dependent on R_0 (Figure 2B). The alternative to this would be to choose interacting particles based on some (metric free) topological rules, such as the nearest n_c neighbours[12].

One can of course choose a set of convenient space and time units such that $\Delta t = R_0 = 1$ and the model behaviour then becomes dependent only on three control parameters: the amplitude of noise η, the particle speed v_0 and the total density of particles $\rho_0 = N/V$, where V is the volume of the system.

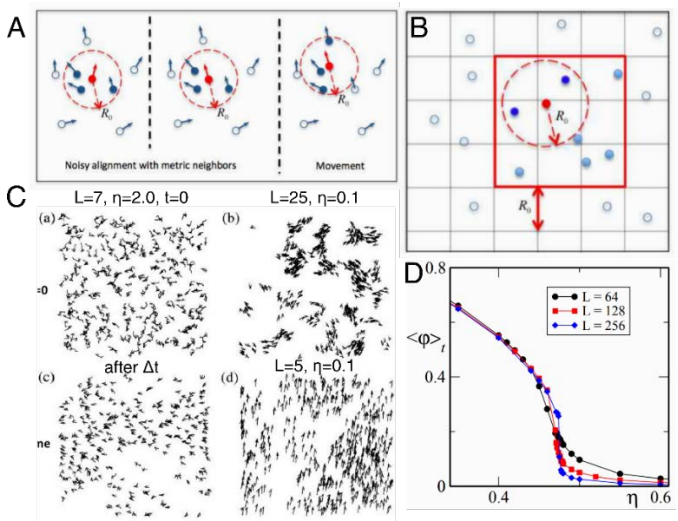

Figure 2: Physics of Vicsek model. (**A**) Interaction rules applied in the Vicsek model that leads to flocking behaviour of self-propelled particles under certain conditions.[35] (**B**) Molecular dynamics implementation of the Vicsek model.[35] (**C**) Velocity vectors of particles displayed as a function of varying values of density and noise [Adapted from 18]. (**D**) Characteristic order parameter curves vs. noise amplitude for fixed density and different system sizes[36].

Numerical simulations of the Vicsek model, under the right conditions, display a transition from disorder to ordered collective motion. For instance, when the amplitude of noise η is reduced below a certain threshold level, particles start to synchronize their orientation and move together (Figure 2C). The easiest way to numerically capture this transition from disorder phase to ordered phase is through the finite polar order parameter

$$\varphi(t) = \frac{1}{N}\sum_{i=1}^{N} \mathbf{s}_i^t \tag{5}$$

At high noise levels, the self-propelled particles are unable to synchronize their orientations which cancels out $\sum_i \mathbf{s}_i$. At lower amplitudes of noise, the particles

are able to synchronize their orientations with each other and φ tends towards 1 (Figure 2D)[21,36].

A simple way to understand the onset towards collective behaviour is to consider that in order for all the particles to synchronize with each other in a system, information has to propagate throughout the system. An alignment interaction that occurs when a particle is in proximity of another particle creates such information, while noise destroys this information. So, another effective way to increase the creation of information in the system is to increase the frequency of particle-particle encounters while keeping the noise constant. This can be achieved by increasing the number of particles in the system. A transition to ordered phase therefore occurs also by increasing the particle density ρ in the system but keeping the noise amplitude fixed. This transition to ordered phase on increasing particle density is in fact what is often observed in biological systems such as in swarming bacteria or flocking birds.

1.3 Collective behaviour in artificial active matter systems

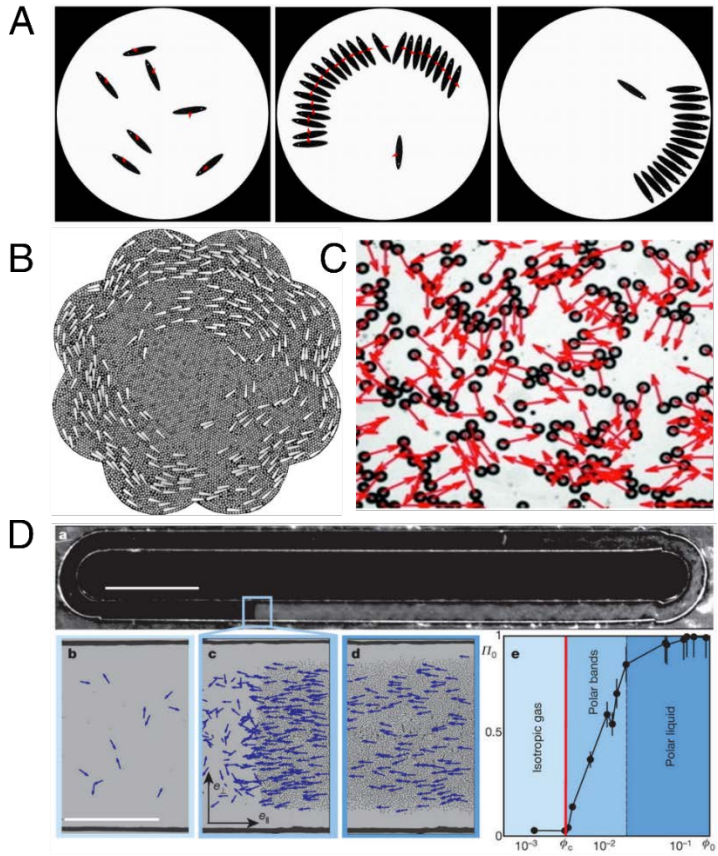

Figure 3: Emergent behaviour in artificial active matter systems. (**A**) Experimental realization of collective behaviour in Bristle bots, (left- right): disordered (random) motion of spinners at lowdensity; swirlingmotion of spinners at high density and stasis of walkers at high density[37]. (**B**) A monolayer of millimetre-sized tapered brass rods align spontaneously on a vibrating surface amidst a background of aluminium beads[38]. (**C**) Emergence of swarming behaviour in self - propelled micr o droplet systems[39]. (**D**) Transition to directed motion in high density suspensions of colloidal rollers[40].

In the last decade, several artificial active matter systems have been created that share the basic properties of their biological counterparts, as in, they consume energy locally, either on board or transduced from their immediate

surroundings, are self-propelled, and have an internal co-ordinate system that dictates their directionality of motion. Much like their biological counterparts these artificial particles have also been shown to interact with each other leading to collective motion.

The onset of orientational order has been demonstrated in systems of artificial active matter at different scales. Giomi *et al.* showed that a system of macroscopic self-propelled Bristle-Bots, simple automata made from a toothbrush and powered by an onboard cell phone vibrator-motor, undergoes transitions form a disordered phase to swirling motion to eventually statis depending on the density of bots (Figure 3A) [37]. In a system of millimetre-sized tapered rods, rendered mobile due to contact with an underlying vibrating surface and interacting through a medium of spherical beads Kumar *et al.* demonstrated a transition to a globally ordered moving state in the presence of a high density of motile rods and spherical beads (Figure 3B)[38]. Using droplets of a few hundred microns, Thutupalli *et al.* showed that swarming behaviour cam emerge in systems with a high density of the droplets (Figure 3)[39]. At the micron-scale, using a system of artificial active matter composed of colloidal 'rollers', Bricard *et al.* showed that local alignment interactions that exist between particles mediated through electrostatic and hydrodynamic interactions were sufficient to promote the emergence of collective motion either in the form of a macroscopic 'flock' at low particle densities, or in the form of a homogeneous polar phase in the case of high particle densities

(Figure 3D)[40]. Similar transitions to spontaneous flows have also been demonstrated in systems of biologically derived micro-tubules associated with motor proteins[41]. Another common collective effect observed in artificial colloidal active particle systems is the spontaneous transition into crystalline phase[42–46].

1.4 Boundary induced effects in active matter systems

The Vicsek model is often implemented with periodic boundary conditions since one is typically interested in the bulk properties of the active matter system. While convenient, this makes for an artificial setting, since several biological active matter systems exist close to interfaces.[47] In fact, surfaces have been shown to play an important role in a number of biological processes. Bacteria, for example, can only form bio-films and colonies when close to surfaces indicating the importance of active unit-surface interactions alongside particle-particle interactions[48,49]. Surface interactions are also important in the case of fish sperms, as they can only enter the egg at a specific point, the micropyle, and hence have to locate it on the surface[50]. Human and mice sperm cells need to propel close to the surface as well in order to be able to swim against flows in the oviduct[51]. Besides, much like the emergence of collective behaviours, surface induced effects seem to be universal in active matter systems.

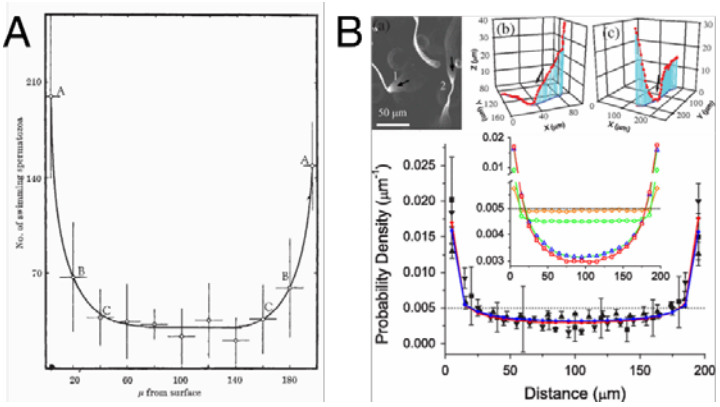

Figure 4: Accumulation of biological micro-swimmers close to surfaces. (**A**) Distribution of motile sperm population as a function of distance from the surface[52]. (**B**) 3D trajectories of Caulobacter swarmer cells swimming near a glass surface and their probability density as function of distance from the wall[53].

Lord Rothschild discovered in 1963, that live sperm cells accumulate at surfaces while dead cells do not (Figure 4A)[52]. This hints towards the fact that an attractive interaction at interfaces is introduced by the activity of the system, which cannot otherwise be explained by classical attractive interactions, such as electrostatic or van der Waals interactions, or through biological interactions, such as receptor-ligand binding. Similar surface accumulation effects have since been observed in other biological active particles like the bacteria *C. crescentus* and *E. Coli* (Figure 4B)[53–56]. These observations indicate towards the fact that surface induced effects such as particle accumulation might be a generic phenomenon existing across different active matter systems and calls for a general physical description like in the case of collective behaviour in active matter systems.

The obvious way in which active particles interact with walls in a confined system is through self-propulsion. A self-propelled particle in the bulk will eventually encounter a confining wall and collide with it. This active particle is typically subject to noise and therefore has some limited orientational persistence, i.e, it keeps pushing in the same direction for some time related to the inverse rotational diffusion coefficient. During this time, the particle remains close to the wall, increasing the particle density close to the wall. The wall accumulation effect then is a competition between the strength of self-propulsion and orientational fluctuations (Figure 5A)[57].

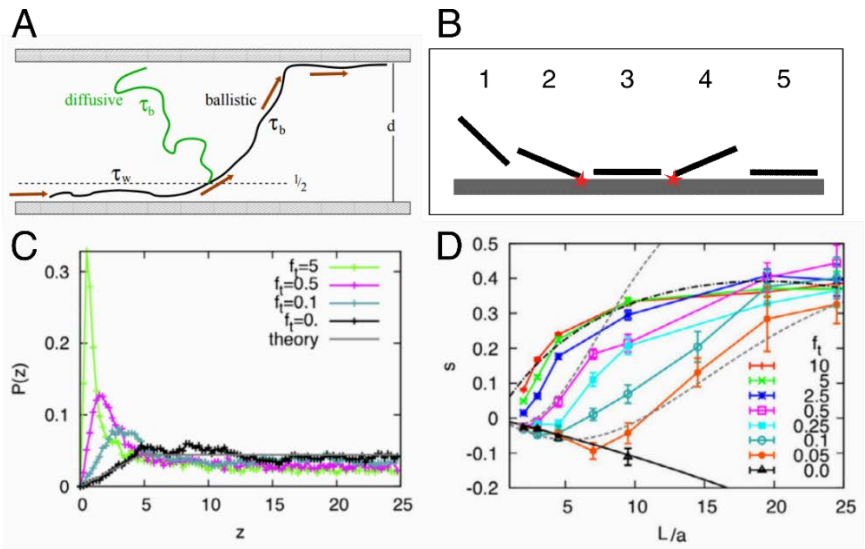

Figure 5: Dynamics of self-propelled rods close to surfaces. (**A**) Schematic representation of the different regimes of rod motion, near a wall for time τ_w and in the bulk for time τ_b, either in the ballistic or in the diffusive regime[57]. (**B**) A self-propelled rod hits a hard surface in an oblique angle head first and gets aligned parallel to it (steps 1 to 3). Rotational diffusion lets the rod turn away from the wall, but it is suppressed to some degree because while turning away the rear end of the rod hits the wall. Adapted from [58]. (**C**) Probability density P(z) as function of the distance z from the surface, for

various propelling forces[57]. (**D**) Surface excess as a function of scaled rod length for various propelling forces[57].

It is interesting to consider the case of rod shaped particles, since many biological active particles mentioned above fit this geometrical description. In the case of passive rods, very close to the wall, the particles have access to fewer orientational confirmations, leading to entropic repulsion from the wall. Brownian dynamic simulations in fact show the depletion of particle density in the case of passive rods. Active rods on the other hand show the opposite effect, accumulating near boundaries (Figure 5C)[57]. When an active particle approaches the confining wall at an oblique angle as shown in Figure 5B, it hits the wall head first. The resulting torque aligns the rod parallel to the surface and the particle continues propelling along the wall. Now, in the absence of orientational noise, the rod would continue moving along the wall forever. But in the presence of a noise term, the particle eventually turns away from the wall. However, the rotational freedom of this event is limited by the rear end of the rod hitting the wall, increasing the time the rod stays at the wall (Figure 5B). It has also been shown that the probability density at the wall increases with growing propulsion force (Figure 5D).

1.5 Hydrodynamic interactions of self-propelled particles with surfaces

Apart from the wall accumulation effect arising through self-propulsion, the medium in which the active particles exist also plays a key role in determining

the confinement induced effects in active matter systems. For systems that exist in liquid media, like many of the active matter systems at the micron and sub-micron scale, hydrodynamic interactions influence the behaviour of active particles close to surfaces[55]. Since no external force is applied on active particles the total interaction force of the self-propelled particle on the fluid and *vice versa* is zero. In the simplest case, which applies to many biological active particles such as motile bacteria, sperms or algae, the far field hydrodynamics can be well described by a force dipole[59]. Two classes of this dipole force exist, determined in part by the physiological features of the biological active particle. The first is the case that occurs for bacteria and sperm where the propelling motor (flagella) is at the back and the passive body is at the front[60]. The passive body pushes the liquid along as it propels, and the particle is referred to as a pusher. In the case of algae, the propelling motor is at the front and the passive body at the back pulls liquid with it as the particle propels and is referred to as puller (Figure 6A)[61,62].

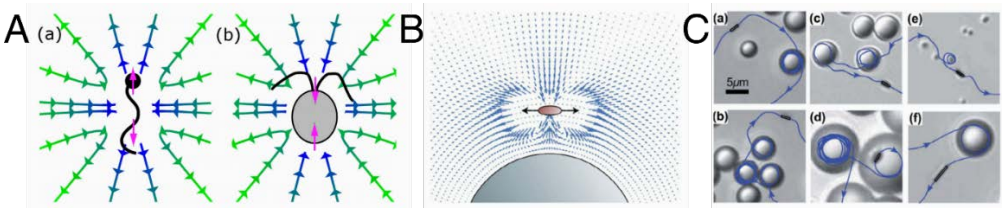

Figure 6: Hydrodynamic interactions of self-propelled particles with surfaces. (A) Schematics of flow fields of dipole swimmers. (left) pushers. (right) pullers.[63] (B-C) Trapping of self-propelled rods by large colloidal particles due to hydrodynamic interactions[64,65].

The magnitude of the flow field around the active particle is measured by dipole strength P, which is given by the product of dipole length and its force. The dipole force of a sperm for example can be estimated from the friction force of the whole body which balances the (pushing) propulsion force generated from the tail and is proportional to $\eta v L$ where v is the propulsion velocity, η is the fluid viscosity and L is the length of the particle. The dipole strength then scales as

$$P \sim \eta v L^2 \tag{6}$$

For an active particle far away from a surface, an analytical expression (far-field approximation) for the torque and drag velocity towards the surface can be obtained. Considering a particle with an orientation angle θ of the dipole with respect to the vertical z direction, the induced velocity at distance z away from the surface is given by[55]

$$u_z(\theta, z) = -\frac{3P}{64\pi\eta z^2}(1 - 3\cos^2\theta) \tag{7}$$

For the case of a pusher, like a bacteria or sperm, this implies that the hydrodynamic interaction is attractive if the particle is oriented nearly parallel to the wall (θ close to 90°) but becomes repulsive if the particle is oriented perpendicular to the wall. This attractive drift towards the surface is proportional to the propulsion velocity and to $\left(\frac{z}{L^2}\right)$. This hydrodynamic interaction also introduces a torque which always tends to align the pushers parallel to the surface where the hydrodynamic drift velocity is attractive (Figure 6B). This attractive interaction has been shown to persist even for

curved walls.[64] Takagi *et al.* have in fact experimentally demonstrated the attraction of self-propelled rod shaped particles to large colloidal spheres arising from hydrodynamic interactions (Figure 6C)[65].

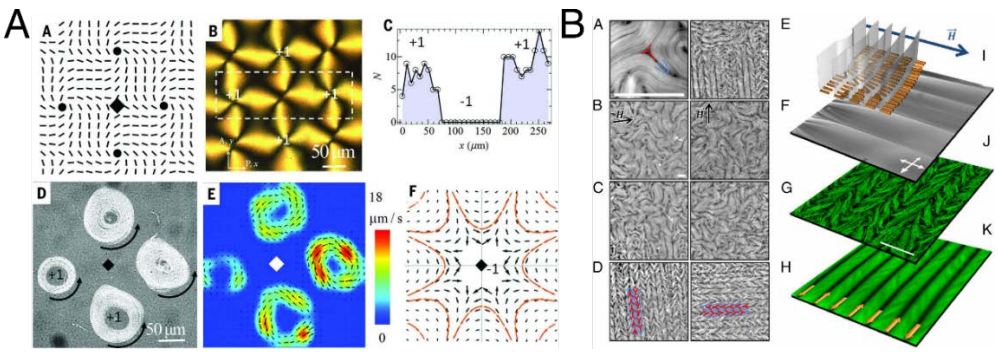

Figure 7: Control of active matter through surface properties. (**A**) Unipolar circular flows of bacteria on periodic patterns of liquid crystal defects[66]. (**B**) Alignment of active nematic flows composed of self-propelled microtubules via magnetic fields[67].

It is likely through a combination of the effect of self-propulsion and the hydrodynamic interactions that most active particles tend to accumulate near surfaces and the strength of these roles is dependent on the specific details of the active matter system in consideration. An advantage of the existence of non-trivial active particle-surface interaction is that the behaviour of active matter systems can now be modified by specifically designing the surfaces on which they propel. Peng *et al.* showed for example that bacteria suspended on a liquid crystal interface are sensitive to the anisotropy of the liquid crystal medium and their trajectories could therefore be controlled by patterning the liquid crystal interface (Figure 7A)[66]. A similar effect was also shown by

Guillamat *et al.* for active microtubules whose flow could be aligned with an adjacent liquid crystal (Figure 7B)[67].

1.6 Self-propulsion at the microscale

I have so far introduced active matter systems in general, discussed some examples of biological and artificial systems and finally described the emergent collective phenomenon and wall-induced effects that result from the self-propulsion of active particles. In this section I will consider in detail, active particles at the colloidal length scales where the active matter system used in this thesis operates. Colloids are dispersions of non-density matched particles in a liquid that remain suspended against gravity by the virtue of their Brownian motion, the constant random motion that particles suspended in a fluid undergo due to collisions with the fast-moving molecules in the fluid. Einstein in fact predicted that in a dilute suspension, the number density of particles, n, as a function of height z, in earth's gravitational field (acceleration = g) should follow an exponential distribution[68]:

$$n(z) = n(0)e^{\frac{-z}{z_0}}, \text{ where} \tag{8}$$

$$z_0 = \frac{k_B T}{\Delta m g} \tag{9}$$

is the sedimentation height, Δm is the buoyant mass of the particle, k_B is the Boltzmann's constant and g is the gravitational constant. He identified that the colloidal particle was in thermal equilibrium with the liquid molecules, so

the equipartition assumption and therefore the Boltzmann distribution applied. A suspension for which $z_0 \geq R$, where R is the particle radius is defined as a colloid. For everyday densities, this sets the condition of particle radius of the order $R \lesssim 10^0$ μm to be classified as colloids.

The physics at this scale can be non-intuitive and necessitates that the micro-scale active particles employ unique mechanisms for self-propulsion that one wouldn't encounter at larger length scales. Micro-scale swimmers such as bacteria live in a world where the viscous forces are so large that the inertial term in the Newton's equation of motion can be safely ignored. Bacterial locomotion determined by the dominating viscous forces is completely different from motion mechanisms that we encounter commonly at the larger length scales where propulsion relies largely on inertial effects. Edward Purcell in his classic article 'Life at low Reynolds number' highlighted this distinction by formulating what is known as the scallop theorem (Figure 8)[69].

A scallop is a small bivalve organism that moves by opening its shell slowly and closing it quickly. During this fast closing mechanism, the scallop expels water and develops momentum which lets it coast along for a small distance due to inertia (Figure 8D). A typical scallop has a length a of about 1 cm and has a propulsion velocity v of a several cm/s, i.e, it moves several body lengths in a second. Thus, the Reynold's number, a dimensionless parameter that compares inertial and the viscous forces and is given by $Re = \rho a v/\eta$, where ρ is the density of the medium and η is the viscosity of the medium, for a scallop

is about 100. Now calculating the Reynold' s number for organisms much smaller than the scallop, like at the microscale, and moving also at several body lengths per second, we obtain Re ≈ 10^{-5}.

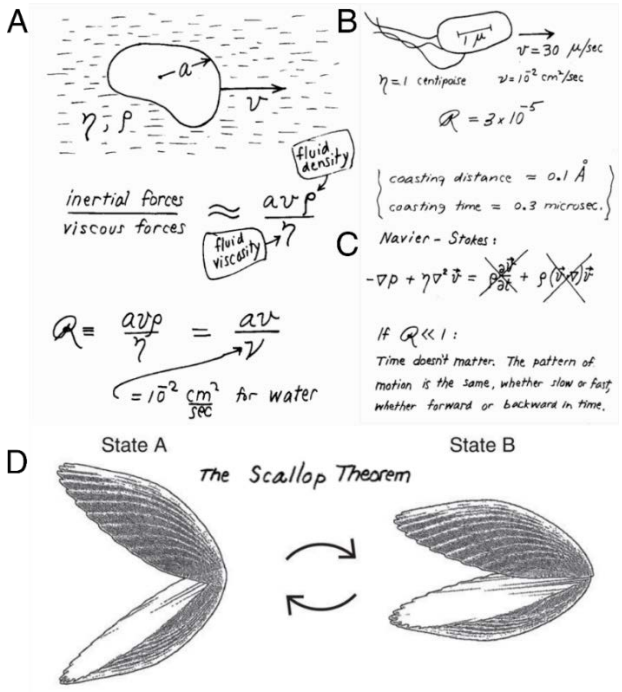

Figure 8: Life at low Reynolds number. (**A**) Definition of dimensionless Reynolds number which compares inertial and viscous forces. (**B**) The consequences of Low Reynolds number and the effect on swimming behaviour of microorganisms. (**C**) Navier-Stokes equation at low Reynolds number. (**D**) The proposed mechanism of swimming in Scallopswith a motion having a single degree of freedom.[69]

At this Reynolds number the micro-scallop would coast for <1Å, as the motion generated by the opening the shell would cancel out the motion generated by closing the shell. A tiny scallop therefore cannot move by opening and closing its shell. The mathematical reason behind this becomes apparent when one

looks at the Navier Stokes equation at low Reynolds number. The motion of fluid substances is defined by the Navier- Stokes equation given by:

$$\rho\left(\frac{\partial v}{\partial t} + v.\nabla v\right) = -\nabla p + \eta\nabla^2 v + f \tag{10}$$

Where ρ is the fluid density, p is the pressure, η is the viscosity of the medium, v is the velocity and f is the external force. At low Reynold' s number we can neglect the inertial terms in the equation and the Stokes equation can be written as:

$$-\nabla p + \eta\nabla^2 v + f = 0 \tag{11}$$

One of the consequences of the form of this equation is reversibility. If $v(r)$ is a solution of the equation with an associated pressure $p(r)$, then $-v(r)$ is also a solution with the forces and the pressure field reversed. This means that time reversible swimming strokes like the opening and closing of a scallop will not result in any effective motion at low Reynold' s number. The net water flow during opening would exactly balance that during closing and there would be no effective motion. Opening and closing at different speeds would also not solve this problem as the aggregate flow is going to remain the same irrespective of how fast or slow the opening and closing are. Time does not appear explicitly in the equation. The motion is therefore dependent only on the sequence of configurations, and not on how rapidly or slowly these sequences are executed. And any sequence that retraces itself in a complete

cycle, and is the only sequence available, such as in the scallop with its single degree of freedom, would result in no net motion.

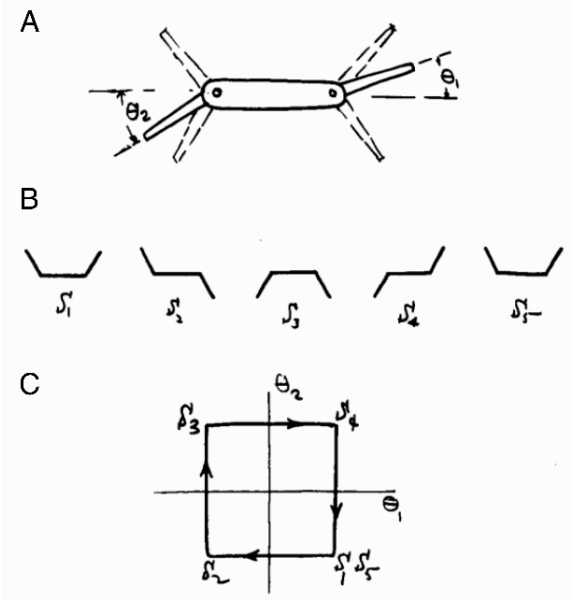

Figure 9: Swimming at low Reynolds number. (A) Schematic of a non-reciprocal swimmer proposed by E. Purcell containing two degrees of freedom. (B) The sequence of configurations the swimmer takes to avoid reciprocal movement and b reak time symmetry. (C) The loop in the configuration space that allows the swimmer to move in low Reynolds number.[69]

Purcell in his article described several locomotion mechanisms that were composed of cyclic shape changes where the sequence of one half of the cycle does not simply trace back the sequence of configurations of the other half[69]. The simplest of these is shown in Figure 9A. He proposed a swimmer that contains two hinges and therefore has two degrees of freedom as opposed to a scallop which has a single hinge. All that this swimmer must do is to go through the sequence S1-S4 shown in Figure 9B and return to the original

configuration in S5 (Figure 9C). It's easy to see that this mechanism breaks the time reversal symmetry and can result in net motion even at the microscale.

1.7 Motion mechanisms in biological micro-swimmers

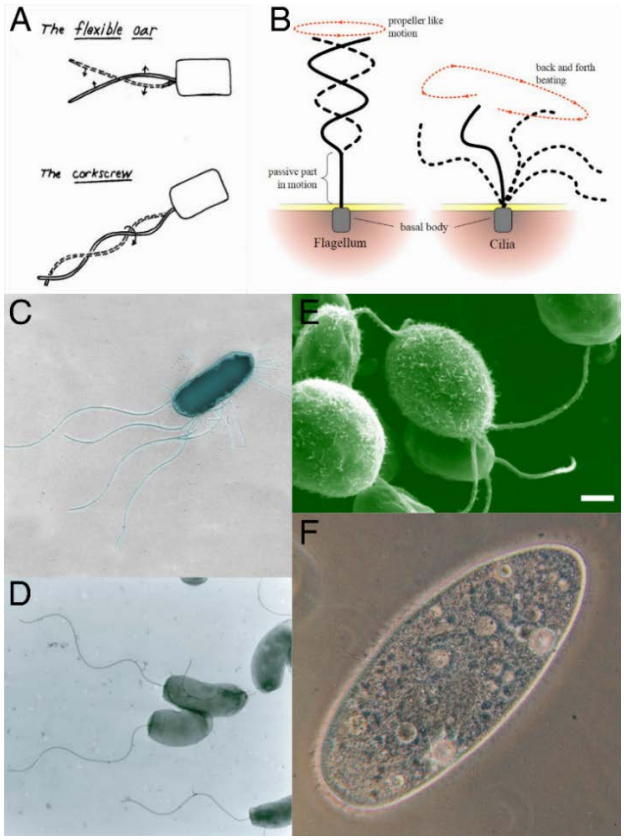

Figure 10: Non-reciprocal motion mechanisms employed by biological micro-swimmers. (**A**) Schematic representation of the 'flexible oar' mechanism or the 'corkscrew' mechanism that enables swimming in biological micro-swimmers[69]. (**B**) The micro-organisms can either pushed by rotating helical flagella as in the case of Escherichia Coli or Vibrio Cholerae bacteria (**C-D**) [70–72] or be pulled by flexible cilia as in the case of Chlamydomonas reinhardtii algae or Paramecium protozoa (**E-F**)[73,74].

While the two-hinge swimmer does move at low Reynolds number, it is not one that is encountered in nature. Biological swimmers at the micro-scale

benefit primarily from either having a flexible oar or a corkscrew structure (Figure 10A)[59]. A rigid oar does not produce any motion for the same reason as a scallop; it only has a single degree of freedom. A flexible oar on the other hand, acquires a curvature whose concavity depends on the direction of its motion – concave down when the flagella is moving upward and concave up when the flagella is moving downward. It relies therefore on the internal relaxation of the oar curvature to escape the time reversal symmetry. The corkscrew mechanism avoids retracing the steps by chirality. At low frequencies, the swimmer moves a fixed distance for each complete rotation of the chiral screw about its axis.

The corkscrew mechanism is implemented in biological micro-organisms through flagella which are often located at the back of the body and are longer in length than the body. These are rigid object with a helical shape and push the cell body forward as they rotate. While some organisms, such as *Vibrio Cholerae*, are equipped with a single flagellum, others like *E. Coli* are equipped with multiple flagella that are bundled together hydrodynamically (Figure 10B, D, C). The flexible oar mechanism is implemented either through long cilia at the front of the cell body as in the case of *Chlamydomonas reinhardtii*, or as short filaments embedded across the body as in the case of *Paramecium* protozoa where the filaments wiggle together to amplify the strength of the strokes (Figure 10 B, E, F).

There have been attempts to implement both these mechanisms in artificial systems. One of the first attempts was to create cilia like structures composed of superparamagnetic particles, coated with streptavidin, and linked together by double stranded DNA (Figure 11A)[75]. These artificial cilia were then attached to a red blood cell and driven by a time-varying magnetic field. The cilia try to follow the magnetic field, but as a consequence of their flexibility and viscous friction, reorientation is also associated with bending. This coupling between magnetic forces, flexibility of the colloidal chains and the viscous drag from the solvent generates controlled deformations in the cilia. With the proper field conditions and flexibility, the time-reversal invariance of the artificial cilia could be broken, and the attached cell was propelled.

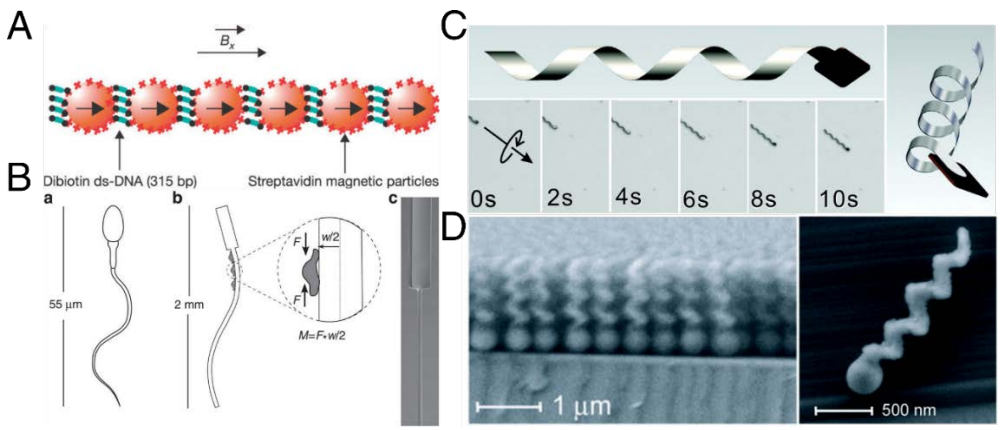

Figure 11: Artificial swimmers mimicking the motion mechanism of biological micro-swimmers. (**A**) A cilium inspired micro-swimmer consisting of a string of colloidal particles linked by strands of DNA. Motion is activated through an oscillating magnetic field[75]. (**B**) Biohybrid swimmer, consisting of an elastic filament with a rigid head and a compliant tail, and a small, single cluster of contractile cells generating a force F at a distance w/2 from the filament's neutral axis[76]. (**C**) Flagella inspired artificial micro-swimmers composed of a helical ribbon attached to a soft magnetic head[77] or a

silica helix coated with a ferro magnetic material[78] (**D**) both actuated through an external rotating magnetic field.

Another approach to obtain artificial deforming cilia was reported by Williams *et al.*, who instead of using a transversal oscillating magnetic field, achieved deformation through the contraction of cardiomyocytes (Figure 11B)[76]. They directly cultured cardiomyocyte cells onto a PDMS filament with a short rigid head and a long slender tail. By functionalizing the rigid head and the part of the tail close to it with extra cellular matrix and the rest of the tail with a cell de-adherent, they could selectively control cell placement on the PDMS structure. Since the cardiomyocyte cells contract at a frequency of about 3 Hz, they deform the flexible tail and a propulsion of about 10 µm/s was achieved.

Artificial microstructures that can replicate the motion resulting from the rotation of a corkscrew geometry have also been demonstrated. Examples of this include magnetic helical tails actuated by a rotating magnetic field. The screw like rotation of these structures breaks the time reversal symmetry and results in the propulsion of the helical structures. Figure 11C shows a helical ribbon attached to soft magnetic head that rotates in an oscillating magnetic field[77]. Smaller versions of these helical structures were achieved by glancing angle deposition of silica onto a silica seed (Figure 11D) and through Direct Laser Writing[78,79]. The propulsion velocity of these helical structures like in biological flagellar swimmers, is dependent on the frequency of the applied oscillating magnetic field.

1.8 Interfacial transport

Artificial active particles that directly imitate the biological micro-swimmers are difficult to fabricate, often involving complex chemistry or multiple lithography steps. A different class of active particles have been developed that depend on interfacial transport and greatly reduce the complexity involved in producing artificial active particles. The interface between two phases has been historically assumed to play a very minor role in the context of fluid dynamics. For solid-liquid interfaces, an assumption of no-slip is generally applied at the solid wall, and in fact, is sufficient to account for many observed hydrodynamic phenomena such as the Poiseuille flow. This assumption however ignores the structure of the transition between the two phases which, in reality has a finite, if very small, thickness. The dynamical processes occurring within this region can lead to a 'slip velocity' that on a macroscopic length scale seems to violate the no-slip condition. Under the no slip condition, the velocity of the particle $\overrightarrow{v_p}$ induced for example by an external field is completely balanced by a counter-acting flow $\overrightarrow{v_f}$. However, in the presence of a slip velocity, we get $\overrightarrow{v_p} + \overrightarrow{v_s} = \overrightarrow{v_f}$ implying that motion is possible even in the absence of external forces.

Phoretic transport is defined as the migration of colloidal particles in a field that interacts with the surface of each particle[80]. The particle surface and the surrounding liquid can interact with each other within a small interfacial layer that is typically <10 nm. If the surrounding of the particle is completely

homogeneous, then all the forces exerted are isotropic and no net motion is observed. However, if a surrounding gradient exists of a field that can act on the solvent molecules around the particle, then an effective force comes into play, which can lead to particle migration. From the perspective of a micron sized particle, this effective force acts as an apparent slip velocity.

An important characteristic of phoretic transport is that the external field applies no force to the particle plus the fluid in the interfacial region. To the outer fluid, the moving particle appears to be force free and torque free. The motion of the particle appears then not from a net force but due to this additional hydrodynamic effect of the appearance of a slip velocity.

1.8.1 Electrophoresis

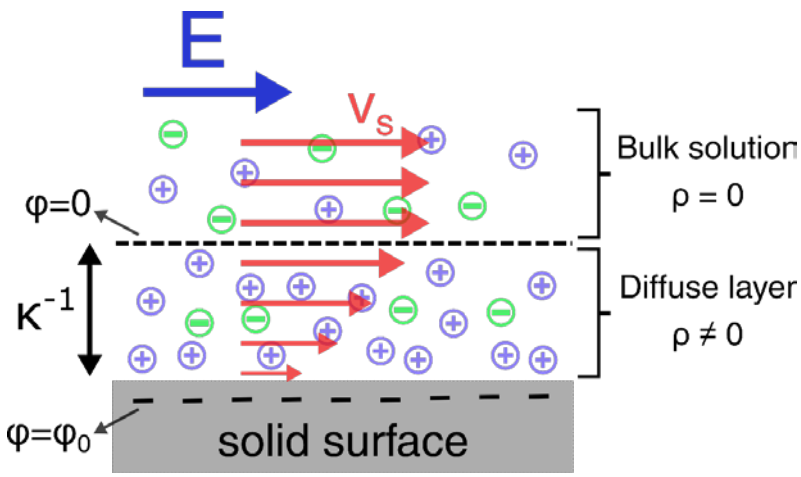

Figure 12: Schematic representing the origin of electro-osmotic flow close to charged surface on application of an electric field in the x axis. Adapted from [81].

A logical starting point to understand the appearance of the slip velocity is to consider a model system where the physics of the interactions between the particle surface and the surrounding fluid is well understood. Electrophoresis is the migration of a charged colloid in an applied electric field and is perhaps the most well studied of phoretic phenomenon[82–85].

Consider a glass wall in contact with an electrolyte solution as shown in Figure 12. Chemically the structure of the glass wall at the surface will be dominated by silanol groups. If now, a pH 7 electrolyte is brought in contact with this surface, the surface groups perform as weak acids and some of the protons will go into the interface as H^+ ions. This will leave SiO^- groups at the surface, which on an average makes the wall negatively charged as shown in the schematic. This charged wall attracts a tiny layer of cations whereas anions are repelled, leading to the formation of a thin double layer in the vicinity of the wall. The steady distribution results from the balance between the electrostatic attraction by the charged surface and the Brownian diffusion of the ions. The potential at the wall is given by φ_0 and we set the equilibrium potential of the bulk, far away from the wall, to 0 (Figure 12). The rate at which the potential away from the wall decays to the equilibrium value can be extracted analytically from the Poisson-Boltzmann equation for excess charge density. Under the assumption of weakly charged electrolytes, the potential $\varphi(r)$ was shown to obey the following exponential law:

$$\varphi(r) = \varphi_0 e^{-\kappa r} \tag{12}$$

where r is the distance from the surface and the thickness of the double layer close to the surface is given by the inverse of the coefficient κ:

$$\kappa^{-1} = \left[\frac{8\pi Z^2 e^2}{\varepsilon kT} C^s\right]^{-\frac{1}{2}} \tag{13}$$

where C^s is the electrolyte concentration at the outer edge of the double layer, Z is the valence of the positive and negative ions of the electrolyte, e is the charge of an electron, ε is the fluid dielectric constant, and kT is the thermal energy. Since all the interesting interfacial phenomena occur within this thin diffuse layer, we can perform an integral boundary analysis of this small region close to the wall.

Now, if we apply an electric field to this system in the x-axis, parallel to the wall, we can calculate the magnitude of the resulting flow (see Figure 12). Close to the wall, in the diffuse layer, we have a charge density $\rho_e(y)$ that equals the difference between the concentrations of counterions (positive here) and coions (negative). The applied electric field acts on the space charge in the diffuse layer to produce a body force $E_{ext}\rho_e(y)$. The stokes equation within the diffuse layer is then given by

$$\eta\nabla^2 v = -\rho_e E_{ext}. \tag{14}$$

and the relation between the charge density and the potential is given by Gauss' law:

$$-\varepsilon\nabla^2\varphi = \rho_e. \tag{15}$$

Rewriting the Stokes equation, we get:

$$\eta \nabla^2 v = \varepsilon E_{ext} \nabla^2 \varphi. \tag{16}$$

Since the potential varies along *x* over much longer length scales than those over which interfacial forces operates, in *y*, we can write

$$\eta \frac{\partial^2 v}{\partial y^2} = \varepsilon E_{ext} \frac{\partial^2 \varphi}{\partial y^2}. \tag{17}$$

Integrating the above equation with appropriate boundary conditions (no slip at the wall and bulk potential far away from the wall is 0), we get:

$$v = \frac{\varepsilon E_{ext}}{\eta} \big(\varphi_0 - \varphi(y)\big) \tag{18}$$

The slip velocity is defined as the value of *v* at the outer limit of the double layer (see Figure 12), where $\varphi(y) = 0$ as defined, and is given by:

$$v_s = \frac{\varepsilon \varphi_0 E_{ext}}{\eta}. \tag{19}$$

We can consider a colloidal particle with radius *R* much larger than the Debye length $\kappa^{-1}$and subjected to an electric field E_{ext}, and perform a similar analysis as for a flat wall. We find that the colloidal particle moves at a velocity just enough to cancel the slip velocity. The electrophoretic velocity of the particle is given by:

$$\boldsymbol{v_{particle} = -\frac{\varepsilon \varphi_0 E_{ext}}{\eta}} \tag{20}$$

It is clear from the above expression that the particle velocity is linearly dependent on the applied field. φ_0 which we defined as the potential at the particle surface, and is referred to as zeta potential, is a function of the chemistry of the particle. The glass surface that we have considered in our

analysis has a negative zeta potential. By switching the material to one that has a positive zeta potential we can reverse the direction of migration of the colloidal particle under the same external electric field.

1.8.2 Diffusiophoresis

This section is partially based on the content found in 86

So far in our analysis of electrophoresis, we have simply considered the ions in the solution where the particle is suspended as point charges, and the phoretic mobility was resultant from the electrostatic interactions in the thin double layer close to the surface. It has also been shown that a gradient of a solute, charged or uncharged, along a surface can also induce a phoretic velocity[87]. In the following analysis we will begin directly on the surface of a colloidal particle and consider the case of the solute being neutral.

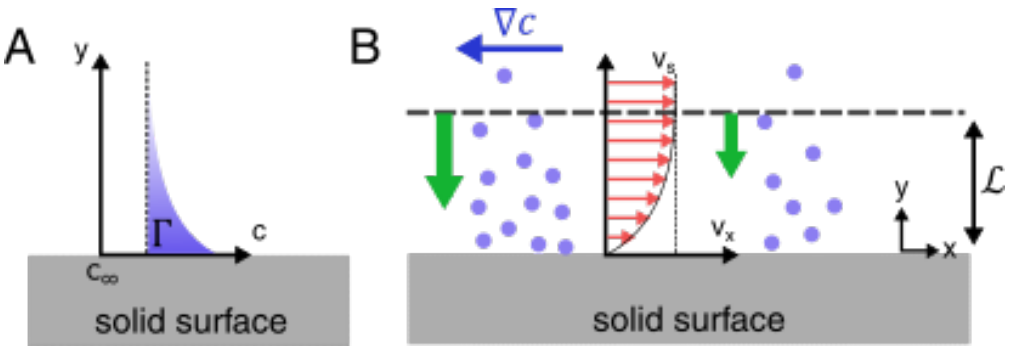

Figure 13: Schematics representing the origin of diffusiophoretic flow close to a surface in the presence of a gradient of solvent molecules. (**A**) The excess surface concentratio**p**lotted along the direction of the surface normal. (**B**) If there is a concentration gradient of solutes along x (here, more concentrated on the left), a tangential pressure gradient results, which drives a flow parallel to the surface. Adapted from [86].

Consider the system of a colloidal particle in a neutral solute with bulk concentration c_∞. We can take the particle surface to be large enough that it can be considered as a locally flat surface. The interaction of the solute and the colloid surface can be described by a short-range potential *U(y)* and this gives rise to an excess surface energy per unit area of $\sigma(c)$. If the solute is attracted to the surface, then the solute profile can be sketched as in Figure 13A, and the excess surface concentration is given by

$$\Gamma = \int_0^\infty [c(y) - c_\infty] dy \tag{21}$$

This excess surface concentration can be normalised to an adsorption length κ where

$$\kappa = \frac{1}{c_\infty} \int_0^\infty [c(y) - c_\infty] dy \tag{22}$$

So κ is essentially the thickness of the bulk layer that contains as many solute molecules as the excess layer. Diffusiophoresis occurs in the cases where there exists a solute gradient along the surface (Figure 13), that is, $\partial c_\infty / \partial x \neq 0$.

For an ideal solute, the distribution from the surface is given by

$$c(y) = c_\infty e^{-\beta U(y)} \tag{23}$$

If the concentration varies along x over much longer length scales than those over which interfacial forces operate then the equilibrium of concentrations and pressures is much faster along y than along x. The solute concentration is then locally Boltzmannian and is given by

$$c(x,y) = c_\infty(x)e^{-\beta U(y)} \tag{24}$$

A solute at *y* experiences a force *–∂U(y)/∂y* because of its interaction with the surface and this is transmitted to the solvent

$$-\frac{\partial p}{\partial y} + c\left(-\frac{\partial U}{\partial y}\right) = 0 \tag{25}$$

The above two equations then solve to

$$\beta[p(x,y) - p_\infty] = c_\infty(x)\left[e^{-\beta U(y)} - 1\right] \tag{26}$$

The variation in pressure due to gradient of c_∞ along *x* drives a solvent flow (see Figure 13) which is balanced by the viscous stress of the flow, i.e,

$$-\frac{\partial p}{\partial x} + \frac{\partial}{\partial y}\left(\eta\frac{\partial u_x}{\partial y}\right) = 0 \tag{27}$$

to be solved with the boundary conditions of no slip at the surface ($v_x(y=0) = 0$) and no velocity gradient in the bulk ($(\frac{\partial v_x}{\partial y})_{y\to\infty} = 0$).

Solving Eq. (27) with these boundary conditions we get,

$$v_x(y) = -\frac{k_B T}{\eta}\frac{\partial c_\infty}{\partial x}\int_0^y dY\int_Y^\infty [e^{-\beta U(y')-1}]dy' \tag{28}$$

Since *v(x,z)* would have reached its asymptotic value u_s at $y \geq \mathcal{L}$, we can take $v_s = v_x(y\to\infty)$ and we get

$$v_s = -\frac{k_B T}{\eta}\frac{\partial c_\infty}{\partial x}\int_0^\infty dY\int_Y^\infty [e^{-\beta U(y')-1}]dy' \tag{29}$$

Solving the above integral leads to the expression for slip velocity

$$v_s = \frac{-k_B T}{\eta}(\kappa\mathcal{L})\frac{\partial c_\infty}{\partial x} \tag{30}$$

$\mathcal{L}$ here measures the range of the solute-surface interaction potential. The above equation predicts that if the solute is attracted to the surface then in the stationary frame of the surface the solvent flows from high to low solute concentration. In the stationary frame of the liquid, the surface translates up the solute concentration gradient. Another implication of (16) is that a large adsorption length κ leads to a larger diffusiophoretic velocity and that we need a finite $\mathcal{L}$, which requires a finite interaction potential between the surface and the solute. The diffusiophoretic velocity of a particle can be written by switching frames (and the sign) from the equation of the slip velocity

$$v_{dph} = \frac{k_B T}{\eta}(\kappa\mathcal{L})\nabla c_\infty \tag{31}$$

In a set of illustrative experiments, Abecassis *et al.* showed that it is possible to achieve a strongly amplified migration of large colloidal particles, where Brownian diffusion does not play a significant role, by slaving their dynamics to that of a fast carrier species, a dilute salt in their case, via the diffusiophoretic mechanism (Figure 14)[88]. They studied the migration of colloidal particles in a microfluidic device with a ψ channel geometry. The colloids were always flown in the central channel and depending on if they introduced the salt in the side channels or the central channel along with the colloids, they achieved a spreading or focusing of colloidal particles respectively.

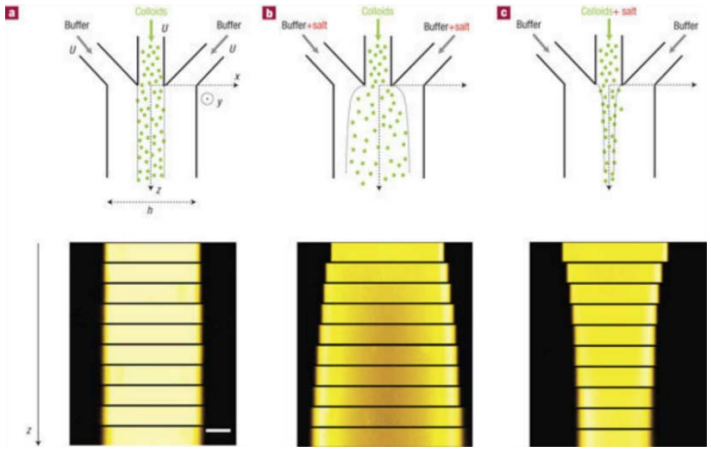

Figure 14: Diffusiophoretic migration of colloids. A colloidal solution is injected with a co-flowing buffer in a ψ microfluidic channel (**left**). Depending on where the solute is inserted, the colloids either spread (**centre**) or focus (**right**) due to diffusiophoretic drift[88].

1.8.3 Self-phoresis of colloidal particles

I have so far described how a gradient of electric field or solute distribution around a colloidal particle can lead to the migration of the particle, its direction and velocity determined by the surface properties of the particle and the magnitude of the gradient imposed. We have assumed that this gradient is imposed externally and acts on all the particles in the system. Now, if a particle were to be capable of self-generating this gradient in which it migrates, it can be considered an active particle by the definition that was introduced at the beginning of this chapter. It would derive its energy for propulsion locally, via the mechanism with which it generates its associated gradient, and the directionality of its motion would be set by an internal co-ordinate of the particle, dictated by the asymmetry of the local gradient.

In order to create these local gradients, the particle would have to be equipped with some sort of surface asymmetry. Golestanian and co-workers did indeed propose such a model system which consisted of a colloidal particle decorated on one side with an enzymatic patch as shown in Figure 15[89]. When this colloid is placed in a solution containing the substrate of the enzyme, a chemical reaction would take place, but only in the vicinity of the enzymatic patch. This introduces an asymmetry of the reaction product along the particle surface (Figure 15) and as discussed in the previous section, leads to the migration of the particle.

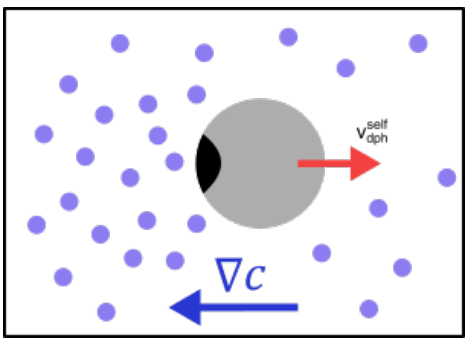

Figure 15: Schematic of a colloidal sphere undergoing self-diffusiophoresis. A catalytic patch (dark) on a particle catalyzes a reaction in the solvent, giving rise to a concentration gradient of products. Adapted from 86.

These types of colloids which contain a patch of material whose properties differ from the rest of the surface are referred to as *patchy* colloids. A vast literature exists on precisely creating patchy particles with well-defined properties. These particles have been typically used for self-assembly, as a sort of colloidal analogues to molecules where a specific number of particles with

specific properties self-assemble into colloidal molecules. In order to create self-propelled phoretic particles, the simplest of these patchy colloids, Janus particles are typically used. Janus particles, named after the Roman god of beginnings and transitions, contain two faces with heterogenous properties. In our case, one half of the colloidal particle (typically silica) is coated with a thin layer of Pt. It is simple enough to create these particles by using standard evaporation methods. Typically, one begins by creating a monolayer of colloidal particles on a flat substrate. While simple drop-casting methods are sufficient to create reasonably well assembled monolayers, Langmuir Blodgett troughs can be used for obtaining close packing of the colloids. Once the monolayers are dried, a metal evaporation method is used to deposit thin layers of desired metal (Pt) on one half of the particle surface. Since, the colloidal particles we use are spherical, they automatically offer the self-shadowing property necessary to deposit the metal layer only on one side which shadows the other half of the particle.

While the monolayer method of creating Janus particles is straightforward, it lacks in the ability to mass produce particles. The reliance on having to create single monolayers severely hinders the number of particles than can be produced in a single process. There exist other volume-dependent methods that can be used for mass production of Janus particles. One of these methods is to use Pickering emulsions, where the colloidal particles are trapped at wax/water interfaces, which act as surfactants, and prevent the emulsion

droplets from coalescing[90,91]. The continuous phase is then used to functionalize the exposed half through chemical or electrochemical methods. The spherical geometry of the droplets used here greatly increases the number of particles that can be produced in a single batch.

In the rest of this section, we will focus on a colloidal Janus particle, specifically, a spherical silica particle that is half covered with a catalytic patch (normally Pt). The heterogeneous surface catalysis produces a solute gradient in which the particle undergoes diffusiophoresis. Since this gradient is created by the particle itself, we refer to it as self-diffusiophoresis.

In order to obtain self-diffusiophoretic velocity, eq (31) that was derived for diffusiophoresis can be used but we need to obtain an expression for ∇c for the concentration gradient around the colloidal particle. In the case of a simple one step reaction, which gives rise to a uni-molecular product that causes the gradient, the following scaling arguments can be made. The assumption of this one-step reaction is purely for the sake of simplicity in calculations and doesn't necessarily reflect experimental reality. Product molecules diffuse away from the catalytic patch with a flux $D_p \nabla c$ where D_p is the diffusion coefficient of the product. In steady state, this should be matched by the amount of product (N_p) that is being produced which leads to

$$\left|D_p \nabla c\right| a^2 = \frac{dN_p}{dt} \tag{32}$$

Using $dNp/dt = \tau_c^{-1}$, the rate of the catalysis, we get:

$$|\nabla c| = \frac{1}{D_p a^2 \tau_c} \tag{33}$$

For the case of a Pt coated Janus particles we have:

$$H_2O_2 \xrightarrow{Pt} H_2O + \frac{1}{2}O_2$$

The rate of production of O_2 is given by:

$$\frac{d[O_2]}{dt} = k_1[H_2O_2]$$

Where k_1 is the rate of production of O_2 at a Pt surface in H_2O_2, so $k_1[H_2O_2]A = \tau_c^{-1}$ where A is equal to a^2 and is approximately the area of a catalytic patch on a particle of radius a. Substituting into eq (33) gives

$$|\nabla c| = \frac{k_1[H_2O_2]}{D_p} \tag{34}$$

Substituting back the expression for ∇c into the equation of diffusiophoretic velocity (eq. 31), we have

$$|v_{dph}^{self}|^{(I)} = \frac{k_B T}{\eta}(\kappa\mathcal{L})\frac{k_1}{D_P}[H_2O_2] \tag{35}$$

If we treat that the interaction of the solute with both silica and Pt as repulsive, then we get that the particles should swim away from their Pt caps which is experimentally verified. In the above equation (Eq. 35) we see that the velocity should be proportional to the fuel concentration. This is indeed experimentally verified to be true at low concentrations of the fuel, but at higher concentrations the dependence becomes sub-linear. This can be explained by postulating that the reaction takes place in two steps forming a Pt:H_2O_2

complex whose decomposition is governed by k_2. At higher concentrations the first reaction is saturated and k_2 is the limiting step giving:

$$|v_{dph}^{self}|^{(II)} = \frac{k_B T}{\eta}(\kappa\mathcal{L})\frac{k_2}{D_P} \tag{36}$$

More recently it was observed that the velocity of the particle is dependent on the size of the particle. The velocities were inversely proportional to the size of the particle. This feature can be explained by accounting for the flux transporting reactants towards the catalytic patch. When the reaction is fast, and the particle size is large it is possible that the diffusive flux is the limiting step:

$$|v_{dph}^{self}|^{(III)} = \frac{k_B T}{\eta}(\kappa\mathcal{L})\frac{[fuel]}{a} \tag{37}$$

These three regimes of self-diffusiophoretic particles are summarized in the Figure 16.

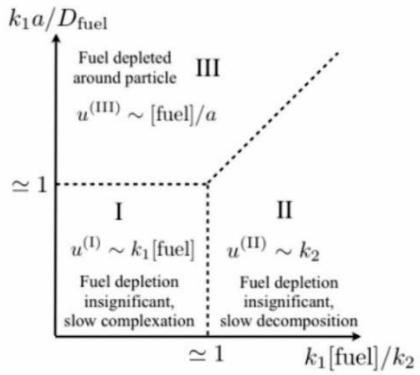

Figure 16: Schematic of different propulsion regimes predicted for a self-diffusiophoretic Janus particle dispersed in a peroxide solution. From [86] adapted from [92].

These silica-Pt Janus particles are of course not the only active particles that derive their self-propulsion from self-phoresis. Even before the silica-Pt particles were introduced, Paxton *et al.* demonstrated self-propulsion of Au-Pt rods[93]. When suspended in a solution of H_2O_2, a redox reaction takes place along the surface of these bimetallic particles. The oxidation of H_2O_2 occurs preferentially at the Pt end and the reduction of H_2O_2 at the Au end. Since there is an excess of H^+ on the Pt side, an electric field points from the Pt end to the Au end (Figure 17A). We have already seen in a previous section that the presence of an electric field and charged species in the solution leads to electrophoretic migration (Figure 12). Palacci *et al.* introduced a system of colloidal particles with a hematite cube embedded in the particle that was capable of self-propulsion in a solution of H_2O_2 when illuminated with a blue light (Figure 17B)[42,94]. Buittinoni *et al.* showed that Au coated colloidal Janus particles self-propel when suspended in a critical binary mixture of water-lutidine and exposed to light (Figure 17C). They described that the local asymmetric demixing induced by the illumination-borne heating from the Au cap generates a local spatial chemical concentration gradient which is eventually responsible for the particle's self-diffusiophoretic motion[95,96]. Another class of self-propelled particles that have been recently developed are colloids coated with biological enzymes (Figure 17D)[97]. These particles propel in solutions containing the enzyme substrate and owing to their bio-compatibility as opposed to systems that use H_2O_2 are touted to be potential carriers for drugs in biological systems.

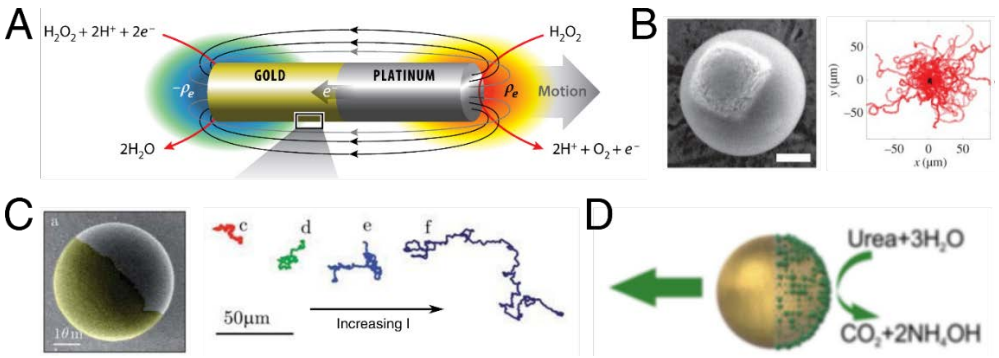

Figure 17: Self-phoretic particles. (**A**) Self-electrophoretic Au-Pt nanorods that propel in H_2O_2[98]. (**B**) Colloidal particles with a hematite cube embedded that surf on self-generated diffusiophoretic flows close to a confining surface[94]. (**C**) Colloidal particles with a gold cap when immersed in a water-lutidine mixture and exposed to light propel due to the diffusiophoretic flows arising from the local de-mixing of the water-lutidine solution[95]. (**D**) Enzyme coated Janus particles asymmetrically degrade their substrate in the solution leading to self-diffusiophoretic motion[99].

It is impractical here to go into a full literature review of all the different designs of self-phoretic particles that exist given that the literature is now extremely vast. The interested reader will however find these reviews useful in getting an overview of all the self-propelled phoresis based artificial systems that exist[98,100–102].

I will conclude this chapter by bringing the focus back to silica-Pt colloidal particles suspended in a solution of H_2O_2 which I use throughout this thesis. I have already described the dependence of their propulsion velocity on fuel concentration and particle size. I will give here, a brief account of the dynamics of self-propelled motion observed in these systems. When observed under a microscope, these self-phoretic Janus particles seem to perform a persistent random walk on the long run. This is similar to what is observed in biological

micro swimmers like bacteria and results from the competition between ballistic motion under the propulsive power derived from diffusiophoretic migration and the angular randomization caused by the thermal fluctuations from the solvent molecules (Brownian motion). The position $[x(t), y(t)]$ of a spherical microscopic particle with radius R undergoes Brownian diffusion with translational diffusion coefficient:

$$D_T = \frac{k_B T}{6\pi\eta R} \tag{38}$$

where k_B is the Boltzmann constant, T the temperature, and η the fluid viscosity. The particle self-phoretic motion results in a directed component of the motion with speed v that is constant and is correlated with the particle orientation $\phi(t)$. Finally, $\phi(t)$ undergoes rotational diffusion with rotational diffusion coefficient:

$$D_R = \frac{k_B T}{8\pi\eta R^3} \tag{39}$$

The transition between the propulsive and diffusive regimes occurs at the rotational diffusion time $\tau_R = 1/D_R$. Physically τ_R is the timescale at which the propulsion direction the self-phoretic particle, which is aligned with the orientation of the particle, decorrelates. For $t \ll \tau_R$, the colloid propels along the direction ϕ and there is very little random fluctuation of ϕ. The colloid seems to simply go along ϕ with a constant velocity v. At $t \sim \tau_R$, the particle direction ϕ is randomised and the particle moves along a new direction ϕ' decorrelated with the previous one (Figure 18). For $t \gg \tau_R$, the particle seems

to be performing random steps of average length $l_p = \tau_R v$, referred to as persistence length.

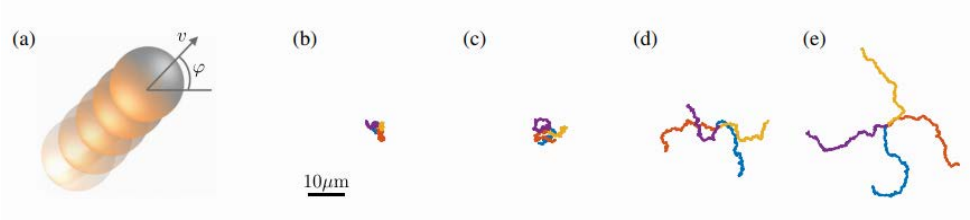

Figure 18: Active Brownian particles in two dimensions. (A) An active Brownian particle in water (R = 1 μm, η = 0.001 Pa s) placed at position [x, y] is characterized by an orientation φ along which it propels itself with speed v while undergoing Brownian motion in both position and orientation. The resulting trajectories are shown for different velocities (**B**) v = 0 μms^{-1} (Brownian particle), (**C**) v = 1 μms^{-1}, (**D**) v = 2 μms^{-1}, and (**E**) v = 3 μms^{-1}. With increasing values of v, the active particles move over longer distances before their direction of motion is randomized; four different 10-s trajectories are shown for each value of velocity.[103]

The full expression for the mean square displacement of these particles was shown to be[104]:

$$\langle\left(r^2(t) - r^2(0)\right)\rangle = 4D_0 t + \frac{v^2 {\tau_R}^2}{2}\left[\frac{2t}{\tau_R} + e^{\frac{-2t}{\tau_R}} - 1\right] \quad (40)$$

Applying temporal limits with respect to τ_R, we get:

$$\langle\left(r^2(t) - r^2(0)\right)\rangle = 4D_0 t + v^2 t^2 \text{ for } t \ll \tau_R$$

$$\langle\left(r^2(t) - r^2(0)\right)\rangle = (4D_0 + v^2 \tau_R) t \text{ for } t \gg \tau_R$$

It is clear from the above limiting equations that the motion of an active particle is characterized by ballistic behaviour ($\langle\left(r^2(t) - r^2(0)\right)\rangle \propto t^2$) at time scales shorter than the rotational diffusion time τ_R and on the longer time

scales leads to diffusive behaviour ($\langle\langle(r^2(t) - r^2(0))\rangle \propto t$) with an effective Diffusion coefficient D_{eff} given by:

$$D_{eff} = D_0 + \frac{1}{4}V^2\tau_R \tag{41}$$

In the following chapters I will describe the experiments performed to understand the interactions between self-phoretic active particles and nearby surfaces. We will see that apart from the self-propulsion characterised by persistent random motion, hydrodynamic and phoretic interactions play an important role in determining the behaviour of these particles close to confining surfaces. I will also describe how the surface interactions of self-phoretic particles can be exploited to generate a continuous directional flow of active particles. Finally, I will elaborate on a surprising effect that arises when an external flow is imposed on a self-phoretic particle close to a confining surface.

2.Interaction of phoretic micro-swimmers with surfaces

2.1 Introduction

Self-propelled biological micro-swimmers have constant, rich interactions with their surroundings which can substantially modify their swimming behavior.[105] Interactions between swimming microorganisms and nearby surfaces have been shown to play a significant role in important biological processes ranging from bacterial bio-film formation[106] to human fertilization[107]. Several recent studies have focused on understanding the physical mechanisms that govern these interactions.[108–115] A detailed understanding of these interactions has not only helped develop new biological insight into the functioning of cell flagella and cilia but has also led to the design of micro-structures such as micro-gears that can be powered by the stochastic swimming of bacteria[116] and micro-ratchets that can direct the locomotion of swimming algae[109] (Figure 19).

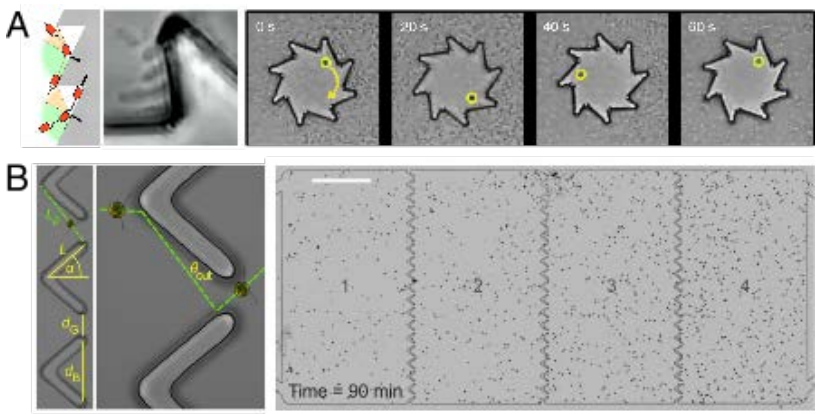

Figure 19: Interaction of biological micro-swimmers with walls. (A) Interactions of bacteria with walls, where they tend to align along the walls and get trapped by corners, can be exploited to create ratchet structures that convert the forces exerted by the swimming bacteria into rotational motion[116]. (B) The interactions between algae and nearbywalls is dominated by ciliary contact leading to their scattering at fixed

angles, which can be exploited to build microfluidic ratchets capable of rectifying their locomotion[109].

One of the earliest surface induced behaviours observed for micro-swimmers is the accumulation of live human sperm cells near surfaces. Lord Rothschild observed that live human cells accumulate near surfaces while dead cells do not, ruling out classical attractive interactions such as electrostatic or van-der-Waal' s forces.[117] Since then, similar accumulation behaviour has been observed for other swimmers such as sea urchin and bacteria[118,119] indicating that self-propulsion, common to all these systems, might play an integral role in the accumulation mechanism for these micro-swimmers. In some sense, the accumulation itself is not surprising and can be explained simply as a statistical phenomenon in systems of self-propelled particles.[120,121] Consider a confined cell with self-propelled particles as typically used in experiments with micro-swimmers. When a particle with velocity v reaches an impenetrable surface, it stays along the surface for a characteristic time τ before being reoriented and swimming back into the bulk. The characteristic time τ is set either by the thermal fluctuations in the case of an active Brownian model or the typical run length in the case of a run-and-tumble model. In such a system, the incoming flux towards the surface scales as ρv where ρ is the bulk density of particles. The outgoing rate from the surface will scale as σ/τ where σ is the surface density component. On equating the two terms, we find that the surface density builds up scaling as $\rho v\tau$, where $v\tau$ is the persistence length (ℓ) of the particles. So, a finite persistence length is a sufficient condition to lead to wall

accumulation of self-propelled particles. However, bacteria have been observed to remain close to surfaces for much longer periods than the characteristic bulk reorientation time τ, as assumed in the simple dimensional argument above, leading to stronger accumulation than predicted by purely active Brownian or run and tumble models.[110,111] This wall entrapment effect, no longer simply a result of statistical mechanics, has been attributed to the hydrodynamic coupling between the cell body and the surface, as shown in Figure 20.[122]

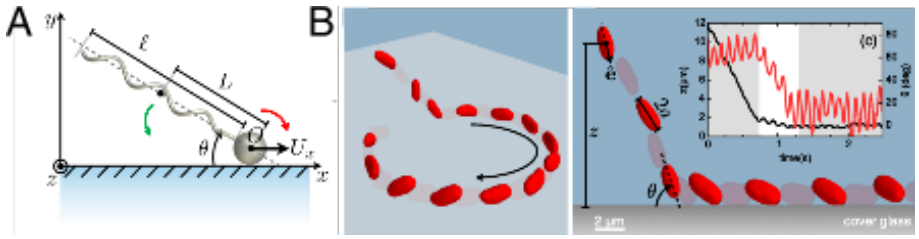

Figure 20: Wall-entrapment of bacteria close to surfaces. (**A**) Schematic of a swimming bacterium close to a surface. The red and green arrows correspond to the torques arising from hydrodynamic interactions of the cell body with the bottom surface and the drag on the flagella [Adapted from 122]. (**B**) Holographic microscopy images capturing the approach and entrapment of bacteria close to a surface arising from the stability of the swimming angle[123].

Since bacteria are pusher type swimmers, they approach a surface head first, as shown in Figure 20A. The cell body close to the surface experiences a shear which introduces a torque that rotates the flagella into the bulk (red arrow). The rotating flagella encounters a viscous drag in the bulk which introduces a torque in the opposite direction (green arrow). Resulting from these competing torques, bacteria attain a stable angle at which they swim close to

surfaces, leading to the entrapment effect observed in experiments. The existence of this stable angle has been confirmed by direct holographic microscopy observations of bacteria swimming close to surfaces performed by Bianchi *et al.* recently (Figure 20B).[123]

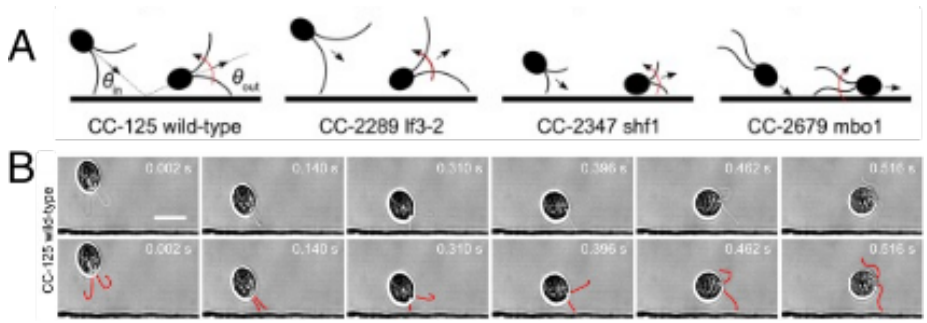

Figure 21: Scattering of Chlamydomonas from surfaces. (**A**) Schematic illustration of the flagella-induced scattering and trapping mechanisms[109]. (**B**) Scattering sequence for WT Chlamydomonas CC-125 obtained from optical microscopy. (Upper) Original micrographs. (Lower) Cilia manually marked red.[109]

In other biological swimmers such as *Chlamydomonas*, direct contact interactions between cilia and the solid surface has been shown be the dominant factor in determining the surface interactions, with hydrodynamics only playing a secondary role (Figure 21). In a recent work, Kantsler *et al.* showed that the flagella of the *Chlamydomonas* prevents the cell body from touching the surface and creates an effective torque that turns the body away from the surface at a finite scattering angle. They could also show that longer flagella led to sharper turns away from the surface indicating the importance of the contact interactions. They then exploited the understanding of these

scattering angles to design a microfluidic ratchet that could rectify the swimming of wild type *Chlamydomonas* (Figure 19B).[109]

In both the cases described above, of bacteria and *Chlamydomonas*, we see that the flagella play a key role in determining the fate of the micro-swimmer close to a surface either through resulting hydrodynamic interactions or direct contact interactions. In our experiments, we use artificial spherical colloidal particles which lack the functional and geometrical complexity of biological micro-swimmers. However, they still create hydrodynamic and chemical fields around them which are significantly modified in the proximity of a confining surface.[124] In the following sections, I will describe experiments performed to understand the interactions between artificial phoretic colloids and impenetrable surfaces. Key results from numerical simulations performed by our theoretical collaborators, which provide insights into the physical mechanism of the experimentally observed interactions will also be described. Our observations are further exploited to create a guidance system for the self-phoretic colloids that does not involve the use of any external fields.[125,126]

2.2 Results

2.2.1 Orientation of phoretic Janus micro-swimmers at planar walls

We fabricate Janus particles with a SiO_2 core (5 µm and 2 µm) and a thin Pt cap (7 nm) as described in Appendix A. In the presence of H_2O_2 these particles self-

propel due to the phoretic flow fields induced by the asymmetric distribution of chemical products around them (see Chapter 1 for details on the mechanism). Within our experimental chamber, we observe that over long periods of time the particle trajectories are largely restricted to be near the bottom surface much like bacteria. To understand if this is due to a simple wall accumulation mechanism that is characteristic of any self-propelled system, or a more complex wall-entrapment mechanism due to preferential orientation of particles close to surfaces, we make our observations at high magnification close to the surface enabling us to keep track of particle orientation.

Initially, the particles are introduced into the system with no H_2O_2. After sedimentation, we find the particles randomly distributed over the substrate and most of the 5-μm particles have their much denser (compared with the SiO_2 cores) Pt caps oriented downward. Under an optical microscope in the top-down view, these particles look like dark circles since the Pt cap absorbs the illumination light of the microscope (Figure 22 Inset top) The smaller 2 μm particles have a slightly wider distribution of orientations due to the greater effect of thermal noise (data not shown). In both cases, all the particles are seen in the same focal plane of the microscope, which indicates that they are at similar vertical distances from the substrate.

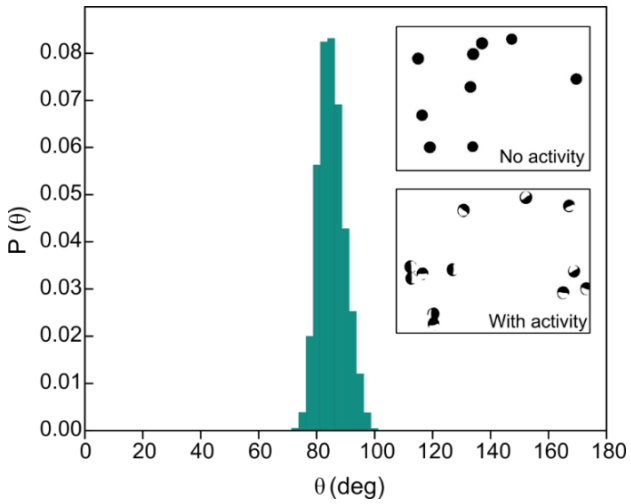

Figure 22: Experimentally measured probability distribution of θ for active particles. Inset: Snapshots showing the system of Janus particles without and with activity. Activity changes the bottom heaviness induced θ = 0 to θ = 90°.

On addition of H_2O_2 to the system, we observe a systemic and consistent change in the orientation of Pt caps. Within the first second, the Pt caps of the active particles change their orientation from caps facing downwards (θ = 0 deg) to caps being parallel to the bottom surface (θ = 90 deg) (Figure 22). Following this reorientation, the active particles start moving parallel to the substrate in the direction away from the catalytic caps. Due to this preferential orientation of the particles close to the surface (Figure 22 Inset lower) and since the Janus particles propel away from their Pt caps, their motion is confined to a 2D plane just above the surface leading to the observed accumulation near boundaries. Instead of the sedimented particles, even if we begin with active particles in the bulk, upon approaching the surface, they assume this stable orientation. It should be noted that the active particles possess enough self-

propulsion velocity to overcome the gravitational force downwards in both the cases of 2 and 5 μm particles. Qualitatively this is similar to the steady angle at which bacteria swim close to surfaces due to near-wall hydrodynamic effects[122], although the mechanism leading to this effect is quite different in the two cases as I will describe in the following sections.

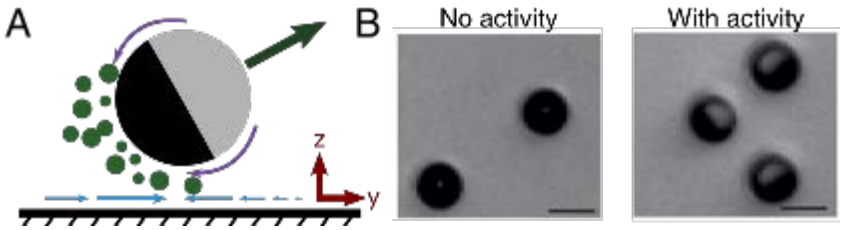

Figure 23: Interactions of phoretic Janus particles with surfaces. (A) Schematic illustrating the several contributions between a self-phoretic particle and a nearby surface. The green dots represent the solute being produced due to the catalytic reaction at the cap. The purple arrows indicate the torques arising from the bottom heaviness of the particle and the hydrodynamic interactions. Blue arrows indicate the chemi-osmotic slip induced on the surface by the confinement of the solute near the surface. (B) Optical microscopy images showing that the particles that sedimented to the bottom surface in a water suspension (inactive system) tend to align with their Pt caps facing downwards (in the image one sees transparent SiO_2 on top of heavily absorbing Pt). However, on addition of H_2O_2 (active system), the particles reorient their symmetry axis parallel to the bottom surface and can be seen as half-covered circles in the right micrograph where dark semi-spheres correspond to the Pt cap and the SiO_2 parts that do not absorb the light appear lighter.

This change in orientation of catalytically active particle close to an impenetrable wall can be explained by considering the different interactions that exist between them. (Figure 23A) First, the particle drives long-range flows in the suspending solution. These flows are reflected from the wall, coupling back to the particle (hydrodynamic interaction). Second, the particle's self-generated solute gradient is modified by the presence of the wall (green dots

in Figure 23A). The wall-induced modification of the solute concentration field can contribute to translation and rotation of the particle ('phoretic interaction'). In particular, when the solute interacts more weakly with the inert region of the particle than with the catalytic cap and both interactions are repulsive, the confinement and accumulation of solute near the substrate tends to drive rotation of the cap away from the substrate. On the other hand, the bottom heaviness of the particle, along with the hydrodynamic interactions of the particle with the substrate, tends to drive the rotation of the cap towards the substrate. Finally, the inhomogeneous solute distribution along the wall induces a solute gradient-driven 'chemiosmotic' flow along the substrate (blue arrows in Figure 23A). For repulsive solute–substrate interactions, this surface slip velocity is directed quasi-radially inward towards the particle, driving a particle-uplifting flow in the suspending solution and causing the particle cap to rotate away from the substrate. (Figure 23B)

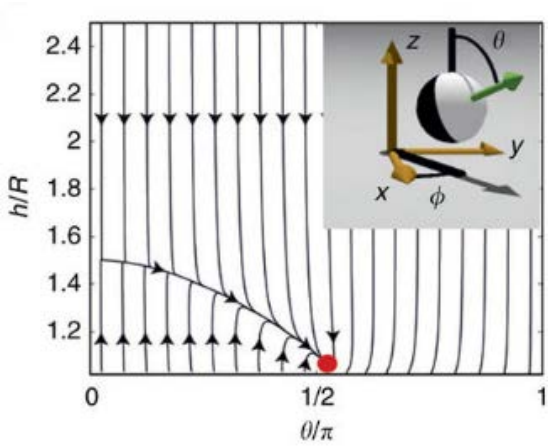

Figure 24: The phase portrait obtained from numerical simulations for a bottom-heavy particle with R=2.5 μm at an infinite planar wall oriented with its normal parallel to the direction of gravity. The phase portrait is calculated at $b_{inert}/b_{cap}=0.3$ and $b_w/b_{cap}=-0.2$, where b_{inert} and b_{cap} are the surface mobilities at the inert and catalytic faces of the particle, respectively, and b_w is the surface mobility at the wall. The phase portrait indicates that a particle will rotate to its steady-state orientation $\theta=\theta_{eq}\approx 90°$ for all initial conditions.

Numerical analysis of this model system shows that depending on the relative strengths of these interactions (that is, the parameters characterizing the surface chemistry of the particle and the wall), the various contributions to rotation discussed above may balance at a steady height h_{eq} and orientation $\theta_{eq}\approx 90°$, and that this steady state is robust and stable against perturbations in height and orientation (Figure 24). The particle cap orientation would therefore evolve to $\theta_{eq}\approx 90°$ (that is, the symmetry axis almost parallel to the substrate) from nearly all initial orientations, including a cap-down one as observed in our experiments. More details about the numerical simulation are provided in Appendix B.

2.2.2 Orientation of phoretic Janus active particles close to side steps

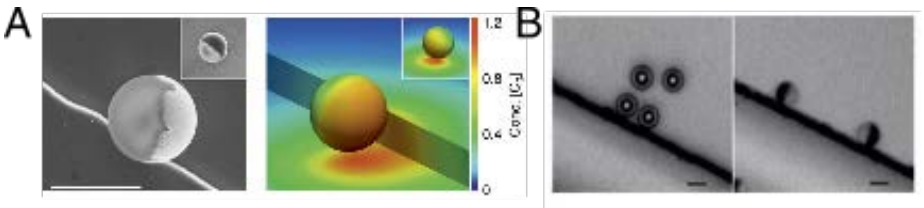

Figure 25: Interactions of phoretic Janus particles with a side step. (**A**) Left: scanning electron microscopy (SEM) image of a spherical Janus motor on a silicon substrate with a silicon step. The lighter part of the Janus particle corresponds to Pt,

while the grey part is the SiO2; scale bar, 2 μm. Right: Color-coded steady-state distribution c(r) of reaction products around a half-covered Janus particle at an inert wall and a step with height h_{step} =R, where R is the particle radius. The colour map shows c(r) at the surfaces of the particle and substrate. The insets show the particles on a flat surface. (**B**) Left: An active Janus particle approaching a step; after direct contact with the step, it reorients until its propulsion axis is parallel to the step. R=2.5μm, h_{step} =800 nm, 2.5%vol. H_2O_2. (b) Micrograph of Janus colloids (R=2.5 μm) in the vicinity of the step with height h_{step} =800 nm. In the absence of H_2O_2 (left image), the step (seen as a black line) has no influence on the orientation of the particles, (their caps are facing downwards, same as far from the step). On addition of fuel (right image), the particles orient with their symmetry axis parallel to both the bottom surface and the step. Scale bars, 5 μm

In the next set of experiments, we explore if similar interactions can induce an orientational attraction to a side step as similar phoretic and hydrodynamic interactions must exist in the presence of this second confinement as well (Figure 25A). In Figure 25B, we show snapshots from an optical microscopy video recording of Janus active particles in the vicinity of a step with h_{step}= 800 nm (see Appendix A for details about the precise micro-fabrication of these step-like features on a glass substrate). Similar to the case depicted in Figure 23B, in the absence of H_2O_2 the particles are initially oriented cap down. After addition of H_2O_2, the particle caps turn parallel to the substrate and the particles start moving in random directions until they encounter a step. On encountering a step, the particles stop, reorient and continue self-propelling along the step (Figure 26). These observations confirm our hypothesis that the presence of a side step near active particles, even if small compared with the particle radius, has an influence on their orientation. Every time the Brownian fluctuations tend to rotate the particle away from this stable orientation parallel to both the confinements, the torques from the various

interactions between the active particle and the walls counter-act to rotate the particle back to this stable orientation.

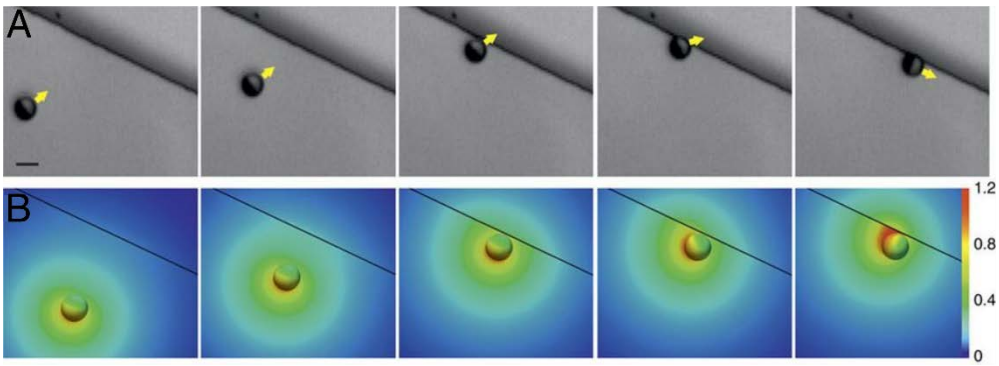

Figure 26: An active Janus particle approaching a step. (**A**) After direct contact with the step the particle reorients until its propulsion axis is parallel to the step. R=2.5 μm, h_{step} = 800 nm, 2.5%vol/vol H_2O_2. (**B**) Numerically calculated steady-state distribution c(r) of reaction products around half catalyst-covered Janus sphere as a function of the step distance and the cap orientation with respect to the step. The colour map shows c(r) at the surfaces of the particle and substrate; c(r) is in units of c_0. Scale bar, 5 μm.

Figure 26A shows snapshots of a typical trajectory of an active particle moving towards a step at an almost perpendicular direction. Once the particle hits the step (Figure 26A third panel) it starts reorienting its axis (Figure 26A fourth panel) towards the direction along the step (Figure 26A fifth panel). We observe that in most cases the complete process of reorientation takes <10 s, independent of the initial angle at which the particle approaches the step. Within the resolution of our experimental equipment, we do not observe any systematic deflection in the trajectory of the particle in the vicinity of the steps. Therefore, we conclude that if any long-range effective interaction exists between the particles and the steps, it must be very weak. We attribute the

suppression of the motion of the particles in the direction normal to the step upon collision to purely steric interactions.

Figure 26B shows the distribution of the reaction products around an active particle for particle positions and orientations approximately corresponding to those shown in the experimental micrographs in Figure 26A. When the particle is far away from the step (Figure 26B first and second panels), approaching it in a head-on direction, the generated concentration field confirms the expected mirror symmetry with respect to the plane defined by the motion axis and normal to the substrate. As a result of this symmetry, there are no activity-induced rotations and the particle stays on its head-on track (up to Brownian rotational diffusion) towards the step. However, closer to the step, a head-on collision becomes unstable to small fluctuations of the propulsion axis, as any such fluctuation gets amplified by the build-up of asymmetric product distribution in the region between one side of the particle and the step (Figure 26B fourth panel). This eventually leads to the reorientation of the motion axis parallel to the step (Figure 26B fifth panel).

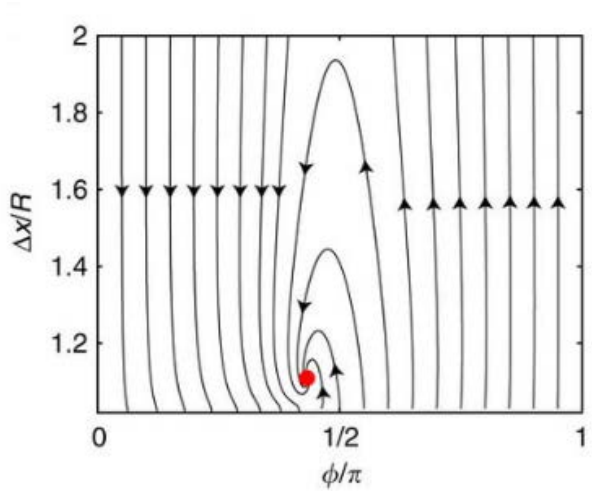

Figure 27: Phase portrait similar to the one in Figure 24, but in absence of gravity. All other parameters are as in Figure 24; this portrait captures qualitatively the effect of the vertical step wall.

Numerical simulations with the same interaction parameters used for the case of a single surface show that for this second confinement, for which gravity plays no role, a similar sliding along the wall attractor emerges with $\varphi_{eq} \approx 90°$, that is, with the particle oriented with its axis almost parallel to the vertical wall. The combination of the two sliding states thus aligns the axis of the particle along the edge formed by the two walls as observed in experiments. It is noteworthy that although this second fixed point appears to have a smaller basin of attraction, it should capture the whole $\varphi \leq \pi/2$ range. A particle on a trajectory that 'crashes' into the vertical wall would diffuse along the wall until it reaches the basin of attraction in the vicinity of $\varphi_{eq} \approx 90°$ (Figure 27).

2.2.3 Effects of the step height on the capture efficiency

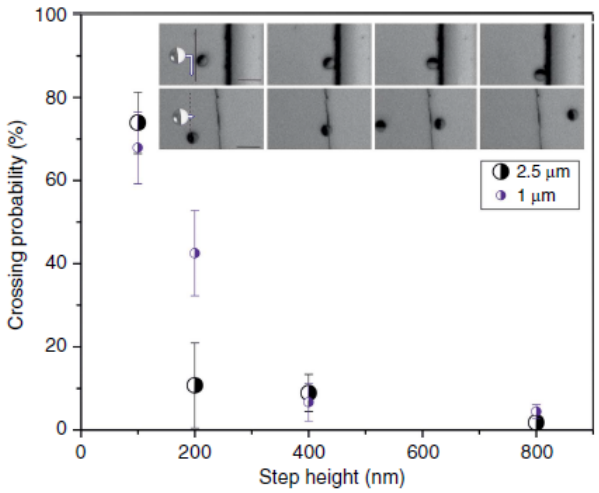

Figure 28: A summary of the crossing behaviour of Janus SiO_2-Pt particles of different sizes at several values of h_{step}; the error bars are s.e.m. Inset: a sequence of micrographs showing a Janus particle with R=2.5µm approaching a step with h_{step} =800 nm, reorienting and then moving parallel to it (upper row). Micrograph sequence of a Janus particle, 2.5 µm, passing over a step, h_{step} =100 nm (lower row). Scale bars, 10 µm (all).

We observe that sub-micrometre steps can capture, and guide particles as shown in Figure 28 (inset top). To evaluate the minimum height h^*_{step} that can still influence the trajectory of the particles, we fabricated a set of patterns with h_{step} varying in a range from 100 to 1000 nm. The results for the two different particle sizes show that h^*_{step} decreases as the particles size increases. In Figure 28 we summarize the responses of R = 1 µm and R = 2.5 µm active particles to variation of the step height. Both types of particles simply swim over the step of 100 nm height with no effective reorientation observed (Figure 28B inset bottom). For R = 2.5 µm particles, steps of height 200 nm already

ensure ~90% docking of particles upon collision with the step, while a significant fraction of the *R* = 1 µm particles managed to pass over the 200-nm-high step, and 400-nm-high steps were required for efficient docking. From Figure 28 we infer that $\mathrm{h}^*_{\mathrm{step}}/R$ is smaller for larger particles. This effect is possibly due to the combination of larger effect of Brownian noise in the case of smaller particles and the fact that the heavier R = 2.5 µm particles are closer to the bottom surface allowing them to interact with features of much smaller sizes as compared to the R = 1 µm particles.

2.2.4 Guidance of active particles by low-height topographic steps

A bit of context: *Several applications have been envisioned for micro systems such as the self-propelled Janus particles that we use in our experiments.*[127–130] *These applications range from environmental sensing*[131–133] *to cargo transport*[134–136] *and targeted drug delivery*[137–139]*. A major barrier to achieving systems capable of these tasks has been Brownian rotation which constantly randomizes the direction of these micron sized particles. In order to achieve directional control of these active particles, two main methods of guidance have been employed with varying degrees of success. The first one uses controlled spatial gradients of 'fuel' concentration.*[140–144] *This approach suffers, however, from severe difficulties in creating and maintaining chemical gradients, and the spatial precision of guidance remains rather poor. The second approach relies on the use of external magnetic fields in combination*

with particles with suitably designed magnetic coatings or inclusions.[145,146] This proved to be a very precise guidance mechanism, which could be employed straightforwardly for the case of tubular[147], but difficult to extend to the case of spherical colloids, where it requires sophisticated engineering of multilayer magnetic coatings[148–151]. In addition, individualized guidance of specific particles is difficult to achieve without complicated external apparatus and feedback loops.[147] The advantages of autonomous operation are thereby significantly hindered. Here I will describe how particle-wall interactions can be exploited to create an effective guidance system for chemically active particles.

The step-like topography and particle alignment along step edges can be used to guide active particles, as shown in Figure 29A. This corresponds to particles in a well structure with straight steps. Upon collisions, the particles align along the steps and follow them (Figure 29A). In the same well-like structure, particles eventually encounter a corner and remain stuck there until a strong Brownian perturbation enables them to align with the adjacent step (Figure 29B). This process typically takes tens of seconds. In the case of a post-like structure as displayed in Figure 29C, particles also follow the straight features but fail to reorient and manoeuvre around the 270° corner. These findings suggest that certain critical value must exist for reflex angles between features above which guidance along the step is lost.

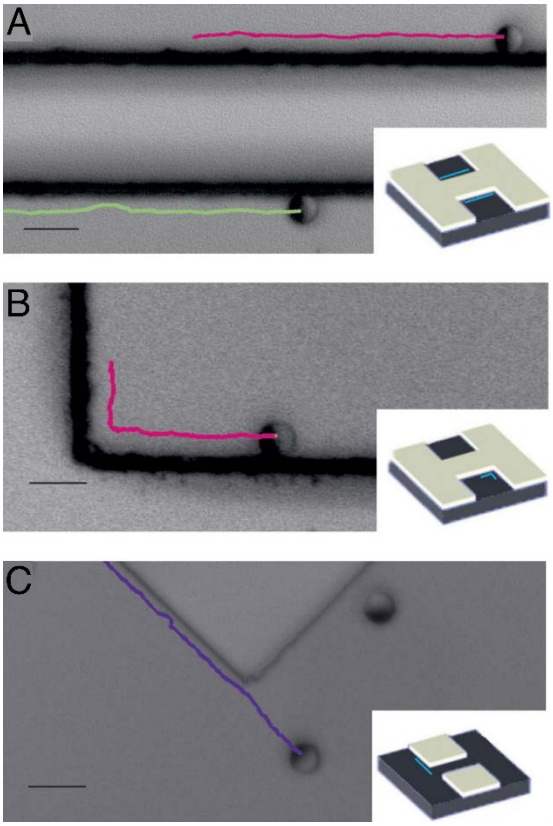

Figure 29: Janus particle trajectories close to topographical steps. (A) A micrograph showing trajectories of two R=2.5 μm Janus particles following a straight step. (B) A Janus particle tracked while manoeuvring around a 90° corner. (C) A Janus particle unable to follow a reflex angle of 270°. The insets show schematically the structures of wells A,B and posts C. The blue lines on the insets schematically indicate the position of Janus particles in actual experiments. Scale bars, 10 μm.

The strongest evidence for the wall entrapment effect of these active particles comes from the experiments performed in proximity of cylindrical posts. If the swimmer-wall interactions were to be purely active Brownian, where the particles approach a flat wall, stay oriented for a characteristic time before reorienting away from the surface, one wouldn't expect them to be able to follow along cylindrical posts as this would involve constantly reorientation at

every time step to be able to follow along the curvature of the posts. However, in our experiments we observe that these phoretic swimmers follow circular trajectories around cylindrical posts of different curvatures.

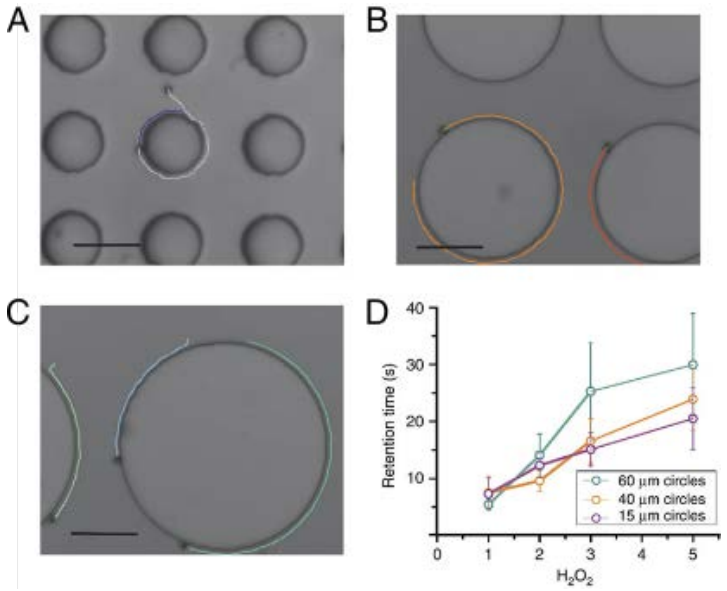

Figure 30: Trapping of phoretic Janus particles around cylindrical posts. (**A-C**) Optical snapshots of R=1 μm active particles moving for 12 s around circular posts of 15, 40 and 60 μm diameter d, respectively. Scale bar, 20 μm. (**D**) Average retention time as a function of peroxide concentration for R=1 μm. The average is determined for 15–20 trajectories per data point; the error bars are standard errors of the mean.

In Figure 30A, B, C, paths are shown where particles with R =1 μm circle around posts with the diameter of 15, 40 and 60 μm, respectively, for more than 12 s. We find that the retention time of active particles at the circular posts increases with increasing peroxide concentration, as displayed in Figure 30D. At 1%, few particles completely circle around a whole post and, in most cases, the active particles detach from the post before a complete revolution (at lower peroxide concentrations, the particles hardly move and get easily stuck at the steps;

thus, measurements were not considered). At 2% H_2O_2, the path length along the posts is increased and likewise in 3 and 5% H_2O_2, where many particles circle around posts multiple times. As the retention time increases with the concentration of H_2O_2, we conclude that it is the activity of the active particles that is directly responsible for the effective particle attraction to the posts and for the occurrence of the sliding attractor: it is the net result of the particle-step hydrodynamics and confinement-induced modification of the distribution of the oxygen concentration. The strength of both effects depends on the fuel concentration: increased fuel concentration leads to a higher production rate of solute (that is, stronger phoretic and chemi-osmotic interactions) and a higher self-propulsion velocity (that is, stronger hydrodynamic interactions). The finite retention time is set by the competition between activity-induced effective attraction to the post side walls and rotational diffusion. Increased fuel concentration increases the strength of the first factor without affecting the second one and therefore increases the retention time. Within the range of radii of posts that we performed our experiments (the smallest of which was larger than 3 $R_{particle}$, a limitation set by the fabrication method used) we do not see a significant dependence of retention time on the curvature of the posts. However, since increasing curvature would require a greater counter-acting torque from the various particle-wall interactions, there must exist a limit where the particle is no longer able to follow the circular posts.[115]

2.3 Discussion and further experiments

The micro-structuring method presented here avoids the use of any external fields and relies solely on the intrinsic properties of the system to guide particle motion. The phenomenology reported here is, in some sense, a mesoscale analogue of the binding of motor proteins to microtubules, to switch to directional motion. However, in distinction to biological nanomotors, the Janus active particles bypass the binding and rather elegantly exploit an effective attraction that stems from the feedback between geometric confinement, and chemical and hydrodynamic activity to achieve guidance.

Besides guiding applications described above, these observations have already helped us in designing new self-assembled micro-gears that are powered by Janus active particles.[152] In experiments performed in collaboration with the Di Leonardo Lab in Rome, we show that a small, well-defined number of artificial micromotors can self-organize in highly ordered configurations around a larger passive micro-object and propel it in a steady unidirectional motion. We begin with a suspension containing the inert gear shaped structures shown (grey in Figure 31) and active Janus particles. Over time, since the Janus particles are self-propelled and swim close to the surface where the inert structures are sedimented, they interact with the edges of the micro-gear. By choosing a convenient relationship between the lengths of the sides of a micro-gear, we force the active particles to dock on the gears in a well-defined position and orientation.

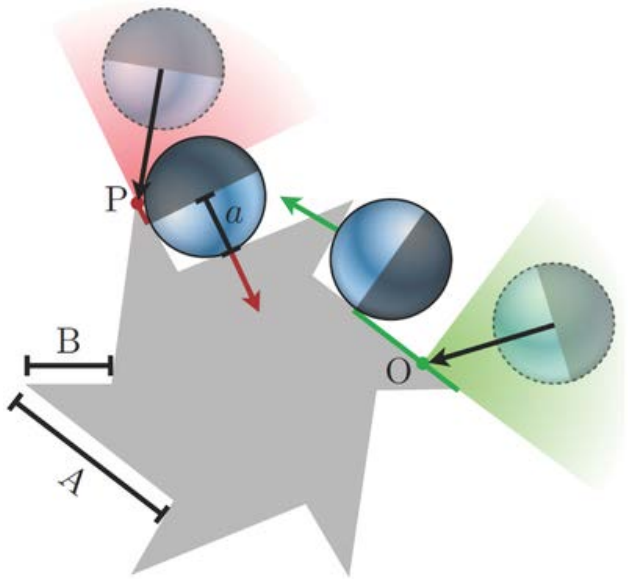

Figure 31: Schematic representation of the two possible docking events leading to a Janus particle stably propelling the microgear.[152]

As a result of the interactions between active particles and micro-gears, two distinct final configurations are possible (see Figure 31). The first is that a particle collides in O coming from the green shaded region, aligns, and docks at the corner propelling the structure in anticlockwise direction. The probability of events of this type is proportional to the length A-a of the green segment representing the locus of possible impact points O. A second docked state occurs when a particle collides in P coming from the red region and gets stuck pushing the structure in the clockwise direction. The probability of these events is proportional to B-a (see Figure 31). By properly designing the lengths of the different segments of the structures, we can ensure that most of the fully occupied structures will have all particles pushing in the same direction, while the fraction of "wrong" assemblies where for example one particle

points in the opposite direction is only (B-a)/(A-a) with the optimal situation being B ≈ a. In our designs B = 3 μm, A = 6.7 μm so that only one structure among ten is expected to form with a misoriented particle.

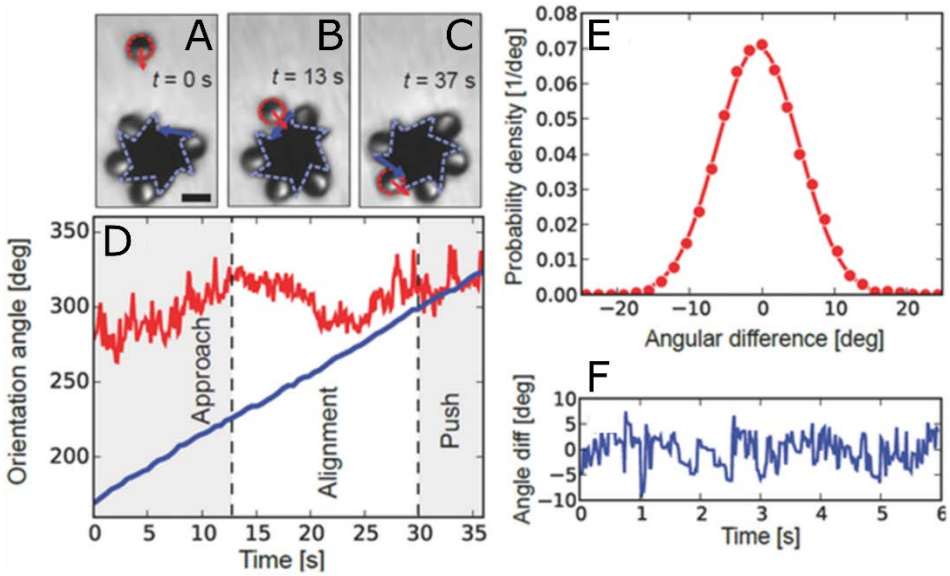

Figure 32: Self-assembly of phoretic Janus particles around inert micro-gear structures (A) Janus particle approaching the gear. Dashed lines represent the tracked shapes and arrows indicate the instantaneous orientation of particle propulsion and of the colliding long edge (scale bar is 5 μm). (B) Collision followed by alignment. (C) The Janus particle docks on the gear with an orientation resulting in a maximal applied torque. (D) Temporal evolution of the orientation angle for the gear (blue line) and of the Janus particle (red line), during the approach, alignment, and pushing stages. (E) Probability distribution of the angle formed by a docked Janus particle and the corresponding long edge. (F) Typical fluctuations of the angle formed by the orientation vector of the Janus particle and the corresponding long-tooth edge as a function of time.[152]

Figure 32 shows a typical docking event for a 5 μm Janus particle which is composed of the same three main stages that were observed in the interactions between the particles and rectangular wells (Figure 26): the particle moves freely on the surface until it encounters a gear (Figure 32A). The

particle touches the long edge and aligns along it as it would along a side step (Figure 32B), and finally, the particle slides along the long edge until it arrives at the corner formed by short edge, gets stuck there, and starts pushing with maximal applied torque (Figure 32C). Figure 32D which tracks the orientation angle of the gear edge and the orientation vector of the particle shows that, once the alignment has occurred, the two orientation angles merge onto the same curve and the assembly moves as a rigid body. And once the particle is trapped in the corner of the gear its orientation is stably locked around the orientation of the long edge of the gear showing only small fluctuations (Figure 32E, F).

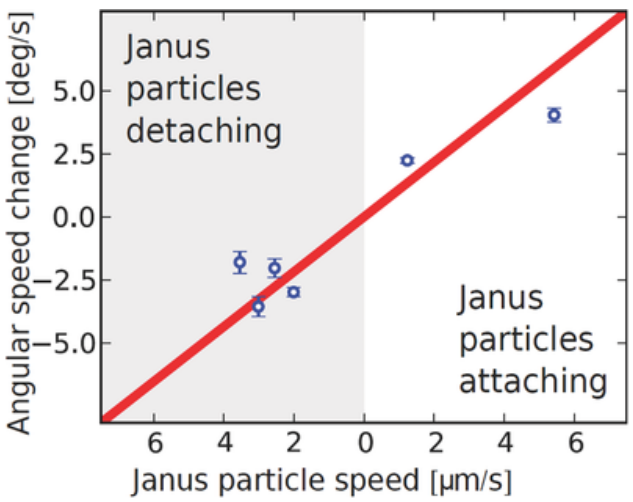

Figure 33: Change in angular speed (circles) of the microgear when one single Janus particle attaches (right) or detaches (left) as a function of the particle speed as measured before attachment or after detachment. The full line is a linear fit passing through zero.[152]

When a Janus particle collides, aligns, and docks to the gear, we usually see a clear increase of the rotational speed. Occasionally we also observe that a stuck

Janus particle reorients, because of Brownian fluctuations, and leaves the structure. These events are instead accompanied by a decrease in rotational speed of the gear. In both cases the change of the rotational speed is approximately proportional to the free propulsion speed of the Janus particle far from the structure (Figure 33).

2.4 Concluding remarks

In this chapter I have reported experimental results showing the dynamics of chemically active Janus active particles at geometrically patterned substrates. Employing a lithography-based method to fabricate sub-micrometre topographic features in the form of rectangular stripes, square posts, cylindrical posts or square wells, we have demonstrated that the motion of chemically active Janus active particles can be restricted to proceed along these sub-micron patterns for significant time intervals. Furthermore, the motion along the circumference of cylindrical posts reveals that the retention time increases with increasing H_2O_2 concentration. This allows us to unequivocally identify the particle' s chemical activity, which modulates the distribution of the phoretic slip at the particle surface and thus the hydrodynamic interactions with the nearby topography, as playing a dominant role in the observed phenomenology.

A minimal continuum model of self-diffusiophoresis captures the qualitative features of the experimental observations if one accounts for the difference in

material properties of the two parts of the colloid and for chemiosmotic flows induced at the wall. This latter aspect highlights the need for models that explicitly include chemical activity, without which a no-slip boundary condition would apply at the wall. The model exploited here allows us to understand the emergence of states of motion along the edges as a simultaneous attraction to two fixed-point attractors corresponding to steady sliding states along the bottom wall and along the vertical wall of the step. The results presented here open the possibility of robust guidance of particles along complex paths via minimal surface modifications, that is, by sculpting a pattern with the edge in the desired shape.

While it is possible by using this system to switch the particle motion behaviour from diffusive to directional, it is still hard to control the polarity of the particle motion. When a particle approaches a flat wall, there is an equal probability for the particle to go in either direction along the wall. Similarly, when the particle encounters a cylindrical post, there is an equal probability of clockwise or anti clockwise trajectories. Another drawback of this system is that it can only guide individual particles that encounter the micro-patterned structures due to 'chance'. It excludes any possibility for a population scale migration of particles. Any effective guidance system for active particles should allow for control on both the polarity of directional motion and allow for the scaling of the system to larger populations. In the following chapter, I will use the

phenomenon that we have uncovered here to build a system that can generate a current of active particles in a desired direction.

2.5 Appendix A: Preparation of Janus particles and microstructures used for guidance experiments

Janus particles: The Janus particles were obtained by electron-beam deposition of a Pt layer on a monolayer of silica colloids. The monolayers were prepared either by a Langmuir-Blodgett (LB) method or a drop-casting method. For the LB method, silica colloids (R = 1 μm; Sigma-Aldrich) were first surface-treated with allyltrimethoxysilane to make them amphiphilic. A suspension of these particles in chloroform-ethanol mixture [80%:20% (v/v)] was carefully dropped onto the LB trough and compressed to create a closely packed monolayer. The monolayer was then transferred onto a silicon wafer at a surface pressure of 20 mN/m. The silicon wafer was then shifted to a vacuum system for the electron-beam deposition of a thin layer of Pt (10 nm) at 10^{-6} mmHg. The Janus particles were released into deionized water using short ultrasound pulses. The suspension of Janus particles in water was stored at room temperature. The monolayers of R = 2.5 μm silica particles (Sigma-Aldrich) were prepared by drop-casting the suspension of colloids onto an oxygen plasma–treated glass slide. The plasma treatment was used to make the glass slide hydrophilic and ensure uniform spreading of the particle suspension. The solvent was subsequently removed by slow evaporation. The Pt deposition step was identical to the one used for R = 1 μm particles.

Microstructures: Photoresist patterns were prepared on 24 mm square glass slides or on silicon wafers. This choice is made depending on the type of microscope used. For the case of inverted microscopes where the illumination light has to pass through the substrate, transparent glass slides were used. For the upright microscopy, silicon wafers offer better contrast.

In case of positive photoresist, AR-P 3,510 was spin coated onto the cleaned substrate at 3,500 r.p.m. for 35 s, followed by a soft bake using a hotplate at 90 °C for 3 min and exposure to ultraviolet light with a Mask Aligner (400 nm) for 2 s. Patterns were developed in a 1:1 AR300-35:H_2O solution. In case of negative photoresist, a layer of adhesion promoter TI prime was spin coated on the substrate during 20 s at 3,500 r.p.m. After 2 min of drying at 120 °C, the negative photoresist was coated employing a program of 35 s spinning at 4,500 r.p.m., followed by 5 min baking at 90°. The exposure was carried out with a Mask aligner for 2 s followed by 2 min on the hotplate at 120 °C. Finally, an additional exposure to 2 s ultraviolet light is applied and the patterns were developed in pure AZ726MIF. The steps were obtained by e-beam deposition of the desired material (SiO_2, Si) in the desired thickness. By dissolving the photoresist layer in acetone, the pattern structures of the substrate were exposed.

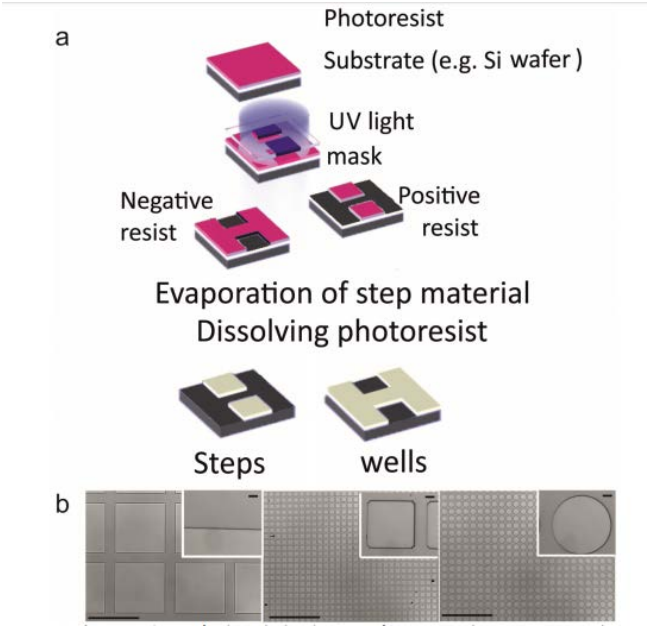

Figure 34: Lithography based creation of patterns. (**A**) Schematic representing the lithography- based method to create submicron step and well structures for particle guidance. (**B**) Optical images of the resulting patterns; the scale bar in the inset correspond to 10 µm while the scale bars in the main images correspond to 500 µm.

2.6 Appendix B: Notes on theoretical modelling

This analysis was carried out by Dr. William E. Uspal, Dr. Mihail N. Popescu and Dr. Mykola Tasinkevych

We model particle motion within a continuum, neutral self-diffusiophoretic framework. A particle emits solute at a constant rate from its catalytic cap. The number density $c(\mathbf{r})$ of solute is quasi-static, where $\mathbf{r}$ is a position in the fluid. The solute field is governed by the Laplace equation $\nabla^2 c=0$ and obeys the boundary conditions $-D\nabla c\cdot\mathbf{n}=\kappa$ on the catalytic cap and $-D\nabla c\cdot\mathbf{n}=0$ on the inert face of the particle and the substrate, where κ is the rate of emission (uniform

over the cap), D is the diffusion coefficient of oxygen and $\mathbf{n}$ is the local surface normal. Our model neglects the details of the catalytic reaction, which might involve the transport of charged intermediates.[153,154] Nevertheless, we expect this model to capture the gross effects of both near-wall confinement of the solute field and HI with nearby walls. The surface gradient of solute drives a surface flow ('slip velocity') $\mathbf{v}_s$ in a thin fluid layer surrounding the particle surface $\mathbf{v}_s(\mathbf{r}) = -b_s(\mathbf{r})\nabla_{||}c$, where $\nabla_{||} = (\mathbf{I} - \mathbf{n}\otimes\mathbf{n}) \cdot \nabla$. $\mathbf{I}$ is the 3 × 3 unit matrix.

The coefficient $b_s(\mathbf{r})$ of the slip velocity, the so-called 'surface mobility', is determined by the molecular interaction potential between the solute and the particle surface[155]. We allow $b_s(\mathbf{r})$ to differ between the inert and catalytic regions, but assume it is uniform in each region, that is, take $b_s = b_{inert}$ or $b_s = b_{cap}$. In addition, when we consider the effect of chemiosmotic flow on the substrate, we calculate a wall slip velocity $\mathbf{v}_w(\mathbf{r}_s) = -b_w\nabla_{||}c$, where b_w is a constant. We always take the interaction between the solute and particle surface to be repulsive, that is, $b_s < 0$, so that the model is consistent with the observed motion of particles away from their caps.

The velocity $\mathbf{u}(\mathbf{r})$ in the fluid is governed by the Stokes equation $-\nabla p + \eta\nabla^2\mathbf{u} = 0$ and the incompressibility condition $\nabla\cdot\mathbf{u} = 0$, where $p(\mathbf{r})$ is the fluid pressure and η is the dynamic viscosity of the solution. The velocity obeys the boundary conditions $\mathbf{u} = \mathbf{v}_w(\mathbf{r})$ on the substrate and $\mathbf{u}(\mathbf{r}) = \mathbf{U}^a + \mathbf{\Omega}^a \times (\mathbf{r} - \mathbf{r}_O) + \mathbf{v}_s(\mathbf{r})$ on the particle surface, where $\mathbf{r}_O$ is the position of the particle centre

and $\mathbf{U}^a$ and $\mathbf{\Omega}^a$ are the contributions of activity to the translational and rotational velocities of the particle, respectively. To obtain $\mathbf{U}^a$ and $\mathbf{\Omega}^a$ for a given position and orientation of the particle, we first solve for $c(\mathbf{r})$ numerically, using the boundary element method. The slip velocities $\mathbf{v}_s$ and $\mathbf{v}_w$ are then calculated from $c(\mathbf{r})$. Inserting the slip velocities in the boundary conditions and requiring that the particle is force and torque free, we solve the Stokes equation numerically via the boundary element method, to obtain $\mathbf{U}^a$ and Ω^a in terms of characteristic velocity scales $U_0 \stackrel{\text{def}}{=} |b_{cap}|\kappa/R$ *and* $\Omega_0 \stackrel{\text{def}}{=} U_0/R$. Additionally, $c(\mathbf{r})$ is calculated in terms of a characteristic concentration $c_0 \stackrel{\text{def}}{=} \kappa R/D$.

When we include the effects of gravity, we adopt the geometrical model of Campbell and Ebbens[156], taking the Janus particle as having a platinum cap that smoothly varies in thickness between a maximum of 7 nm at the pole and zero thickness at the particle equator. The gravitational contributions to particle velocity, $\mathbf{U}^g$ and $\mathbf{\Omega}^g$, are calculated using standard methods.

We obtain complete particle trajectories by numerically integrating $\mathbf{U}=\mathbf{U}^a+\mathbf{U}^g$ and $\mathbf{\Omega}=\mathbf{\Omega}^a+\mathbf{\Omega}^g$. Further details of the numerical method are given in ref. [124]. We note that the assumption that the solute field is quasi-static is valid in the limit of small Peclet number $\mathrm{Pe}=U_0R/D$. We have neglected the inertia of the fluid, which is valid for small Reynolds number $\mathrm{Re}=\rho U_0 R/\eta$, where ρ is the mass density of the solution. These dimensionless numbers are

Pe≈4 × 10^{-3} and Re≈10^{-5} for a 5-μm-diameter catalytic Janus particle that swims at 6 μm s^{-1} [157].

3.Directed flow of active particles through alignment interactions

3.1 Introduction

A micro particle suspended in a liquid is subject to random collisions with the solvent molecules. This is a fluctuating force that changes direction and magnitude frequently compared to any other timescale in the system and averages to zero over time. Within a liquid, there is also a viscous drag force that dampens the motion arising from the fluctuation force. These two effects are in fact not independent. The amplitude of the fluctuating force is determined by the viscosity and temperature of the liquid and is referred to as thermal noise. The effect of thermal noise on a small particle was first observed by Robert Brown in 1827 when he described small particles of plant pollen jiggling around in liquid. This characteristic random motion of small particles suspended in liquid is called Brownian motion.

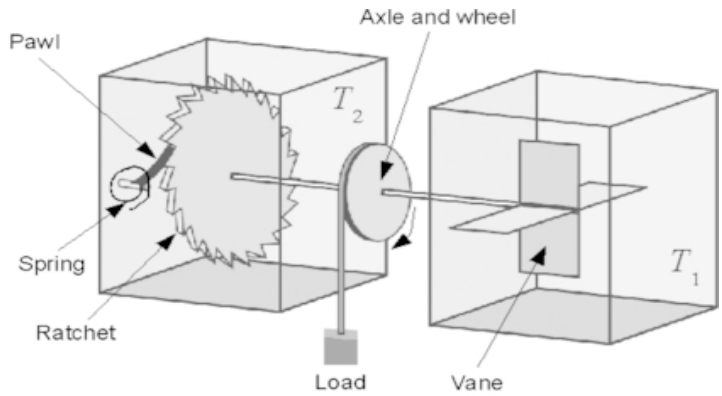

Figure 35: Feynman's ratchet composed of a ratchet engaged to a pawl and a spring in a thermal bath at temperature T_2 and connected to a vane in a thermal bath at temperature T_1[158].

At equilibrium, the effect of thermal noise is symmetric, even in an asymmetric medium, and Brownian motion cannot be used to obtain net work or directed motion. This was illustrated beautifully in the context of a microscopic 'ratchet and pawl' by Richard Feynman[159] who considered a wheel that could rotate in only one direction and was connected to a windmill whose wanes are surrounded by a gas at finite temperature with $T_1 = T_2$ (Figure 35). Occasionally, an accumulation of collisions by the gas molecules on the vanes could enable the wheel to rotate by one notch in the allowed direction but presumably never in the forbidden direction. This directed rotation of the wheel could then be harnessed to perform some useful work, such as lifting a small object against gravity, a result then would be in direct violation of the second law of thermodynamics. Feynman resolved the paradox by observing that for the random collisions to cause a rotation of the ratchet, the ratchet and pawl need to be microscopic as well and therefore also subject to thermal fluctuations. This would then occasionally cause the pawl to disengage from the ratchet and allow it to move in the backward direction. By comparing the rates of the two processes – rotation in the forward and backward directions – Feynman showed them to be equal in an isothermal system and net motion cannot actually be achieved despite the anisotropy of the system.

However, if the wheel in the system is maintained at a lower temperature to reduce the probability of the pawl disengaging from the ratchet, then net motion can indeed be achieved in this system which is no longer in violation

of the second law. Brownian motion in synergy with a thermal gradient can therefore result in the directed motion of microparticles.

As a practical matter, however, large thermal gradients over small distances are impossible to maintain. An alternative approach to achieve directed motion at the microscale has been to use an energy source other than a thermal gradient. If energy is supplied by external fluctuations, Brownian motion can be coupled with an asymmetric medium to achieve directed motion even in an isothermal system.[160,161]

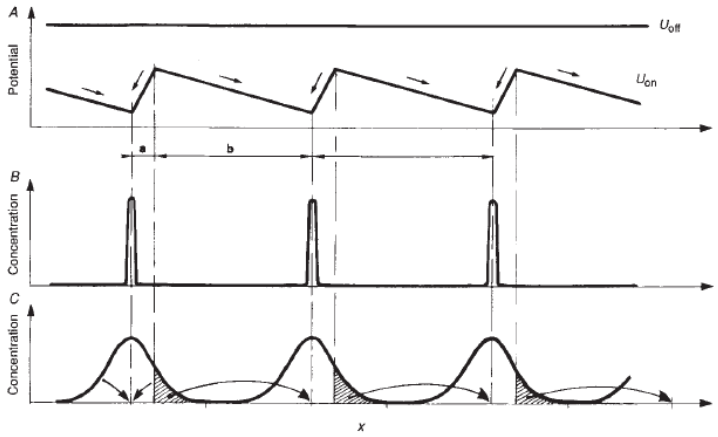

Figure 36: Schematic illustration of a flashing ratchet. (**A**) Shape of the applied asymmetric potential. (**B**) Probability distribution of the particle positions at the end of the *On* period. (**C**) Probability distribution of the particle position at the end of the *Off* period[162].

Consider an asymmetric potential U_{on} that is periodically turned on for time τ_{on} and turned off for time τ_{off} (Figure 36A). The anisotropy of the potential results in two legs of the potential, one of length a, where the force is $-\Delta U/a$ and the other of length b, where the force is $\Delta U/b$ with $a < b$ as shown in Figure 36A.

At the end of the *on* time the particles subject to this potential are trapped at the potential minimums of U_{on} and their spatial probability distribution is represented in Figure 36B. At the start of the *off* time, since the particles are subject to Brownian motion, their spatial probability distribution spreads as a gaussian around the potential minima of U_{on} and is given by:

$$\boldsymbol{P\left(0\middle|x;t_{off}\right)=\frac{\exp\left[-\frac{x^2}{4Dt_{off}}\right]}{\sqrt{4\pi Dt_{off}}}} \qquad (42)$$

as shown in Figure 36C. At the end of the *off* time, once the potential is turned back *on*, where the particles get trapped is dependent on the position of the particles. The *off* time can be regulated such that, owing to the asymmetry of the potential, the turning on process induces a downhill motion of particles, as the particles in the hatched region in Figure 36B now move on to the right, causing a net drift of particles.

The mechanism described above works only because of the thermal diffusion of particles. In the absence of Brownian motion there would be no spread of the probability distribution of the particle position, and there would be no net drift. The energy to gain this net drift however doesn't come from the thermal diffusion of particles but rather from the flashing *on* and *off* of the asymmetric potential and these systems are referred to as *flashing ratchets*.[162–164]

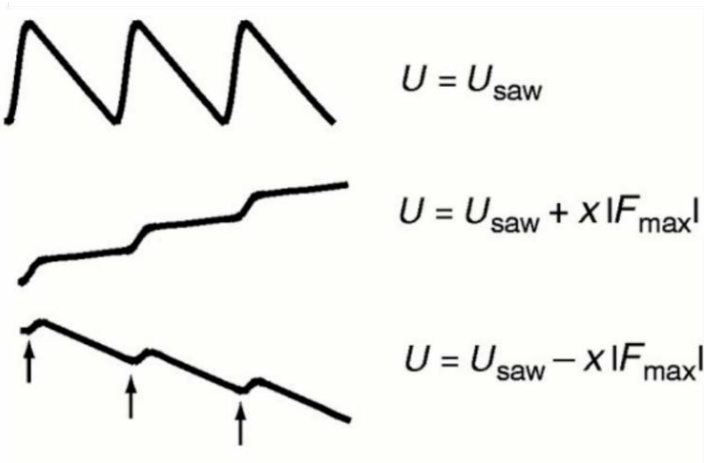

Figure 37: Rocking ratchet: Due to the asymmetry of the imposed potential U_{saw} the force required for the particle to move to the left is lower than the force required to move to the right. When an intermediate force between the two values is applied, the particle can drift freely to the left, but is captured by local potential minima towards the right[165].

Another often used method to drive the rectification of microparticles is that of the *rocking ratchet*[166–172]. In a rocking ratchet, the asymmetric potential U_{saw} is kept constant but a zero averaged fluctuating force is applied externally on the particle (Figure 37)[165]. For a particle trapped in the potential minima of the U_{saw} it requires a different magnitude of force to move towards the left $F_{left} = \Delta U/b$ as compared to the right $F_{right} = -\Delta U/a$ with $F_{left} < F_{right}$. Now, if a zero-averaged oscillating force with $F_{max} < \Delta U/b$ is applied, the particle remains trapped within the minima. But if $\Delta U/b < F_{max} < \Delta U/a$, then with each oscillation the particle moves to the left, but not to the right and a net drift can be obtained (Figure 37). This mechanism will work even without thermal diffusion when a slow oscillation between $\pm F_{max}$ is applied, such as in a periodic square wave. For a Brownian particle, a sub threshold F_{max} slightly smaller than

ΔU/b can be used to cause net drift. However, if the oscillation rate of the force is too high, then no rectification is observed. In such a case, the particle does not have the time to probe the asymmetry of the potential landscape underneath.

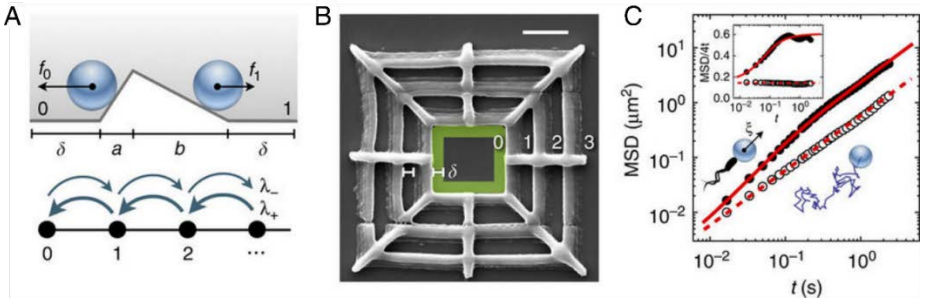

Figure 38: Transport of colloidal particles in bacterial baths (A) Schematic representing the geometric and dynamic features controlling the transitions between 2 metastable states. (B) Scanning electron microscopy image of the 3D structures designed to accumulate colloidal particles in the centre chamber. (C) The mean square displacements of colloidal particles in water (open symbols) and in a bacterial bath (closed symbols).[173]

There are several ways of obtaining the fluctuations that drive the system out of equilibrium and result in the rectification of particles. Koumakis *et al.* for example described a method to exploit the non-equilibrium fluctuations from a suspension of bacteria (Figure 38A).[173] They used photolithography to pattern a potential landscape onto the glass slide on which the colloidal particles are suspended (Figure 38B). In a bacterial suspension, unlike in water, the particles have a finite persistence time in the order of seconds arising from collisions with swimming bacteria (Figure 38C). This persistence time is enough to probe the asymmetric features of the landscape underneath. In contrast to

the case of a rocking ratchet where the fluctuations have a well-defined F_{max}, here the system relies on the probability of the occurrence of a particle being pushed by a force of large magnitude being lower than that of a small magnitude.

Consider the case of Brownian particles hopping between two metastable states 0 and 1 that have the same energy and the same spatial extent as shown in Figure 38A. In an equilibrium thermal bath, the number of particles is equal even if there exists an asymmetrically shaped energy barrier between them. However, if these Brownian particles are suspended in a bacterial bath, there exists a fluctuating noise term with a finite correlation time. In this case, the particles have a finite persistence time and the probability of jumping from 0 to 1 is related to the probability of being pushed by the bath with a force of amplitude ξ larger than the slope of the energy barrier f_0. Since a large ξ will be less frequent than a small ξ, transitions from 1 to 0, that involve climbing over a smaller slope, will be more frequent than the reverse transitions from 0 to 1. The particles therefore tend to spend more time in 0 than in 1 (Figure 38A). The authors of the study built three dimensional asymmetric structures that could accumulate colloidal particles in small regions based on these principles.

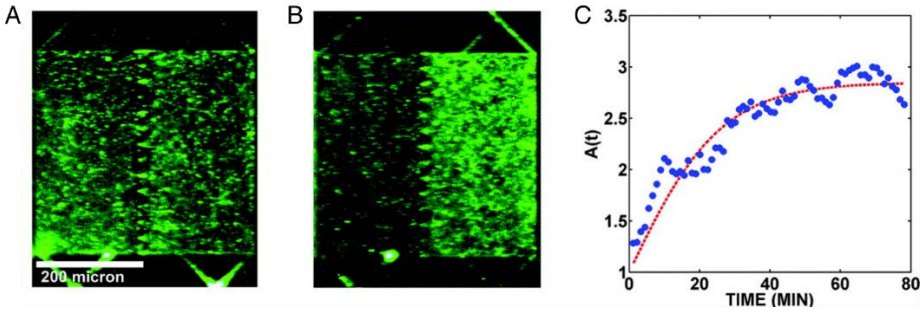

Figure 39: Wall of funnels separate motile bacteria. (**A**) Uniform distribution of bacteria right after injection of bacteria into the chamber. (**B**) Steady state distribution of bacteria after 80 min. (**C**) Evolution of the ratio of density of bacteria in the left and right compartments with time.[174]

Active particles, such as motile bacteria or self-propelled Janus particles, are intrinsically out-of-equilibrium either due to biological processes inside the cell body or chemical reactions happening on the cell surface.[1] In this case, the existence of an asymmetric periodic potential is sufficient to induce the rectification effect without the need for externally imposed fluctuations. These particles inherently have a finite persistence time and can therefore explore the asymmetric landscapes around them. Galajda *et al.* demonstrated that for a system of bacteria swimming in a sample separated into two chambers by asymmetric funnel shaped structures, this structural asymmetry was sufficient to accumulate motile bacteria on one side (Figure 39).[174] Subsequent simulations have identified that the finite run-lengths of bacteria along the walls is necessary to produce the observed effect.[175,176] If the interaction between the bacteria and the asymmetric structures was simply elastic, as would be the case for a purely Brownian particle, the rectification effect was lost. Increasing the run-length along the edges lead to a stronger rectification

effect. In fact, the bacteria do tend to move along the edges for a period longer than their bulk persistence time due to the hydrodynamic attraction of motile bacteria to solid obstacles as described in Chapter 1. So, while a system of active particles intrinsically is out-of-equilibrium and contains the time correlated fluctuations necessary to lead to rectification in the presence of an asymmetric potential, the exact nature of interaction between the active particle and the asymmetric obstacles dictates the efficiency of the rectification.

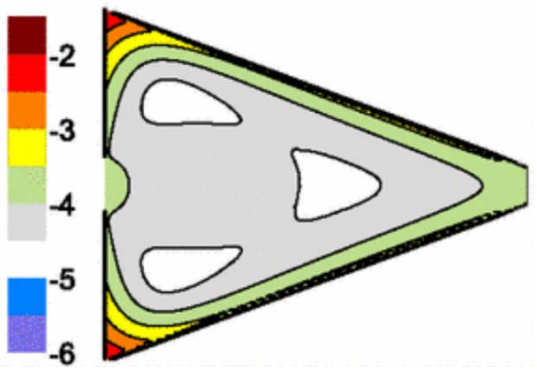

Figure 40: Stationary probability density of particle position in a channel compartment for particles with frictionless collisions at the walls[177].

The case of self-propelled Janus particles was first studied in simulations by Ghosh *et al.*[177] They considered the case of swimming Janus particles in periodic triangular channels, where the collision dynamics at the boundaries are modelled so that the translational velocity upon collision is elastically reflected, whereas the in-plane angle ϕ is modelled to have a frictionless collision such that ϕ remains unchanged along the wall as the particle slides

along it for an average time of the order of τ_R (characteristic rotational diffusion time) until thermal fluctuations redirect it towards the centre of the compartment. This clearly leads to the accumulation of stationary probability distribution (P(x, y)) close to the boundaries (Figure 40), and a net rectification is observed in simulations.

We have however observed in experiments, as described in Chapter 2, that the collision dynamics of self-propelled Janus particles is strongly influenced by the hydrodynamic and phoretic interactions of these particles with nearby obstacles. For spherical silica-Pt Janus particles, a non-intuitive alignment effect exists in the presence of topographical boundaries resulting in the 'pinning' of the particle orientation by the shape of nearby geometrical constraints.[178] In this chapter, I will describe how we exploit this alignment effect and show that the flow of spherical Janus particles can be rectified geometrically by properly shaping the walls of a quasi 1D channel. We begin by developing the principles to design these asymmetric channels taking into consideration the hydrodynamic and phoretic interactions of the active particles with their surroundings. In doing so, we show that intuitively simple asymmetric shapes that lead to directional flow when modelling the self-propelled particle as purely active Brownian or run-and-tumble particles do not actually generate net flows in experiments. We then design asymmetrical channels, considering the alignment effect of active particles near topographical boundaries, that lead to a robust directional current. We also

exploit this effect to develop a set-up that concentrates active particles in confined areas and identify the particle-particle interactions responsible for this accumulation. Finally, we develop a minimal model identifying the main ingredients required to get efficient rectification of active particles in ratchet-like structures. Altogether, our work builds up the principles of designing microstructures that self-phoretic active particles interact with and provides key insights into achieving a macroscopic flow of active particles by exploiting these interactions.

3.2 Results

Our experiments are performed with catalytically active Janus particles composed of silica colloids (2.5 μm radius) half coated with a thin layer of Pt (~10 nm) (see Methods). When suspended in an aqueous solution of H_2O_2, these particles exhibit self-phoretic active motion. The Pt cap catalyses the degradation of H_2O_2, setting up an asymmetric chemical field around the colloidal particle. The concentration gradient of products along the surface of the particle induces a phoretic slip velocity, resulting in the propulsion of the particle away from the Pt surface (Figure 41A, B).[86] The particle motion is ballistic on small timescales ($t < \tau_r$) and becomes diffusive over the larger time scales.[104]

The swimming of the active particles is largely confined to a plane close to the bottom surface, displaying an orientation vector aligned parallel to the surface

which confines their trajectories to a 2D plane (Figure 41C, D). We have previously reported on the hydrodynamic and phoretic effects that lead to the stable steady state at θ ~ 90° and results in the surface entrapment effect in spherical active particles.[178] Importantly for us, this means that particles can interact *via* chemical and hydrodynamic fields with topographical features of the surface.[179]

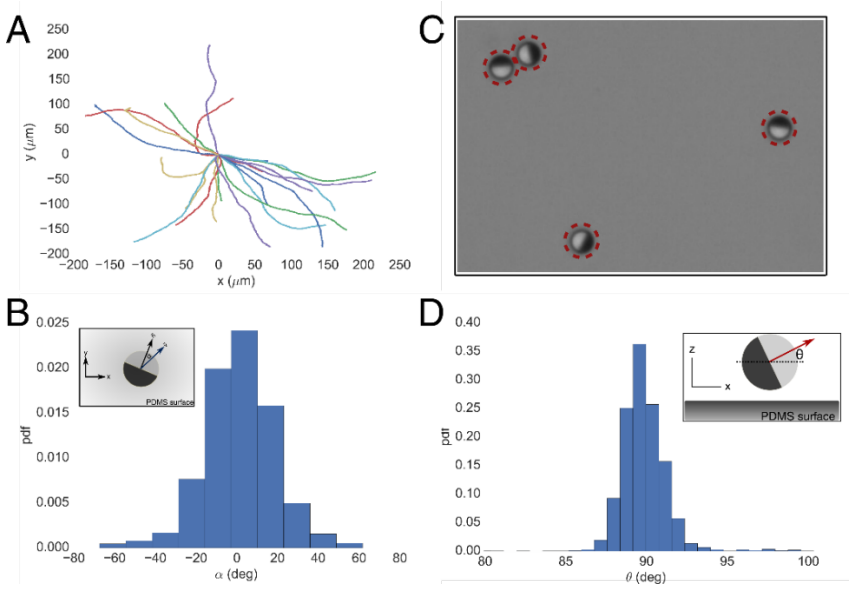

Figure 41: Self-propelled Janus particles on surfaces with topographical features. (**A**) Sample trajectories of r = 2.5 μm spherical active particles near a homogenous flat surface with v_0 = 6 μm/s for t < 30 sec. (**B**) Probability distribution of the angular difference(α) between the velocity vector (**v**) and the orientation vector (**n**) of a micromotor. (**C**) A snapshot of spherical micromotors swimming near the surface. The black half is the Pt coated side and the white half the uncoated SiO_2 side. (**D**) Probability distribution of θ (defined in inset) of micromotors swimming near the surface.

We create these topographical features using a DWL method and replicate the designs onto a PDMS surface where the structures appear as 'wells'. We

begin our experiments by allowing a dilute suspension of colloidal particles to sediment onto the PDMS surface. Initially, in the absence of activity, we see that the particles are uniformly distributed on the surface with a cap down orientation induced by the bottom heaviness of the Pt coated particles (Figure 42C). We then add H_2O_2 into the system to introduce activity. The particle orientation changes to $\theta \sim 90°$ and they begin to self-propel along the PDMS surface. Within the first minute, we observe that most active particles are confined to the topographical structures which act as potential wells, as particle density on the surface outside the ratchet structures depletes (Figure 42A, B and D).

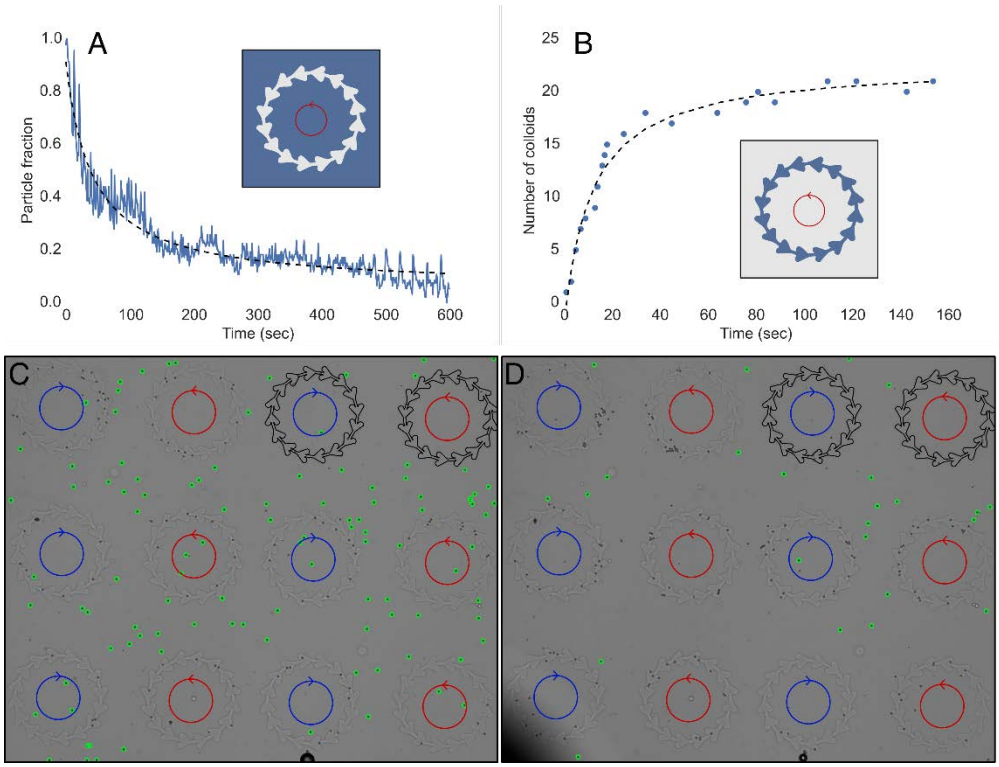

Figure 42: Dynamic of self-propelled Janus particles on surfaces with potential wells. (A) Depletion of the fraction of Janus particles outside the asymmetric structures on the surface (blue region in inset). (B) Cumulative number of active particles observed inside the asymmetric ratchet-like structures over time (blue region in inset). (C- D) Snapshots showing the particle distribution on the surface at t = 0 and t = 60 sec respectively. The green circles mark the particles outside the asymmetric structures.

3.2.1 Active particles in symmetric structures

As a control, we start by tracking the trajectories of active particles in a channel of repetitive symmetric units and do not observe any directional flow of particles. Over an extended period of time, we notice an equal probability of particle flow in both the clockwise and anti-clockwise directions, as expected (Figure 43A, B). Plotting the stationary probability distribution of particle positions in these structures we notice that the particles position clearly tends to accumulate at the boundaries (Figure 43C). Since we work at very dilute particle concentrations, the influence of particle-particle interactions is negligible on the overall characteristics of particle flow which is dominated by particle wall-interactions.

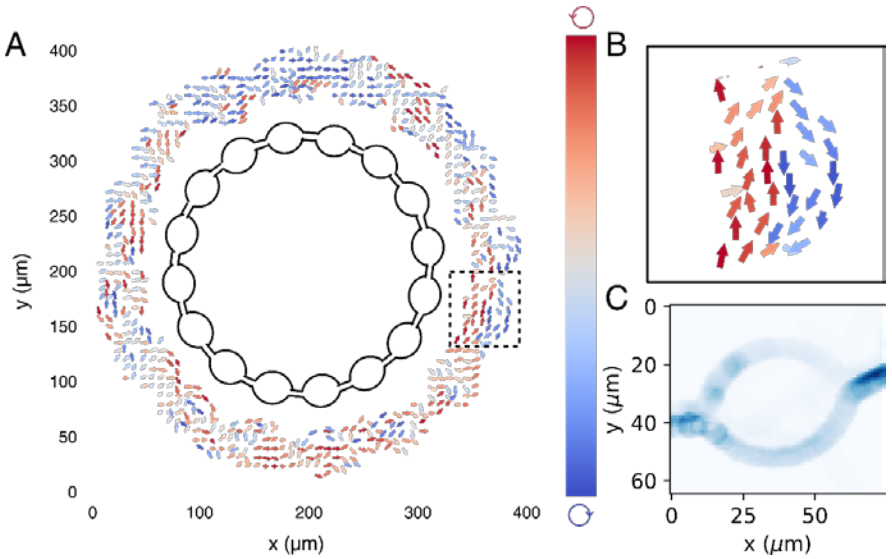

Figure 43: Self-propelled Janus particles in symmetric channels. (**A**) Velocity maps obtained from tracking active particles inside symmetric channels. Color bar on the right corresponds to the vorticity direction. (**B**) Zoomed image of the highlighted region (black dotted square) in A. (**C**) Particle distributions averaged over a steady state inside a unit structure of the channel.

3.2.2 Active particles in triangular channels

Now, in order to obtain directional flow of particles, we introduce asymmetry by using triangular units. In simulations of self-propelled Janus particles within these units, modelled with frictionless collision dynamics at the walls, a net flow is observed. Within an experimental system of self-propelled Janus particles, however, ϕ does not evolve according to frictionless collision dynamics but rather is strongly influenced by the hydrodynamic and phoretic effects. The particles do not simply slide along the walls until they are reoriented back into the channel but are actively aligned by the walls in a very short period which leads to a very different effect. We observe that using

asymmetric triangular channels does not lead to rectification in our experiments over extended periods of time. The particles simply accumulate at the sharp corners of the triangles and stay there for times significantly greater than the rotational diffusion time τ_R (Figure 44A, B, C).

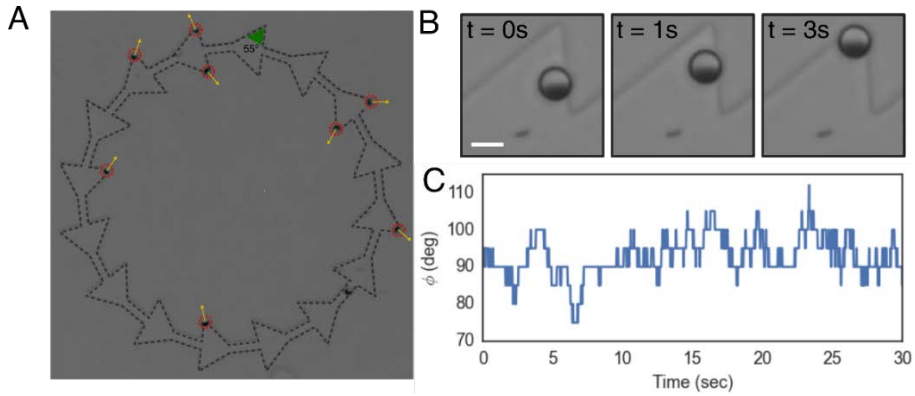

Figure 44: Self-propelled Janus particles in triangular channels. (A) Snapshot of an experiment with self - propelled Janus particles in an asymmetric channel with triangular structures. (B) Time lapse images of a self-propelled particle approaching and getting captured at the sharp corner of a triangular structure. (C) Tracked angular evolution of the particle orientation at the sharp corner of the triangular structure.

This can be explained by accounting for the influence of the two confining walls at the sharp corners of the triangular structures. Once the particle approaches the sharp corner, every time thermal fluctuations try to reorient the particle away for the corner, the particle encounters one of the two confining walls and stays aligned with it leading to a meta-stable state at the sharp corners. Indeed, this is only possible because the self-propelled Janus particles behave as active Brownian particles where the orientation of the particles diffuses slowly over a period of time as opposed to run and tumble particle where the tumbling event leads to a sharp change in orientation. These

asymmetric triangular structures can in fact be used for the rectification of run-and-tumble particles, such as motile bacteria, which can escape away from the corners via tumbling events even if an active alignment mechanism exists.

Based on the above experiments, we designed asymmetric channels with 'smooth' corners to avoid the accumulation of particles at these corners. We notice right away that we begin to obtain particle flows in the desired direction (Figure 45 A). However, on closer observation, we find a considerable number of particle trajectories (≈15%) in the opposite direction of the easy axis of the ratchet structure. In order to understand this phenomenon, we track the individual trajectories of particle moving against the 'easy axis' of the structure and plot the probability distribution of the release angle (δ), defined as the angle between the tangent of the ratchet unit at the cusp and the velocity vector obtained from tracking the particle for ~25 µm. (Figure 45C).

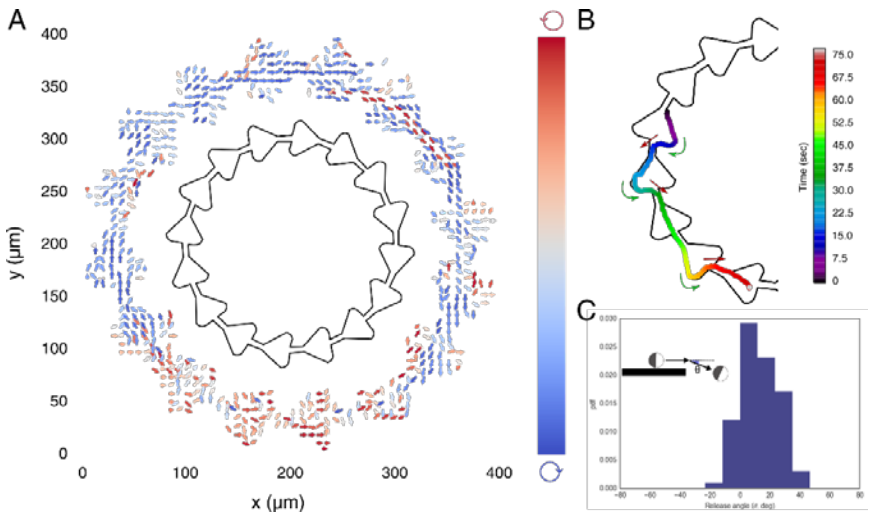

Figure 45: Self-propelled Janus particles in triangular channels with rounded corners. (A) Velocity maps obtained from tracking active particles inside asymmetric triangular channels with curved edges. Colour bar on the right corresponds to the vorticity direction. (B) Example trajectory of a particle swimming against the easy axis of the structure. Colour bar is the progression of time. (C) Probability distribution of the release angle (δ, defined in Inset)

Interestingly, we find a bias in δ towards positive values (in the direction of the wall), where δ peaks between 10 and 20 degrees. This bias is most likely due to the asymmetry of particle-wall interactions along the surface of the particle at the tip, that introduces a small torque towards the direction of the wall. This leads to trajectories such as the one represented in Figure 45B where, once the particle is directed against the direction of easy axis (either due to particle-particle collisions or random reorientations at the centre of the channel), it tends to move in that direction until it's directed back due to chance particle-particle collisions.

3.2.3 Directed flow of active particles in asymmetric channels

Our final designs account for all the observed effects above to include smooth corners to avoid accumulation of particles and edges that incline back into the centre of the channel at an angle greater than $2\bar{\delta}$ to avoid the back flow of particles (Figure 46A, B). The ratchet units are designed to allow for the easy movement of particles in either the clockwise or counter clockwise direction. Note that even though the height of the ratchet structures is ~1 μm, as compared to the 5 μm diameter of the active particles, it is sufficient to influence the trajectories of the particles close to a confining surface.[178]

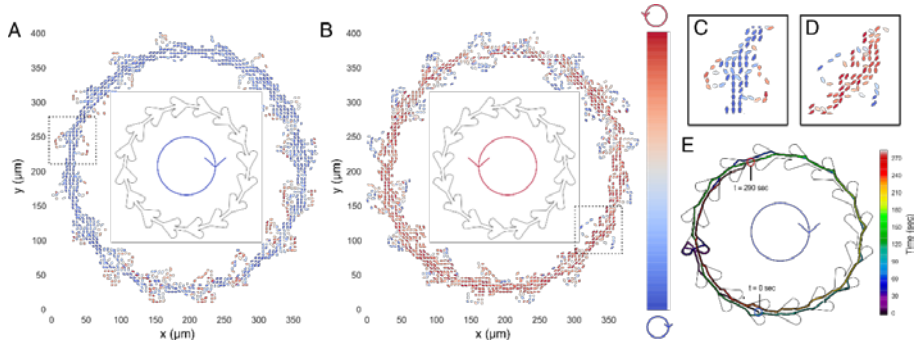

Figure 46: Circular flow of active particles inside periodic ratchet-like structures. (**A-B**) Velocity maps obtained from tracking active particles (n=100; N=6) inside the asymmetric structures meant to generate flows in the clockwise and anti-clockwise directions. Colour bar on the right corresponds to the vorticity direction. (**C-D**) Close-up of the individual cells marked by dotted squares in A, B. (**E**) Sample trajectory of an active particle over t = 290 sec inside the asymmetric structure. Colour bar on the right corresponds to time progression.

Figure 46A, B show the velocity map of the active particles within these structures for over 300 secs, highlighting the directional bias of particles in the clockwise and anti-clockwise directions. The length of the arrows corresponds to the velocity of the particles, which at the H_2O_2 concentration that we use is ≈6µm/s, and the colour corresponds to the vorticity direction. Figure 46C, D show magnified images of one of the ratchet units. We see that, while the velocity field in the centre of the structure is biased toward the direction set by the ratchet, the rounded edges display a flow in the opposite direction where the particles´ flow is reversed into the ratchet direction (Figure 46E). This current is also sensitive to the chemical and material properties of the ratchet structure and we discuss these effects in Appendix A.

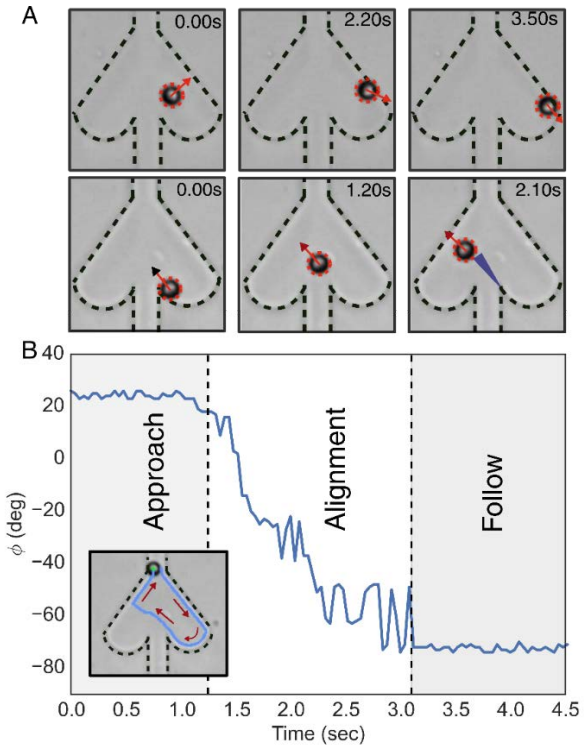

Figure 47: Alignment and release of active particles influenced by topographical features. (**A**) Snapshots of an active particle interacting with a topographical feature and releasing from the edge of a topographical feature. (**B**) Evolution of the in-plane angle, ϕ over time. Inset is the full trajectory of a particle that releases from the edge and is realigned at the opposite side.

In the following section we will describe the dynamics of an individual active particle within the asymmetric channel. For an active particle starting from the centre of the cell, we observe that the particle approaches the side of the structure and reorients parallel to the structure within a short period of time (see Figure 47A top and Figure 47B). The orientation of the particles in proximity of the structure is pinned by the tangential orientation of the topographical structure. If the reorientation occurs towards the 'easy' axis, the particle follows along towards the next ratchet unit. If the reorientation

occurs towards the 'hard' axis, the particle remains aligned along the structure until it reaches the sharp tip (cusp) at the end of the rounded edge, where it releases back into the centre of the structure (see Figure 47A bottom) with a small bias in the release angle towards the walls as described in Figure 45C. The typical persistence length of these particles ($l_p = v_p\tau_r \approx 300$ µm, where v_p is the propulsion velocity) is an order of magnitude larger than the distance from the tip to the opposite wall of the unit structure (16 µm) and most of the particles reach the wall at an orientation close to the release angle. This allows us to determine the angle at which the particles approach the opposite wall by controlling the geometry of our structure. Within our design, from observations of over 400 particles, we see that the probability to re-orient in the easy axis upon reaching the wall is significantly higher than to re-orient in the hard axis ($P_{easy} = 0.77$) resulting in a strong bias in the overall directionality of the current.

Altogether, these results show that the angular alignment of active particles by topographical features can be used to generate a macroscopic flow of particles in properly designed asymmetric ratchet structures.

3.2.4 Accumulation of active particles using linear ratchet structures

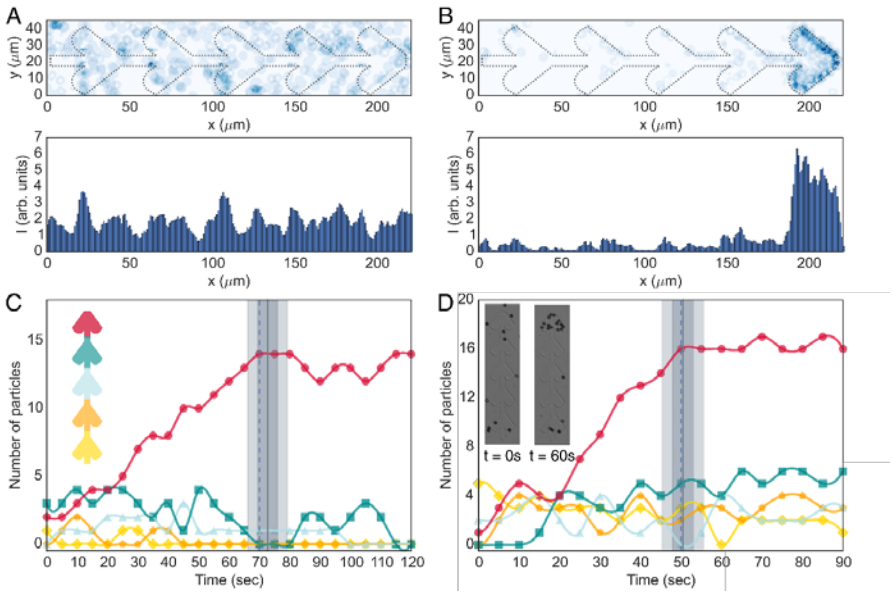

Figure 48: Accumulation of active particles using linear ratchet structures. (**A- B**) Average positions ofactive particles at t = 0 and t = 60 sec respectively obtained from 17 different experiments.(**C- D**) Evolution of the number of particles in each of the units of the structure over time at v_p = 4 μm/s and v_p =6 μm/s respectively. The solid grey line represents the average saturation time from 15 different structures and the shaded grey areas are up to one and two standard deviations. Inset of D) contains snapshots of the structure at t = 0 and t= 60 sec respectively.

We next use a linear ratchet structure containing 5 units to determine whether active particles can be accumulated in confined spaces (Figure 48). At t = 0 sec we find the particles to be uniformly distributed (Figure 48A). Upon addition of H_2O_2, the particles begin to self-propel and within 60 seconds, we find a clear accumulation of particles in the last ratchet unit (Figure 48B). For a system of active particles with v_p = 4 μm/s, we track the number of particles in each

cell from t = 0 to t = 120 sec which shows the increase in the number of particles in the final unit until t = 75 sec after which it saturates (Figure 48C). As expected, the saturation time is reduced, to t = 60 sec, for particles with v_p = 6 µm/s which can be achieved by increasing the concentration of H_2O_2 in the system (Figure 48D).

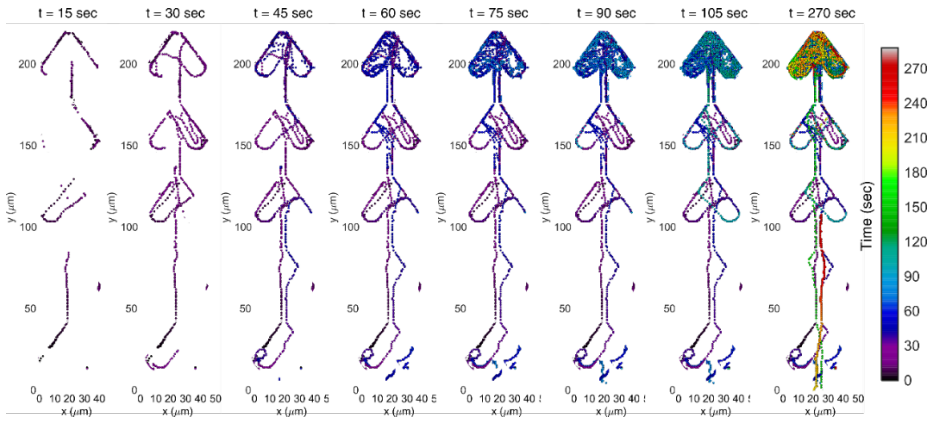

Figure 49: Trajectories of active particles accumulated over different time lengths from t = 15 sec to t = 270 sec. Colour bar on the right corresponds to time progression.

In Figure 49 we represent the trajectories of all the particles over 270 seconds. After t = 60 sec, we see that the particle motion is largely confined to the final ratchet unit with little exchange with the rest of the structure (see Figure 50A). To shed light into the mechanism of particle accumulation, we acquire high magnification time-lapse images of particles moving in the final unit after the saturation time.

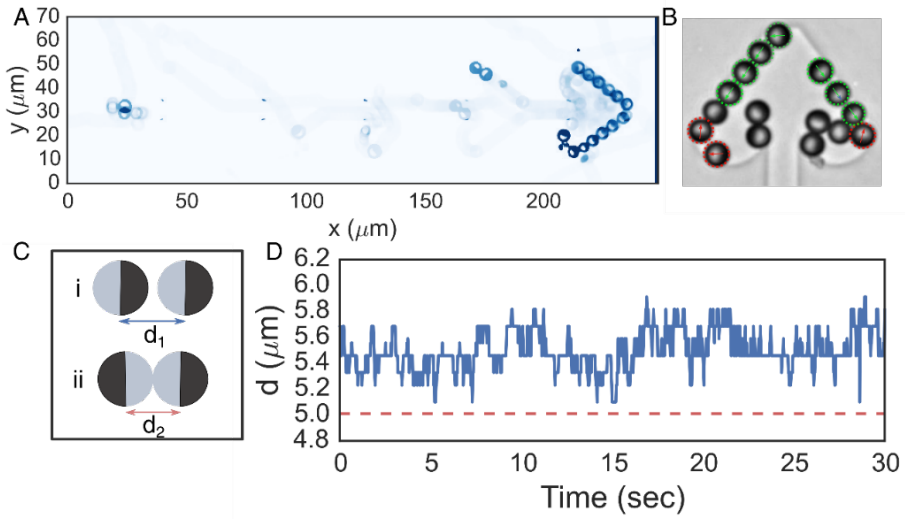

Figure 50: Orientational locking of active particles in confined spaces. (**A**) Particle distribution averaged over a steady state in the asymmetric structures after saturation. (**B**) Snapshot showing the positions and orientations of active particles confined in the final cell of the ratchet structure. (**C**) Definitions of the separation distance between the particles in two different configurations. (**D**) Separation distance between two active particle s in cap - inert (blue) and inert - inert (red dotted) configurations.

We find that particle accumulation is due to the orientational-locking of Janus particles in confined spaces arising from a combination of particle-particle and particle-wall interactions. When two active particles moving in opposite direction along the side of the ratchet unit interact (i.e., inert sides touching), they are locked into their positions as both the particles typically have a similar propulsion velocity and both their orientations are strongly aligned with that of the side wall (Figure 50B). This results in further jamming of newly interacting particles, locking their location and orientation, leading to a state where the positions along the wall are highly occupied (Figure 50B). We find that this state is not resolved by the imbalance in the number of particles on

either side. The chemical products generated from the catalytic cap of one of the particles introduces a repulsive force that prevents physical contact between the inert side and the catalytic side of neighbouring particles. This leads to the particle behind the catalytic cap simply fluctuating in position without making physical contact with the particle in front. The separation distance between the particles over time clearly shows these fluctuations of around 0.6 µm (Figure 50C, D). There is however dynamic exchange between the particles along the wall and particles in the bulk but the positions along the wall are constantly occupied leading to the confinement of active particles within the final cell of the ratchet. A similar effect can also lead to jamming between the ratchets units in the channel at high particle concentrations (Appendix B).

These results show that a system composed of asymmetric ratchet units can be used to concentrate active particles in confined areas. And since the saturation time of the particles depends on the velocity of the particles, this system can further be exploited to separate particles based on their propulsion velocity.

3.3 Minimal model and discussion

The minimal model was developed by Dr. Raphael Voituriez

We have demonstrated how a combination of breaking the time-reversal symmetry through the alignment interaction of active particles at

topographical features, and the breaking of spatial symmetry by using asymmetric ratchet structures can lead to a robust method of controlling the motion of active particles. In the following, we provide a minimal model that captures the observed effect and shows that active particle trajectories can be rectified geometrically by properly shaping the walls of a quasi 1D channel. We determine the flux of particles and its dependence on the main parameters of the problem. The aim of the minimal model is to determine on general grounds the key ingredients involved in the process, but not necessarily to quantitatively fit the data obtained in a specific set-up.

Following the experimental set-up described in the paper, we assume that the active particles are confined in a quasi 1D channel. We neglect particle-particle interactions and assume that the particles have planar anchoring interactions with the confining walls, as observed experimentally. Importantly, this interaction breaks time reversal symmetry and will be essential to generate a macroscopic flow of particles.

We assume that the active particles follow run and tumble dynamics, that we project along the main axis x of the channel; the problem is therefore effectively 1D and we denote by $\rho_{\pm}(x)$ the total density of + (resp. -) moving particles, i.e. either moving towards (+) or opposite (-) to the ratchet easy axis. The density $\rho_{\pm}(x)$ encompasses both free moving and wall-associated particles. The interaction with the channel walls is modelled by an effective association constant K so that the density of wall-associated particles is given

by $\rho_{\pm}^{w}(x) = K\rho_{\pm}(x)$. A model of active Brownian particles, more realistic to model Janus particles but less suitable to an analytic resolution of the model, would yield qualitatively similar results. We assume that the ratchet channel is periodic with period L; following the experimental set-up, it is characterized by sharp cusps at positions $x = nL$ with $n \in \mathbb{Z}$, with a singular local tangent forming an angle β_0 with the x axis. We will assume that except for these cusps the shape of walls is smooth. At steady state, the density of free particles follows:

$$v\partial_x\rho_+ = -\lambda(\rho_+ - \rho_-); -v\partial_x\rho_- = \lambda(\rho_+ - \rho_-) \quad (43)$$

Here λ is the tumbling rate, and we introduce the Peclet number $P = v/(\lambda L)$ defined here as the ratio of the persistence length over the system period. For the sake of simplicity, we model the interaction with domain walls only effectively: + movers are assumed to be unaffected by interactions with the walls, and - movers are assumed to be affected only in the neighbourhood of a cusp. In a first approximation λ is assumed unchanged for both free and wall interacting particles; relaxing this hypothesis would not change qualitatively the results. We therefore write the following boundary conditions at each cusp $x = nL$:

$$\rho_+(x^+) = \rho_+(x^-) + \alpha\rho_-(x^+); \rho_-(x^-) = (1-\alpha)\rho_-(x^+) \quad (44)$$

Here α is a phenomenological parameter that encompasses the local geometry of the cusp and quantifies the fraction of - movers that are converted into + movers by the cusp. Importantly, this effect is made possible only because of

the aligning interaction with the walls and self-propulsion and can be seen as a local Maxwell daemon sitting at each cusp. The parameter α depends on the specific geometry of the channel (cusp angle β_0), and on the fraction of wall associated particles. We therefore expect the following scaling $\alpha \propto K \cos\beta_0$.

Introducing $\rho = \rho_+ + \rho_-$ and $m = \rho_+ - \rho_-$, it is easily seen that equations (43, 44) are solved for

$$\rho = \rho_0 + \frac{m}{P}\left(1 - \frac{2x}{L}\right) \quad m = \frac{\alpha P \rho_0}{2 - \alpha + \alpha P}$$

where ρ_0 is the mean density of the free active particles. The total flux of particles is then given by $\Phi = vm$.

This result highlights the main ingredients required to get efficient rectification, and the dependence on the key parameters. First, as expected, the Brownian (equilibrium) limit $P \longrightarrow 0$ yields a vanishing current, which shows that self-propulsion is essential. The flux is monotonically increasing with P and saturates to full rectification for $P \longrightarrow \infty$. Note that P can be tuned either by the properties of self-propulsion or the geometric parameter L. Second, the coupling to a geometric cue with broken symmetry (the cusp) is also essential, since α is dependent on the geometry of the channel through the cusp angle β_0 and the strength of the alignment interaction quantified by K.

3.4 Concluding Remarks

We have demonstrated that the alignment interaction of spherical active particles with topographical features can be exploited by using asymmetrical patterns, to obtain a directed flow of active particles. Active particles deposited on ratchet-like structures display directional trajectories and macroscopic particle flows. We have also shown that the same effect can be used to concentrate active particles in confined spaces. Further, we have identified the combination of particle-particle and particle-wall interactions that stabilizes this confinement effect. Finally, through a minimal theoretical model, we have identified the key parameters responsible for the experimentally observed rectification effect.

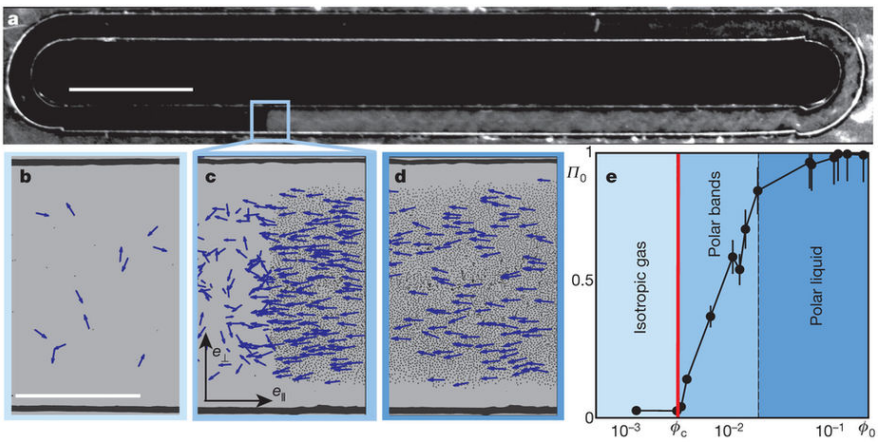

Figure 51: Directed flow of colloidal rollers in racetrack structures. (A) A macroscopic band of colloidal rollers emerges in a racetrack microfluidic channel.(B) Random motion of particles at low concentrations.(C- D) Emergence of polar order at high concentrations of active particles. (E) Average polarization plotted versus area fraction.[40]

Since our system relies on particle-wall interactions, the rectification can occur at low concentrations of particles. In fact, we have observed that a high concentration of particles, the system is prone to jamming effects at the narrow channels (Appendix B). In such situations, a promising approach to achieve directed transport of active particles is to exploit particle-particle interactions. If the particles have a tendency to align with their closest neighbours, above a critical concentration of particles, flocking can occur as an emergent property. Bricard *et al.* have demonstrated this phenomenon in colloidal particle.[40] In a system of colloidal rollers which interact with each other through electrostatic and hydrodynamic interactions, they showed that beyond a critical concentration, a polar state emerges, and a directional flow of the active particles is observed in a race track like channel.

Together, these two approaches represent the different ways of obtaining a directional flow of active particles either via, particle-wall or particle-particle interactions. This ability to control the behaviour of normally diffusive active matter systems at both low and high concentrations of particles opens new possibilities in microfluidic systems, lab-on-a-chip applications and eventually to extract useful work from these out-of-equilibrium systems.

3.5 Appendix A: Dependence of particle flow on material and chemical properties of the surface

The chemistry of the surface can affect both the propulsion velocity and the orientation dynamics of the particle. As a first step towards modifying surface chemistry, we treated the PDMS surface with O_2 plasma. This surface treatment is known to induce negative charges on the PDMS surface and reduce its hydrophobicity. Upon analysing the resulting videos, we find that the general rectification effect is not affected. However, on tracking individual trajectories, we find a ≈20% increase in their propulsion velocity after the plasma treatment of the surface. This could be due to the higher separation distance of the particles from a negatively charged surface (electrostatic repulsion) resulting in a reduction of drag at the surface. An opposite effect can be achieved by functionalizing the surface with amine groups, which induced a positive charge on the surface and the negatively charged colloidal particles get 'stuck' or have significantly lower velocities reducing the efficiency of rectification.

Another approach to modify the chemistry of the surface is to coat it with a thin layer of a different material to see if the rectification behaviour has a dependence on material choice. In order to address this question, we coated our structures with a thin layer of Ti to ensure that the metal layer does not have a catalytic effect with H_2O_2 under visible light. We notice initially that the particles are self-propelled with a $v_p \approx 6$ μm/s as observed on an uncoated

surface. However, over time, we notice that the particles stop self-propulsion at certain points in the ratchet structure marked in green red and yellow

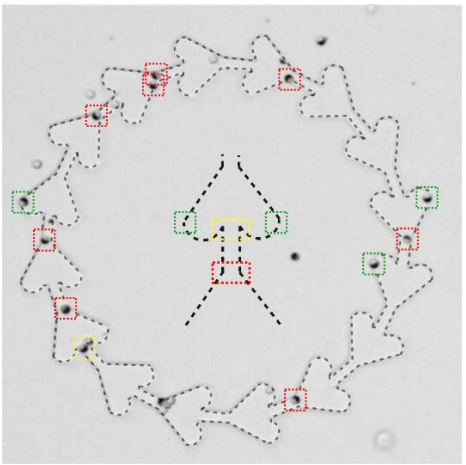

Figure 52: Snapshot of an experiment with self-propelled Janus particles in a ratchet structure coated with a layer of Ti. The red, green and yellow boxes represent the regions in the geometry where the particles must reorient to realign with the subsequent part of the ratchet structure.

We observe that these are the parts of the ratchet geometry where the particles must reorient to realign with the ratchet structure. During the reorientation, the metal cap comes in contact with the metal surface on the ratchet structure which introduces van-der-Waals attraction, restricting the particle motion. However, the same effect does not come into play with the bottom surface which is also coated with Ti. In order to understand this, we need to consider the effect of phoretic slip at the bottom surface.

For a self-phoretic particle close to a confining boundary, the chemical product generated at the catalytic cap is accumulated between the particle and the surface. This asymmetric distribution of chemical product close to the bottom

surface leads to a surface slip above which the particle slides.[180] The side steps in the ratchet structure however are not confining for the chemical product and the particle can come in physical contact with edges where the particles get pinned.

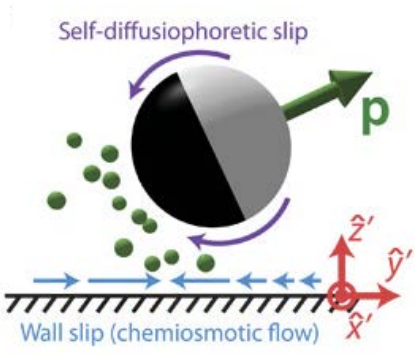

Figure 53: Schematic illustrating the self-diffusiophoretic and chemiosmotic mechanisms that drive the motion of a chemical active particle. The self-generated solute gradient (green spheres) drives flows localized to thin boundary layers on the particle surface (magenta arrows) and on the nearby wall (blue arrows).

3.6 Appendix B: Effect of opening width of channels and jamming

This problem of the effect of the opening width of the ratchet channels can be reduced to that of escape kinetics of self-propelled Janus particles from a cavity and has, in fact, been dealt with theoretically.[181] The simulations suggest that the escape rate from a cavity can be maximized by adjusting the self-propulsion strength in such a way that the mean free path of the Janus particles (l_p) matches with the cavity size and by using smoothly corrugated channels

that avoid sharp corners. Within our final design we fulfil both these parameters such that the cavity dimensions are all < l_p of the self-propelled particles and the edges are smooth. However, the width of the opening of the channel does dictate the particle concentration that can be rectified. At lower particle concentrations, an opening width of ≈ 1.25*$R_{particle}$ is sufficient to obtain efficient rectification. However, when we use a higher number of particles in the same system we notice that it leads to jamming due to the orientational locking of particles at the narrow openings (Fig 2).

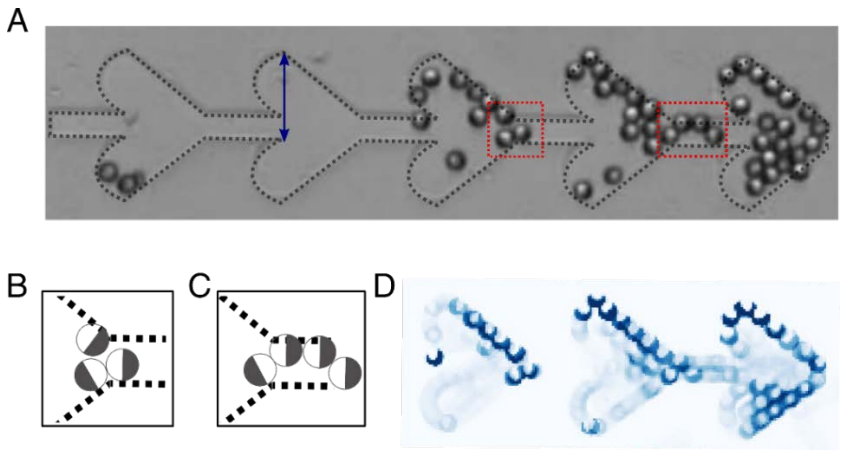

Figure 54: Jamming of self-propelled particles at channel openings. (A) Snapshot of an experiment with high concentration of Janus particles in an asymmetric channel. (B-C) Schematic representing the jamming of channel openings due to orientational locking of Janus particles(D) Average distribution of particles in jammed channels represented in A.

This situation can be remedied by using wider openings of the channels (this was verified by using particles of lower radii in the same channels). The limit on the width of the channel opening is set by the longest distance that the particle must navigate within the channel away from the walls (blue line); this is the distance from the edge of the channel to the opposite wall. If this

distance is smaller than the $0.1l_p$ of the particle, when the particle motion is purely ballistic, we do not expect the rectification to be significantly affected. Considering these arguments and retaining the curvature of the inclining boundaries at the side, the channel width can be increased over 5 times to obtain flows with larger concentrations of particles.

4.Cross-stream migration of active particles in external flow

4.1 Introduction

In microorganisms, such as bacteria, self-propulsion helps them in the efficient exploration of their surroundings to find nutrient-rich areas or to swim away from toxic environments. A common feature among natural micro-swimmers is an ability to adjust their self-propulsion in response to local stimuli such as chemical gradients, temperature gradients, shear flows, or gravitational fields. Whereas the mechanism of some of these responses, such as chemotaxis, is active, involving the ability to sense gradients and signals, that of others is passive, purely resulting from external forces and torques.

Recently, there has been substantial effort to develop artificial micro-swimmers, which mimic this ability to respond to external stimuli.[182] The possibility of creating artificial micro-swimmers that have a predictable response to an external signal, like those observed in natural micro-organisms, could be helpful in achieving several of the complex applications envisioned for these systems. In general, however, it is difficult to create synthetic analogues for responses that have a physiological origin, such as chemotaxis (Figure 55A).[183]

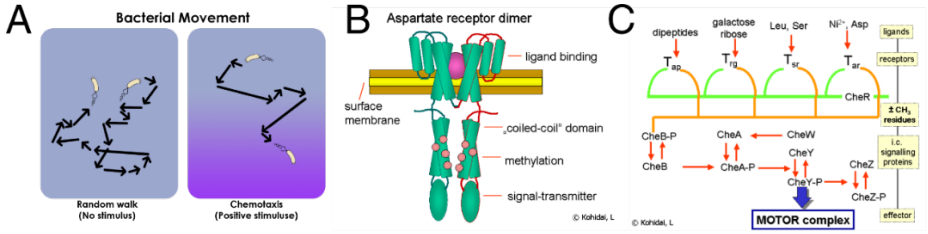

Figure 55: Bacterial chemotaxis. (**A**) In a uniform field the swimming behaviour of bacteria resembles a random walk. However, in the presence of a gradient of chemo-attractant (purple) bacteria perform biased random walk to enable a net drift towards the higher concentrations of the chemo-attractant[184]. A complex physiological feedback mechanism composing of multiple trans membrane receptors (**B**) and signalling pathways[185] (**C**) regulates the flagellar bundling and unbundling rates biasing the bacterial swimming behavior[186].

In bacterial chemotaxis, chemical gradients are sensed through transmembrane receptors, called methyl-accepting chemotaxis proteins (Figure 55B), which vary in the molecules that they detect. These receptors bind attractants or repellents at the membrane and generate a signal that is transmitted across the plasma membrane into the cytosol, where *Che* proteins are activated. The *Che* proteins alter the tumbling frequency of the bacteria in response to the concentration of attractors or repellents at the membrane (Figure 55C).[187] In a uniform chemical environment, the bacteria have a set tumbling rate and the overall swimming behaviour resembles that of a random-walk.[188] However, in the presence of a gradient of chemo-attractant, the tumbling rate is modified to enable longer runs in the direction of the chemical gradient, biasing the random-walk and enabling the bacteria to accumulate in regions of higher concentration.[189]

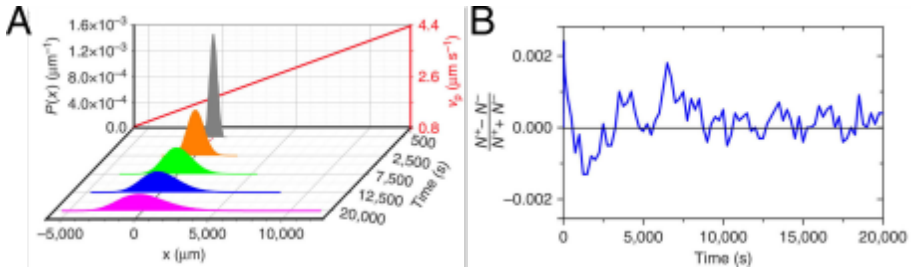

Figure 56: System with position dependent variation of propulsion velocity. (A) Time evolution of the probability distribution P(x) of self-propelled particles with variable self-propulsion as obtained from Brownian dynamics simulations. Although P(x) becomes asymmetric at long times, no systematic drift of the particles to regions of higher motility is observed. (B) Time evolution of $(N^{+}-N^{-})/(N^{+}+N^{-})$, where N^{+} and N^{-} are the numbers of particles at $x>0$ and $x<0$, respectively[190].

This complex sensory feedback mechanism is difficult to implement in simple synthetic micro-swimmers. Here, the particles respond to chemical concentrations only through their velocity, and their reorientation time is completely determined by the physical parameters of the system, the particle radius R, solvent viscosity η and thermal energy k_BT ($\tau_{rot} = 8\pi\eta R^3/k_BT$). It can be shown with Brownian dynamics simulations that in such a system with only position dependent variation of propulsion velocity, but not reorientation rate, no net drift is possible (Figure 56).[190]

There do however exist a set of responses in natural micro-swimmers which are thought to arise solely due to the physical response of the swimmer body to external stimuli and are not dependent on complex sensory feedback mechanisms. An example of this is gravitaxis (ability to swim preferentially upward despite the sedimenting effects of gravity) in *Paramecium*, which is caused by the fore-aft body asymmetry (Figure 57A).[191] Axially symmetric bodies with fore aft asymmetry rotate as they sediment downwards under gravity until the narrower end lies uppermost, after which they fall vertically downward with no further change in orientation. If a micro swimmer with such a shape swims towards its narrow end, it can result in a preferential movement

against the direction of gravity as observed for *Paramecium*. A different mechanism is responsible for gravitaxis in smaller flagellates such as *Chlamydomonas*. Here the directional response is caused not due to asymmetry in body shape but due to the longitudinal density gradient within the cell. The resulting bottom heaviness leads to an alignment mechanism similar to that of a buoy in an ocean and the particles are able to swim against gravity.[192]

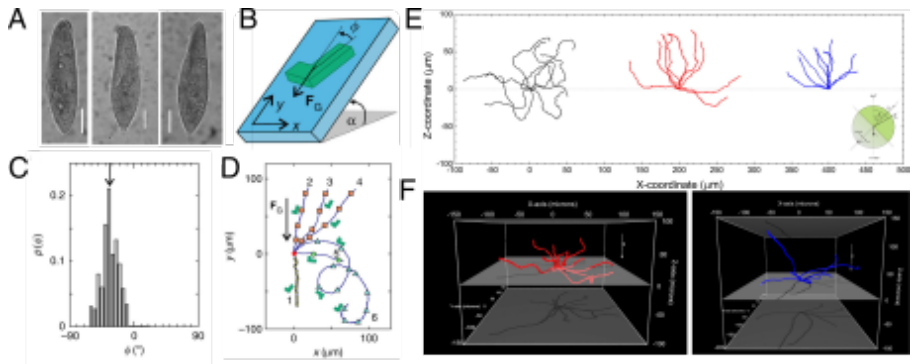

Figure 57: Gravitaxis in natural and artificial micro-swimmers. (**A**) Fore-aft body asymmetry in Paramecium leads to their ability to perform gravitaxis. Predicted orientation rate increase (3.7±0.2 deg s^{-1}, 8.8±0.7 deg s^{-1} and 15.3±1.1 deg s^{-1} from left to right) with degree of asymmetry[191]. (**B**) Sketch of an L shaped particle sedimentingta an inclination angle α=10.67° [193]. (**C**) Measured probability distribution p(φ) of the orientation φ of a passive L-shaped particle during sedimentation for the case depicted in B[193]. (**D**) Experimental trajectories for the same inclination angle and increasing illumination intensity: (1) I=0, (2–5) 0.6 μW $μm^{-2}$<I<4.8 μW $μm^{-2}$, (6) I>4.8 μW $μm^{-2}$ (which corresponds to increasing self-propulsion). All trajectories start at the origin of the graph (red bullet). The particle positions after 1 min each are marked by yellow diamonds (passive straight downward trajectory), orange squares (straight upward trajectories), green bullets (active tilted straight downward trajectory) and blue triangles (trochoid-like trajectory)[193]. (**E**) 2D Swimming trajectories for representative Janus spheres observed in the (x,z) plane for radius a = 0.95 μm (black), a = 1.55 μm (red), and a = 2.4 μm (blue) spheres. The swimmers are suspended in a 10 wt %solution of H_2O_2. Gravity is acting downward in the z direction[194]. (**F**) 3D Swimming trajectories for representative Janus spheres; a = 1.55 μm (left) and a = 2.4 μm (right)[194].

Both these physical mechanisms arising from body shape asymmetry and bottom heaviness have been exploited to create artificial micro-swimmers that preferentially swim upwards. ten Hagen *et al.* demonstrated by using an L shaped particle that simple shape asymmetry is sufficient to induce gravitaxis in micro-swimmers.[193] They could show that passive L shaped particles, when sedimenting under gravity, adapt a preferential orientation as shown in Figure 57B, C. When self-propulsion is high enough for these particles, they observed that the particles displayed a rectilinear motion in the upward direction against gravity (Figure 57D). On the other hand, Campbell *et al.* have shown that bottom heavy spherical Janus particles which swim away from their heavier catalytic caps, also exhibit gravitaxis due to the preferential orientation induced by their mass asymmetry (Figure 57E, F).[194]

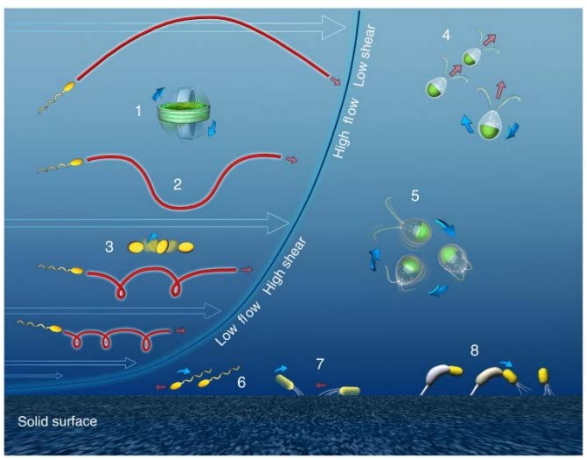

Figure 58: Microorganisms in flow. Fluid flow can have a broad range of effects on microorganisms, both in the bulk fluid and in the vicinity of surfaces. White arrows and the blue line define the velocity profile of the flow. The flow velocity is zero at the solid surface (no-slip boundary condition), where shear is highest. Numbers refer to different flow–microbe interactions, as follows. (1) Periodic rotations ('Jeffery orbits') of

non-motile phytoplankton cells, such as diatoms. (2) Trajectories of motile bacteria for different magnitudes of shear. (3) Jeffery orbits of a non-motile bacterium. (4) Gyrotaxis of phytoplankton. (5) Gyrotactic trapping of phytoplankton. (6) Upstream swimming of bacteria. (7) Upstream twitching of bacteria. (8) Surface colonization by a stalked, curved bacterium under flow.[195]

Similar to the interplay of gravity and self-propulsion, the interplay of flow and swimming activity has been shown to lead to robust directional response of natural micro-swimmers through a rich variety of mechanisms (Figure 58).[195–201] In 1985 Kessler showed that bottom-heavy microorganisms, such as algae, when exposed to a flow in a channel, accumulate at the centre of the channel (Figure 59B).[192] The swimming direction of these cells is set by a balance of gravitational torque due to the asymmetry in body density and the viscous torque imposed by the hydrodynamic shear, and the cells are said to be 'gyrotactic' (Figure 59A)[202–204]. When a spherical cell of radius *a* and mean density ρ, with an offset, L, between its centre of mass and its centre of buoyancy due to the asymmetric density distribution is exposed to shear S, the cell swims upward in the direction $\sin\theta = BS$, where $B = 3\mu/\rho Lg$ is the gyrotactic reorientation time scale, μ the dynamic fluid viscosity, and g the acceleration of gravity. Decades later, Durham *et al.* used the understanding to this mechanism to explain the formation of phytoplankton thin layers in oceans. In a mechanism termed 'gryrotactic trapping' they showed that when $|S| > S_{CR} = B^{-1}$, the stabilizing gravitational torque is no longer able to counter act the hydrodynamic torque that causes them to spin, and the cells tumble end over end accumulating in these regions of high shear (Figure 59C).[205]

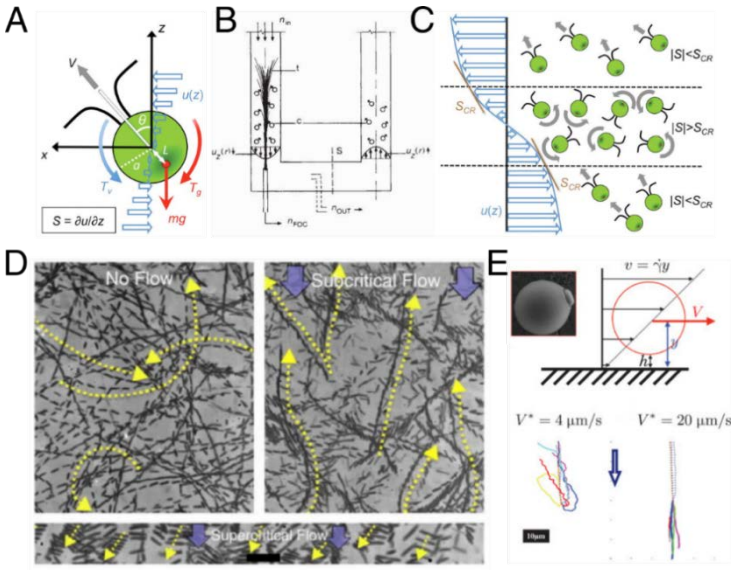

Figure 59:Directional response of micro-swimmers to flow. (**A**) A gyrotactic phytoplankton's centre of mass (red) is displaced from itscentre of buoyancy ($x = z = 0$). As a result, the swimming direction θ in a shear flow, $u(z)$, is set by the balance of gravitational (T_g) and viscous (T_v) torques. V is swimming speed and m is mass[205]. (**B**) Apparatus for demonstrating gyrotactic focusing. Vertical cylindrical tubes are connected by a horizontal section, so that cell-containing fluid flows with velocity distribution $u_z(r)$ is indicated by small arrows attached to spheres which represent cells. The cells swim towards the axis in the downwards stream and towards the periphery in the upward one[192]. (**C**) Schematic of gyrotactic trapping. Cells can migrate vertically at low shear but tumble and become trapped where $|S| > S_{CR}$, accumulating in a thin layer[205]. (**D**) Trajectories of E. coli swimming near a surface in the presence of different flow rates. Under quiescent conditions, E. coli swam preferentially in circular trajectories (top left panel). For low values of shear ($<6.4\ s^{-1}$), bacteria frequently swim upstream (top right panel), whereas at higher shear rates they are dragged downstream (bottom panel)[206]. (**E**) Rheotaxis in artificial colloidal swimmers. (Top left) SEM image of a colloidal particle embedded with a hematite cube. (Top right) A flow is induced along the x direction in the capillary. The particle experiences a shear flow $v = \dot{\gamma} y$, where $\dot{\gamma}$ is the local shear rate, near the nonslip boundary condition. (Bottom) Trajectories of the particles for various flows and $V_p \sim 8\ \mu m/s$[207].

A different physical mechanism comes into play in the case of elongated micro-swimmers, such as sperms and bacteria, which display "rheotaxis," the ability to orient and swim against the direction of flow.[196,208–212] A number of

sperm and bacterial species have been shown to have a tendency to accumulate near surfaces.[60,213–215] As described in Chapter 2, this is due to the steady swimming angle they attain near surfaces, caused by a balance between the shear the bacterial body experiences near the surface which tends to drive the flagella into the bulk and the viscous drag on the flagella in the bulk which exerts a counter torque in the opposite direction. Now, when an external shear flow is imposed, the lighter flagella in the bulk align with the flow and since the bacteria swim away from their flagella, they migrate upstream (Figure 59D). This ability of microorganisms to migrate upstream has been thought to be important in a number of biological processes like sperm navigation inside female reproductive tract to reach the egg cell, or the ability of *Pseudomonas aeruginosa* parasites to colonize environments, such as the bladder, that are inaccessible to other human pathogens.[210,216]

Rheotaxis in a synthetic micro-swimmer, which uses the same physical principles as biological micro-swimmers, i.e., the alignment of the body with the shear and the polar propulsion of the particle, was recently demonstrated by Palacci *et al.*[207] They used polymeric spheres embedded with a hematite cube to create their polar particles. When suspended in H_2O_2 and activated by blue light the hematite cube decomposes the peroxide creating chemical gradients (O_2 and H_2O_2) which induce an osmotic flow on the surface that pulls the hematite cube towards the surface and the particle surfs on this osmotic flow. In the absence of any imposed flow the trajectories were found to be

isotropic and the self-propelled particles were found to have a distinct head and tail with the hematite cube leading. When a flow was imposed on top of this system, they observed that the particle 'body' composed of the polymeric sphere aligned with the flow and the particle propelled towards its hematite 'head' leading to its upstream migration (Figure 59E).

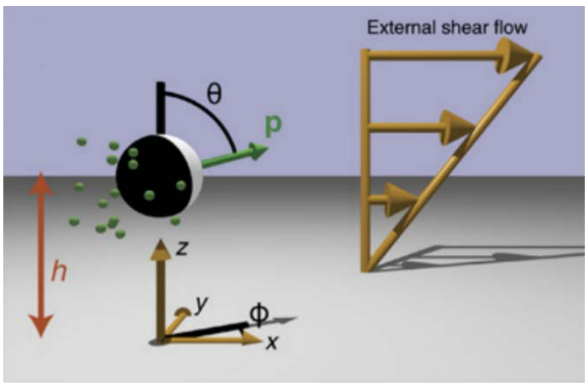

Figure 60: Schematic illustration of the model system. A particle (white sphere) with axisymmetric coverage by catalyst (black) is driven by an external shear flow (large gold arrows) in the $\hat{x}$ direction near a planar wall (gray). The particle has a height h above the wall and an orientation vector **p**, which can be specified by the angles θ and φ. When the particle is active, the cap emits solute molecules (green spheres).

In all the cases of sperm, bacterial and artificial colloidal rheotaxis described above, it was important that the particle had an elongated shape, such that the leading head of the particle swims closer to the surface while the body is aligned with the flow leading to their upstream migration. It is however, a priori unclear how a symmetric spherical self-propelled particle would orient in an imposed flow field (Figure 60). While spherical self-propelled particles such as the silica-Pt colloids lack the elongated shape to align with imposed flows, they

still have a rich interaction with surfaces which imposes an orienting torque on them as described in Chapter 2. In this chapter, I will show that the interplay between an imposed shear flow and the surface proximity induced torques can lead to a surprising and counterintuitive spontaneous transverse orientational order. The particles align almost—but not exactly—in the vorticity direction. As I will discuss in detail, this slight misalignment is a key experimental observation that allows us to identify and understand the physical mechanism behind the directional alignment. Briefly, an inactive, bottom-heavy particle in a flow only rotates as it is carried downstream. However, near-surface swimming activity adds an effective "rotational friction" to the dynamics of the particle because it tends to drive the particle orientation into the plane of the wall. The effective "friction" damps the particle rotation and stabilizes the cross-stream orientation. Finally, the directional alignment, combined with self-propulsion, leads to the cross-stream migration of active particles. The analysis reveals that this mechanism can generically occur for spherical micro-swimmers in a flow near a surface. These findings exemplify the complex behaviour that can emerge for individual micro-swimmers from the interplay of confinement and external fields. Moreover, they show that the qualitative character of the emergent behaviour is sensitive to the details of the interactions (for example, hydrodynamic interactions) between individual micro-swimmers and bounding surfaces.

4.2 Results

4.2.1 Active particles without external flow

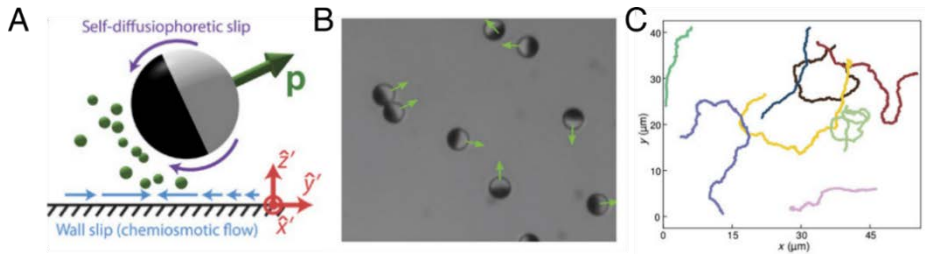

Figure 61: Active particles without flow (**A**)Schematic illustrating the self - diffusiophoretic and chemiosmotic mechanisms that drive the motion of a chemical micro swimmer . The self - generated solute gradient (green spheres) drives flows localized to thin boundary layers on the particle surface (magenta arrows) and on the nearby wall (blue arrows). The particle is shown in the primed frame (red arrows). This frame corotates with the particle around the $\hat{z}$ axis so that the $\hat{z}' = \hat{z}$ and the particle orientation vector **p** is always in the plane spanned by $\hat{y}'$ and $\hat{z}'$. (**B**) Optical microscopy image capturing the distribution of orientations of active particles ($V_p \approx$ 6 μm/s) without an imposed flow. (**C**) Tracked trajectories of active particles without a flow.

In our experiments, we use silica colloids (1-μm radius, or 2.5-μm radius, where noted) half-coated with a thin layer of Pt (10 nm) as active particles. When the particles are suspended in an aqueous H_2O_2 solution, the Pt cap catalyses the degradation of H_2O_2, whereas the silica half remains inert. The asymmetric distribution of reaction products creates a concentration gradient along the surface of the particle, which induces a phoretic slip velocity, resulting in its propulsion away from the Pt cap. In addition, particle-generated concentration gradients can induce chemiosmotic slip on a nearby bounding surface, giving an additional contribution to particle motility. The details of this mechanism, shown schematically in Figure 61A, are comprehensively discussed in Chapter

2 and elsewhere[80,217] and are also the subject of ongoing research[218–221]. When the silica-Pt particles are suspended in water, they are quickly sedimented to the bottom surface because they are density-mismatched (ρ_{SiO2} = 2.196 g/cm^3). They orient with their caps down (θ =0°, where θ is defined in Figure 60) due to the bottom heaviness induced by the Pt layer (ρ_{Pt} = 21.45 g/cm^3). Addition of H_2O_2 introduces activity into the system and changes the orientation distribution of the particles. The particles assume an orientation with the propulsion axis parallel to the bottom surface (θ = 90°). Details of the dynamics leading to this change in orientation of the active particles are discussed in Chapter 3. Briefly, we could show that, whereas the hydrodynamic interactions and the bottom heaviness of the particles tend to drive the caps of the particles toward the surface, the wall-induced asymmetry of the distribution of the chemical product and the chemiosmotic flow along the substrate (see Figure 61A) tend to have the opposite effect, leading to a stable orientation at $\theta \approx 90°$. Once parallel to the surface, the particles are confined to a single plane of motion, where they propel away from their Pt caps (Figure 61B, C) with a typical speed V_p = 6 μm/s. Because of the contrast between the dark Pt hemisphere and the transparent silica, we can measure the angular orientations of these particles (see Appendix A for details of the tracking process). Within the two-dimensional (2D) plane, the particles have no preferred directionality and are diffusive on long time scales.

4.2.2 Passive particles in external flow

Now, we seek to characterize the behaviour of these silica-Pt particles in an imposed flow. Initially, a suspension of the particles in water is introduced in a square glass capillary (1 mm; VitroCom) connected to a computer-controlled microfluidic pump (MFCS-EZ, Fluigent). We allow the particles to sediment to the bottom surface before we impose any external flows. The desired flow rate in the capillary is maintained by using a flow rate monitor (Flowboard, Fluigent), which is in a feedback loop with the microfluidic pump. We begin by imposing a flow of water (no activity) in the *x* direction.

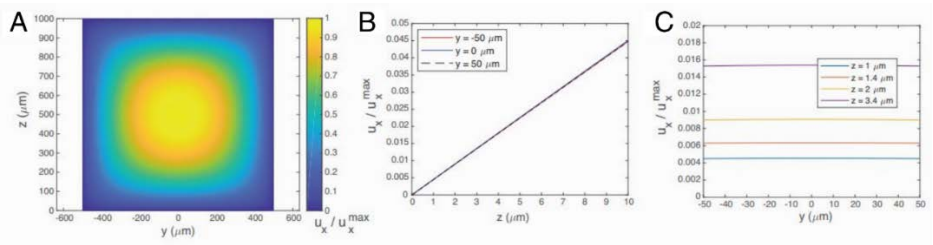

Figure 62: Flow profile in the microfluidic channel. (**A**) Speed of the flow, scaled by the maximum value, as a function of the position in the cross-section of the channel. (**B**) Speed of the flow, scaled by the maximum value, as a function of the vertical position z in the vicinity of z = 0 µm, for several fixed values of y near y = 0 µm. (**C**) Speed of the flow, scaled by the maximum value, as a function of the lateral position y in the vicinity of y = 0 µm, for several fixed values of z near z = 0 µm.

Close to the non-slipping capillary surface, the flow velocity varies linearly as $v_{flow} = \dot{\gamma} z$, and the particles, which are sedimented near the surface, experience a shear flow.[222] The structure of the external flow v, in a rectangular capillary is given by:

$$v_x(y,z) = v_0 \sum_{n,odd}^{\infty} \frac{1}{n^3}\left[1 - \frac{\cos h\left(n\pi \frac{y}{h_c}\right)}{\cos h\left(n\pi \frac{w_c}{2h_c}\right)}\right] \sin\left(n\pi \frac{z}{h_c}\right) \quad (45)$$

Here, w_c is the width of the channel, and h_c is the height of the channel, with y ∈ $[-w_c/2, w_c/2]$ and z ∈ $[0, h_c]$. The parameter v_0 characterizes the strength of the flow. The velocity components v_y and v_z vanish everywhere. For $w_c = h_c$ = 1000 μm, the theoretical flow profile is shown in Figure 62A scaled by the maximum value of the flow speed. In order to determine the validity of the linear shear flow approximation, we focus on a spatial window near y = 0 and z = 0, which is the centre of the bottom wall of the channel. In Figure 62B, we show how the flow speed varies in the z direction for several values of y in the vicinity of y = 0 μm. In the region y ∈ [−50 μm, 50 μm], the flow can clearly be approximated as increasing linearly in the z direction, with negligible variation of the shear rate (i.e., the slope of the flow profile) with y. As a second check, in Figure 62C, we examine how the flow speed changes with y for several fixed values of z near z = 0 μm. We can clearly neglect variation of the flow speed in the y direction. We perform our experimental observations within this window where the assumption of flow varying linearly in z holds true.

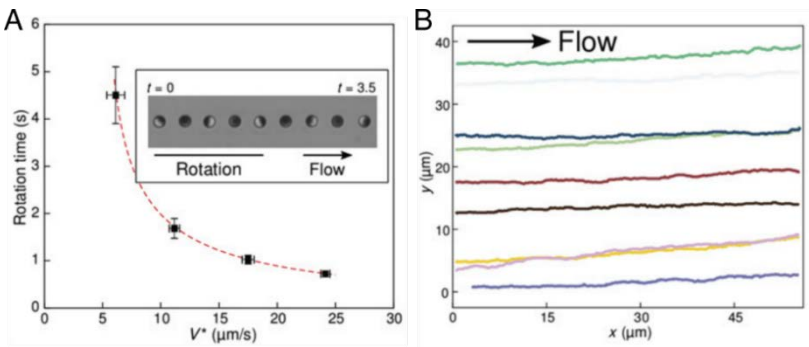

Figure 63: Passive silica-Pt particles in a flow (**A**)The plot shows the dependence of the rotation time on flow velocity.V* is the translational velocity of the passive particle and is used to characterize the flow rate. The red dashed curve represents a fit to the theoretical function $\tau = 2\pi/\sqrt{aV^{*,2} + b}$. Inset: Time-lapse images of a passive particle rolling in a flow. (**B**) Tracked trajectories of passive particles in a flow (V* = 14 μm/s).

In terms of their translational behaviour, we observe that the particles act as "tracers" and translate in nearly straight lines along the direction of flow (Figure 63B). The translational velocity of these particles is proportional to the imposed flow rate. We use the translational velocity *V** of these inactive "tracer" particles to characterize the flow rate. Before we start the flow, the particles are all in the cap-down orientation (θ = 0°). The shear flow induces a torque on the particles, and they rotate around the axis of flow vorticity $\hat{y}$ as they translate in a flow. The rotation speed of the particles is also dependent on the flow rate (Figure 63A), with higher flow rates leading to faster rotation. Through a simple model for particle rolling, we predict the rotational period $\tau = 2\pi/\sqrt{aV^{*,2} + b}$, where *a* and *b* are fitting parameters. This relation shows excellent fit to the data (Figure 63A red curve), and from the fitted *a*, we extract $\dot{\gamma} \approx 1.22\, V^*/R$.

4.2.3 Active particles in external flow

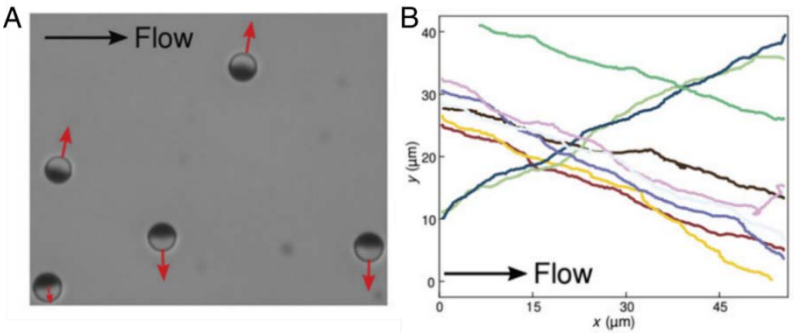

Figure 64: Active particles in a flow. (**A**) Self-propelled particles (Vp = 6 μm) with an external flow imposed, V^* = 14 μm/s. (**B**) Tracked trajectories of active particles in a flow (V^* = 14 μm/s).

We then start a flow of H_2O_2 to introduce activity into the system. We notice that the dynamics of particle behaviour in a flow is markedly influenced in the presence of activity. First, the particles stop rolling and reach a stable orientation parallel to the bottom surface (θ = 90°). This is similar to a previously observed behaviour for the particles in the absence of flow[178]. More surprisingly, the particles also evolve to a stable orientation that is nearly perpendicular to the direction of imposed flow (φ ≈ 90° or −90°; Figure 64A). While the particles continue to translate in *x* due to the imposed flow, they also have the self-propulsion velocity V_p away from their Pt caps. A combination of these effects results in the cross-streamline migration of self-propelled particles, that is, migration of particles in the *y* direction, perpendicular to the flow along the *x* direction. Typical trajectories of cross-stream migrating particles are presented in Figure 64B. Further, we observe that the stability of cross-stream migration (due to the stability of the steady orientation angle φ* perpendicular to the direction of flow) is dependent on the flow rate, with higher flow rates resulting in a stronger alignment effect. The inset of Figure 65 shows the angular evolution of two self-propelled particles in imposed flows of V^* = 14 and 24 μm/s. The deviations away from the φ ≈ 90° positions occur more frequently and at larger amplitude than for particles in lower flow rates.

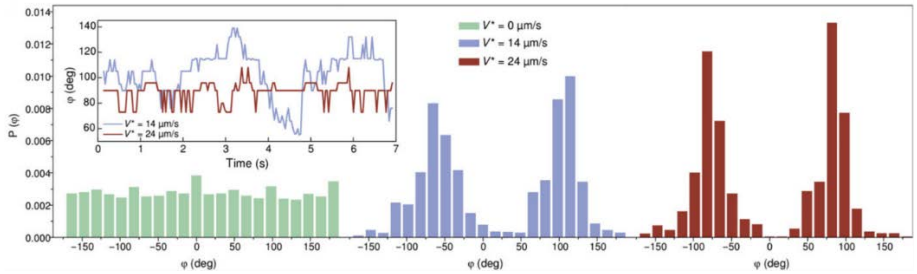

Figure 65: Angular probability distributions of active colloidal particles in the absence of an imposed flow, $V^* = 0$ µm/s (green), at $V^* = 14$ µm/s (blue) and at $V^* = 24$ µm/s (red). Inset shows the angular evolution of two different active colloids at imposed flow rates of $V^* = 14$ µm/s (blue) and $V^* = 24$ µm/s (red).

To study this effect at a population scale, we flow a suspension of self-propelled particles with H_2O_2 and record the angular orientations and positions of every particle in each frame, which allows us to determine the probability distribution of φ in the system. These are plotted in Figure 65 for two different flow rates and compared to the system of self-propelled particles without any imposed flow. In the absence of flow, the distribution is nearly flat, indicating the lack of preference for any orientation φ, and at long time scales, the particle behaviour is purely diffusive. However, in the case of imposed flow, we observe distinct peaks that appear at $\varphi \approx 90°$ and $-90°$. These correspond to the particles exhibiting the cross-stream behaviour. These peaks also become sharper when we increase the flow rate, as can be seen in the distributions for $V^* = 14$ and 24 µm/s. In both cases, closer observation of the angular probability distributions reveals a small bias of orientations in the direction of flow for particles migrating across flow streamlines. Because the particles are subject to Brownian fluctuations, they can also occasionally orient

with or against the flow (φ ≈ 0° or 180°). This leads to an intermittent state where the particles "tumble" in the direction of flow before recovering their φ ≈ ±90° orientation and the cross-streamline behaviour. The recovered orientation of these particles can be different from their initial states, changing the direction of particle migration (for example, from $+y$ to $-y$, see Figure 66).

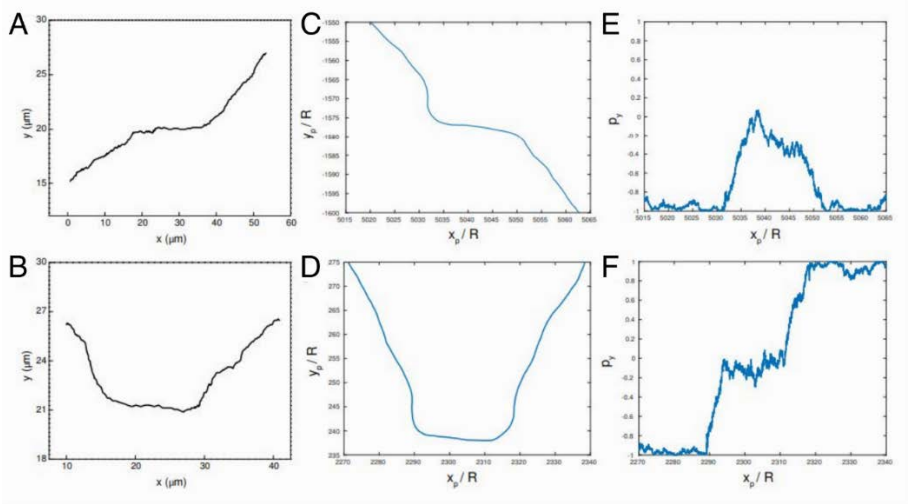

Figure 66: Experimental and numerically obtained trajectories of active particles in a flow: (A-B) Interim states, reminiscent of bacterial "tumbling," can occur for cross stream migrating active particles when the particle orientation is against or with the flow ($\varphi = 0^\circ$ or $\varphi = 180^\circ$, i.e., $p_y = 0$.) For the numerically obtained trajectories in (C) and (D), p_y is shown in (E) and (F), respectively. Eventually particles recover the cross-stream behaviour, either in the same direction as before beginning to "tumble," or the opposite one. Therefore, the interim states are associated with stochastic switching of the particle orientation between two bi-stable states with $p_y \approx \pm 1$.

Apart from the imposed flow rate V^*, we find that the stability of the φ* is also dependent on the particle radius. Using particles of larger radius (2.5 μm), we show that the distribution of φ is narrower around φ = ±90°, as compared to the distribution for R = 1 μm particles for identical V_p and V^* (Figure 67A).

Because the effect of Brownian noise is significantly lower for the larger particles, we also observe that they seldom switch their migration direction within the width of our capillary (Figure 67B). The intermittent tumbling states that occur for the smaller particles do not occur in the case of larger particles.

We can further control the behaviour of particle migration by tuning the self-propulsion velocity V_p of the particles. First, we find that higher propulsion velocities damp the fluctuations around φ* due to higher activity (see Figure 68A). Second, the propulsion velocity also controls the "slope" of the cross-stream migration. To quantify this, we define α to be the offset between the orientation vector **p** and the tracked velocity vector **v** of the particle.

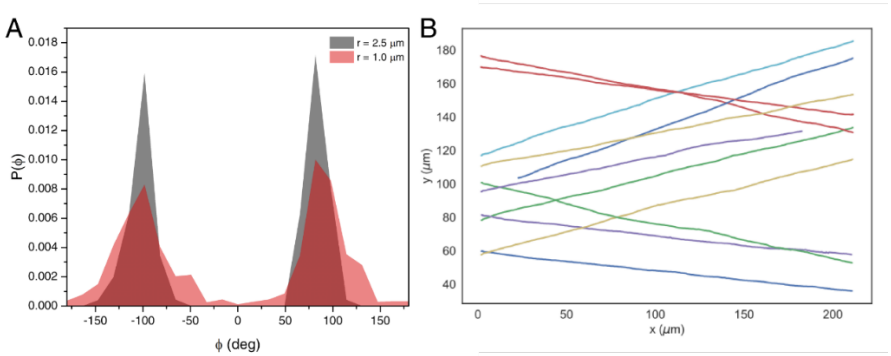

Figure 67: Effect of particle radius on the cross-stream behaviour. (**A**) Probability distribution function of φ for particles of R = 1 and 2.5 μm at $V_p \approx$ 6 μm/s and $V* \approx$ 24 μm/s. (**B**) Sample trajectories of R = 2.5 μm particles show very little deviation from their preferred cross-stream orientation at $V_p \approx$ 6 μm/s and $V* \approx$ 24 μm/s.

For a self-propelled particle in the absence of flow, the particles translate in the direction of the orientation vector **p** as the particles propel away from their

Pt caps (that is, α = 0°), as shown in Figure 68 (B and C). However, with an imposed flow, the translational direction differs from the orientation vector, and the offset α, for a given flow rate, is determined by the V_p of the particles. For particles with V_p = 6 μm/s, the probability distribution function of α has a peak around −64°, whereas for a particle with V_p = 3 μm/s, α is peaked at −83° (Figure 68, B, D, and E). The offset α can be rationalized as a contribution of the transverse propulsion induced by the cross-stream orientation and the longitudinal advection by flow. The α should then simply be given by α = arctan(V^*/V_p). Substituting the experimental values for V_p and V^*, we get α = 66. 9° and 78. 3°, which agree reasonably well with the observed values. This clear separation in peaks of α for different propulsion velocities could eventually be used for the separation of particles based on activity.

The experimental observations can be qualitatively captured and understood within a generic mathematical model of swimming near a surface in external flow[223]. We take a similar approach as in Chapter 2 in constructing dynamical equations for the height and orientation of a heavy spherical active particle and finding their fixed points

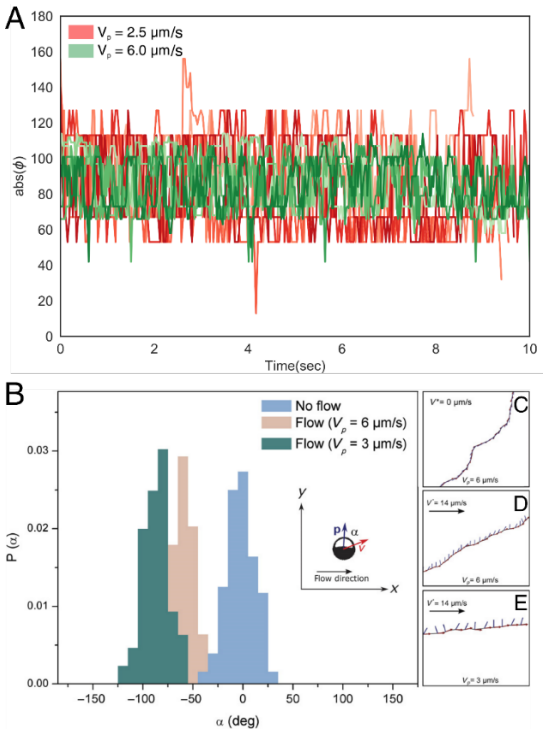

Figure 68: Effect of Vp on the cross-stream migrations behaviour. (**A**) Fluctuations in φ obtained from five different particles for two values of V p at $V^* \approx 24$ μm/s. (**B**) Probability distributions of α for a particle in the absence of a flow with V_p = 6 μm/s and with an imposed flow corresponding to V^* = 14 μm/s for particles of V_p = 6 and 3 μm/s. (**C** to **E**) Tracked orientation vectors (line segments) and instantaneous velocities (arrows) for trajectories at different flow and self-propulsion speeds.

I will briefly describe below the construction of these dynamical equations which show that steady-state behaviours, including cross-stream migration, can emerge from the interplay of external shear flow, near-surface swimming, and gravity. Details on the construction of the theoretical model can be found in Appendix B.

4.3 Construction of theoretical model

The following mathematical model was developed by William E. Uspal

The flow in the suspending fluid is characterized by a low Reynolds number and hence governed by the Stokes equations. Because these equations are linear, the contributions of external flow (*f*), gravity (*g*), and swimming (*s*) to the particle translational and angular velocities can be calculated independently and superposed: $\mathbf{U} = \mathbf{U}^{(f)} + \mathbf{U}^{(s)} + \mathbf{U}^{(g)}$ and $\Omega = \Omega^{(f)} + \Omega^{(s)} + \Omega^{(g)}$. The velocity of the orientation vector is determined by $\dot{\mathrm{p}} = \Omega \times \mathrm{p}$.

To calculate the contribution of the external flow to the particle velocity, we consider a neutrally buoyant and inactive sphere of radius *R* in shear flow at a height *h* above a uniform planar wall. Shear spins the particle around the vorticity axis $\hat{y}$, as shown in the left panel of Figure 69. This is because the flow is faster near the upper surface of the particle (that is, the surface farther away from the wall) than near the bottom surface. Accordingly, the particle has angular velocity $\Omega^{(f)} = \frac{1}{2}\dot{\gamma} f(h/R)\hat{y}$. In addition, the particle is carried downstream with velocity $U^{(f)} = \dot{\gamma} h g(h/R)\hat{x}$. The functions f (h/R) and g (h/R) represent the influence of hydrodynamic friction from the wall[224]. Because of the spinning motion of the particle, the tip of the vector **p** traces a circle in the shear plane

$$\dot{\mathbf{p}}^{(\mathrm{f})} \equiv \Omega^{(\mathrm{f})} \times \mathbf{p} = \frac{1}{2}\dot{\gamma} f(h/R)[p_z\hat{x} - p_x\hat{z}] \tag{46}$$

The component p_y is a constant determined by the initial orientation of the particle. The radius of the circular orbit is $\sqrt{1 - \mathrm{p}_{\mathrm{y}}^2}$, and the speed of the tip $\left|\dot{\mathrm{p}}^{(\mathrm{f})}\right|$ is proportional to the circle radius.

Now, for a heavy, active particle moving in quiescent fluid (no external flow) near the same surface, the particle has an axisymmetric (*ax*) geometry and surface activity profile; accordingly, we can define $\mathbf{U}^{(ax)} \equiv \mathbf{U}^{(s)} + \mathbf{U}^{(g)}$ and $\Omega^{(ax)} \equiv \Omega^{(s)} + \Omega^{(g)}$. This system is depicted in the middle panel of Figure 69. Similar to the analysis performed for the case of flow above ($\mathbf{U}^{(f)}$ and $\Omega^{(f)}$), it is possible to write down the contributions arising from effect of bottom heaviness and interactions with the wall (for example, hydrodynamic interactions) that originate in swimming activity. Superposing all contributions from flow, activity and bottom heaviness we obtain equations for $\dot{\boldsymbol{p}} = \boldsymbol{\Omega} \times \boldsymbol{p}$ and $\dot{h} = U_z$ in the following form

$$\dot{p_x} = \frac{1}{2}\dot{\gamma} p_z f(h/R) - \frac{\Omega_{x'}^{(ax)}(p_z, h/R) p_x p_z}{\sqrt{1-p_z^2}} \tag{47}$$

$$\dot{p_y} = -\frac{\Omega_{x'}^{(ax)}(p_z, h/R) p_y p_z}{\sqrt{1-p_z^2}} \tag{48}$$

$$\dot{p_z} = -\frac{1}{2}\dot{\gamma} p_x f(h/R) + \Omega_{x'}^{(ax)}(p_z, h/R)\sqrt{1-p_z^2} \tag{49}$$

$$\dot{h} = U_z = U_{z'}^{(ax)}(p_z, h/R) \tag{50}$$

and the components of the translational velocity **U** in the *x* and *y* directions are determined by **p** and *h* as

$$U_x = \dot{\gamma} h g(h/R) + \frac{U_{y'}^{(ax)}(p_z, h/R) p_x}{\sqrt{1-p_z^2}} \tag{51}$$

$$\mathrm{U_y} = \frac{U_{y'}^{(ax)}(p_z, h/R) p_y}{\mathrm{p_y}\sqrt{1-\mathrm{p_z^2}}} \tag{52}$$

Equation 47 to 52 fully describe a deterministic active sphere in external shear flow near a planar surface. Note that we have defined a new, "primed" frame that has $\hat{y}'$ and $\hat{z}'$ in the plane of mirror symmetry, with $\hat{z}' = \hat{z}$. This frame is convenient for calculations because $\Omega^{(ax)}$ is strictly in $\hat{x}'$

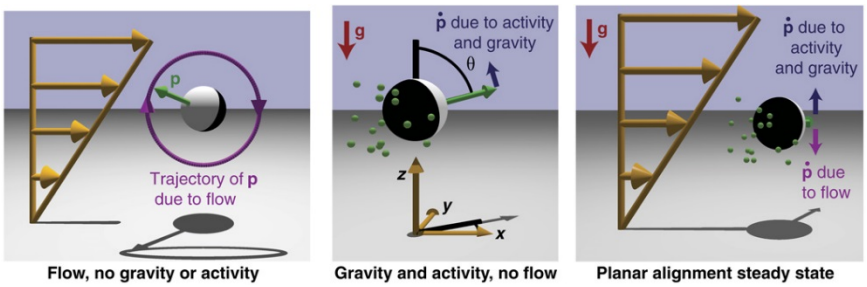

Figure 69: Schematic of the contributions to planar alignment steady state. (**Left**) A neutrally buoyant, inactive sphere driven by an external shear flow (gold arrows) near a planar wall. Because the external flow spins the particle around the vorticity axis (that is, the normal to the shear plane), the tip of the particle orientation vector $\mathbf{p}$ traces a circular path (magenta). (**Middle**) An active, heavy sphere in quiescent fluid. Because the wall is uniform, and the geometry and activity profile of the particle are axisymmetric, the tip of the orientation vector can only rotate in the $\hat{\theta}$ direction, that is, directly toward or away from the wall. (**Right**) Planar alignment steady state, where $p_z^* = 0$, but the particle orientation vector has nonzero components p_x^* and p_y^* in the flow and vorticity directions, respectively. For planar alignment, the component p_x^* in the flow direction can be either upstream ($p_x^* > 0$) or downstream ($p_x^* < 0$), as determined by the function $\Omega_{x'}^{(ax)}(p_z, h/R)$; the downstream case is shown. All contributions to $\dot{\mathbf{p}}$ are in the $\hat{z}$ direction (see Eqs. 47 to 50). At a certain angle φ^*, all contributions to $\dot{\mathbf{p}}$ balance, as shown by the arrows, so that $\dot{\mathbf{p}} = 0$. Note that this fixed point always occurs in pairs related by mirror symmetry across the shear plane; we show the state with $p_y > 0$.

Now, we look for the fixed points ($\mathbf{p}^*$, h^*) of Eqs. 47 to 50 similar to the analysis performed in Chapter 3. A fixed point is a particle configuration in which the particle translates along the wall with a steady height and orientation, that is, $\dot{\mathbf{p}} = 0$ and $\dot{h} = 0$[223]. We find that the system has three fixed points, shown in Figure 70.

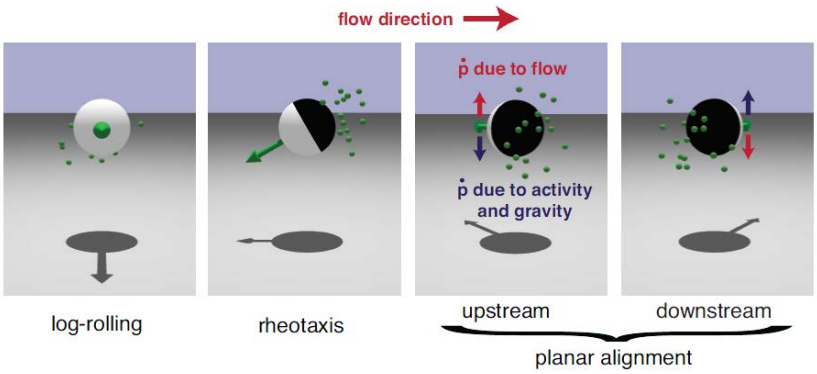

Figure 70: Schematic illustration of the three fixed point solutions to Eqs. 47-50.

Of these three, planar alignment shows excellent qualitative agreement with the experiment observations: The particle orientation is within the plane of the wall ($p_z^* = 0$) and has nonzero components in both the flow and vorticity directions. These criteria are not satisfied by the other two fixed points. Therefore, slight misalignment from the vorticity axis is a key experimental observation that discriminates between the steady states predicted by theory. For planar alignment, the streamwise component p_x^* is

$$p_x^* = cos(\phi^*) = \frac{2\Omega_{x'}^{(ax)}(p_z^* = 0, h^*/R)}{\dot{\gamma} f(h^*/R)} \tag{53}$$

If we assume that the steady height of the particle is not significantly affected by flow rate, then Eq. 53 predicts that the steady-state orientation approaches the vorticity axis as the flow rate is increased, that is, cos(φ*) ~ 1/*V**.

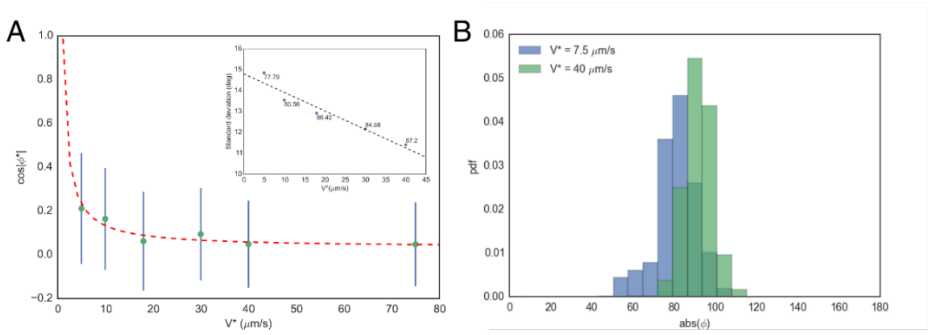

Figure 71: Dependence of | cos(φ*)| on V*. (**A**) The mean px = | cos(φ*)| plotted as a function of V*. Data was obtained from experiments with R = 2.5 μm particles at different flow rates. The dotted line is a fit to the predicted scaling relation. We clearly recover the asymptotic prediction of the scaling relation, i.e., that px = | cos(φ*)| approaches zero for fast flow. (Inset) The dependence of standard deviation of φ* as a function of V* is approximately linear. Numbers show the mean φ*. (**B**) Probability distribution of |φ| plotted for two different flow velocities (corresponding to two data points in A) shows a clear shift of the peak position φ* towards 90° at higher flow rates ($V_p \approx$ 6 μm/s, R = 2.5 μm).

Accordingly, we perform further experiments with 5-μm-diameter particles, which allow for excellent resolution of their orientation (Figure 71). We perform the experiments at six different flow rates in the range accessible with the current experimental setup, V^* = 5 to 75 μm/s, for particles with V_p = 6 μm/s. In Figure 71, we plot cos|φ*| against V^* and find that the data recovers the predicted asymptotic behaviour.

4.3.1 Comparison with experimental trajectories

Eqs. 47 to 50 have been derived in general and do not contain the specifics of the particle composition or self-propulsion. We can calculate the various terms in Eqs. 47 to 50 by using a simple, well-established model of neutral self-diffusiophoresis in confinement[89,178,180,217,225,226]. In the model, the particle has

a hemispherical catalytic cap (Figure 61A, black), and the orientation vector **p** points from its catalytic pole to its inert pole. The particle emits solute molecules (that is, oxygen) at a constant, uniform rate from its cap, leading to self-generated solute gradients in the surrounding solution. These gradients drive surface flows on the particle (Figure 61A magenta arrows) and on the wall (blue arrows), leading to directed motion of the particle.

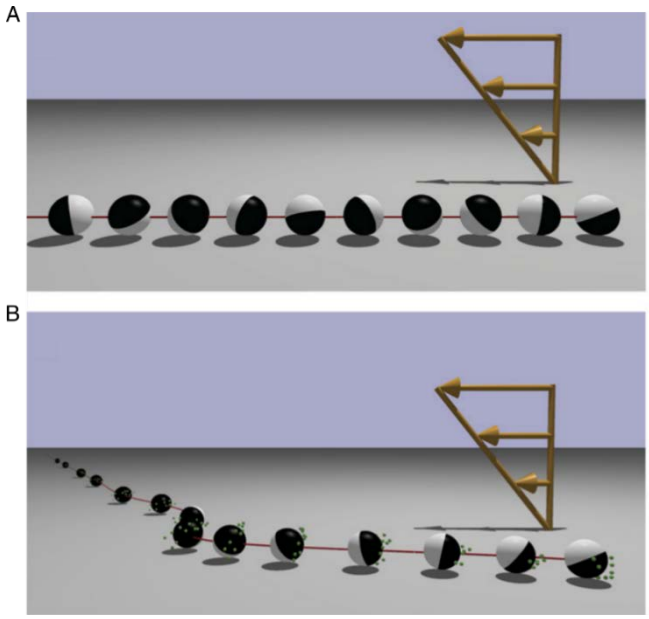

Figure 72: Numerically obtained trajectories of inactive and active particles in flow. (**A**) Numerically computed trajectory of a passive bottom-heavy particle near a wall (grey) and driven by an external shear flow (gold arrows) with dimensionless strength $\dot{\gamma}R/U_0 = 0.1$. The initial condition of the particle is $\theta_0 = 30^\circ$ and $\varphi_0 = 315^\circ$, and the particle height is fixed as $h/R = 1.2$. The particle rotates and is carried downstream by the external flow with no cross-streamline migration. (**B**) Numerically computed trajectory of an active Janus particle with the external flow strength, particle materials, and initial conditions as in (A). The particle rotates so that its inert face points largely in the $-\hat{y}$ direction, with a slight downstream orientation ($p_x > 0$). With this steady orientation, the particle swims across flow streamlines as it moves downstream.

We consider some illustrative examples using dimensionless parameters comparable to those in the experiments and obtaining sample trajectories by numerical integration. In Figure 72B, we show a particle trajectory in a shear flow with strength $\dot{\gamma}R/U_0 = 0.1$ and initial orientation θ_0 = 30° and φ_0 = 315°. The particle rotates so that its inert face points largely in the $-\hat{y}$ direction but with a small downstream orientation (p_x > 0). Notably, this slight downstream orientation agrees with experimental observations. If the particle is inactive (but still bottom-heavy), then from the same initial orientation, the particle simply translates in the flow direction (Figure 72A), rotating as it does so. In Figure 73, phase space trajectories are shown on the unit sphere $|\mathbf{p}| = 1$. The initial orientation in Figure 73(A and B) is indicated by magenta circles in Figure 73 (A and B, respectively). We see that an inactive particle (Figure 73A) has a continuous family of closed orbits in $\mathbf{p}$. When the particle is active, these oscillations are damped, and trajectories in the phase space are attracted to the fixed point (Figure 73B and C). In Figure 73C, we show the effect on the structure of trajectories as the flow strength is increased. For stronger flows, the approach to the fixed point is more oscillatory. Figure 73D shows the contribution of activity in the absence of an external flow.

The phase portraits also provide an intuitive way to understand the stability condition. Consider the bottom-heavy, inactive particle with the phase portrait shown in Figure 73A. How does adding activity transform this portrait into that shown in Figure 73B? The contribution of activity to $\dot{\mathbf{p}}$ is shown as the vector

field in Figure 73D. Because this vector field is small but nonzero on the equator $p_z = 0$, adding it to the portrait in Figure 73A will shift the centre of oscillation (cyan circle) slightly toward the axis $p_x = 0$, producing the green circle in Figure 73B.

More significantly, the addition of this vector field will destabilize continuous oscillatory motion in the following way. Consider the closed trajectories in Figure 73A that are closest to the cyan circle. In the neighbourhood of the equator, activity always "pushes" the vector **p** toward the equator (here, neglecting the small value on the equator, the main effect of which is to shift the fixed point). Therefore, over each period of oscillation, the orientation vector will get slightly closer to the fixed point, transforming the closed circular orbits into decaying spiral orbits.

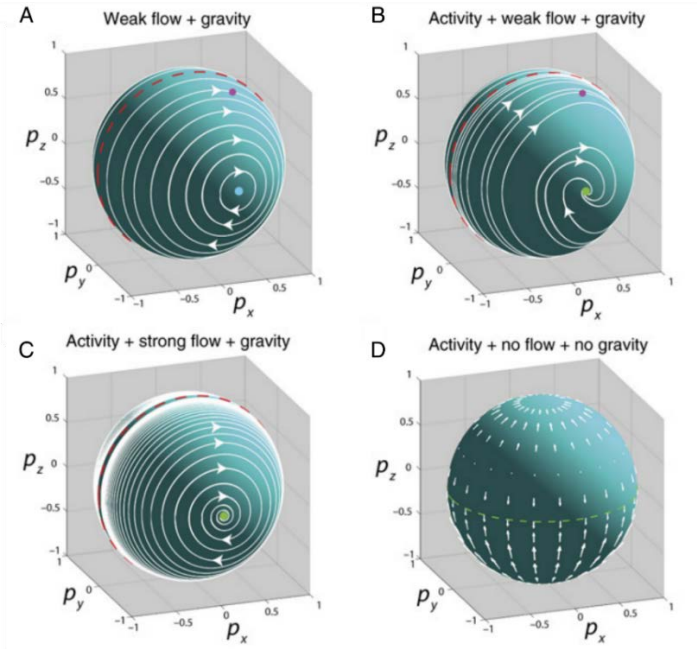

Figure 73: Phase portraits of inactive and active particles in flow. (**A** to **C**) Phase portraits on the sphere $|\boldsymbol{p}| = 1$ for an inactive, bottom-heavy particle (A) in shear flow with $\dot{\gamma}R/U_0 = 0.1$ and for an active, bottom-heavy particle (B and C) in a flow with $\dot{\gamma}R/U_0 = 0.1$ (B) and $\dot{\gamma}R/U_0 = 0.5$ (C). The red dashed lines indicate the plane of mirror symmetry $p_y = 0$. The cyan circle in (A) indicates the centre of oscillatory motion. Green circles in (B) and (C) indicate stable fixed points ("attractors"). For (A) and (B), the magenta circles show the initial conditions for the trajectory in Figure 72A (A) and that in Figure 72B (B). (**D**) Vector field on the unit sphere representing the contribution of activity to the motion in (B) and (C). The green dashed line indicates $p_z = 0$.

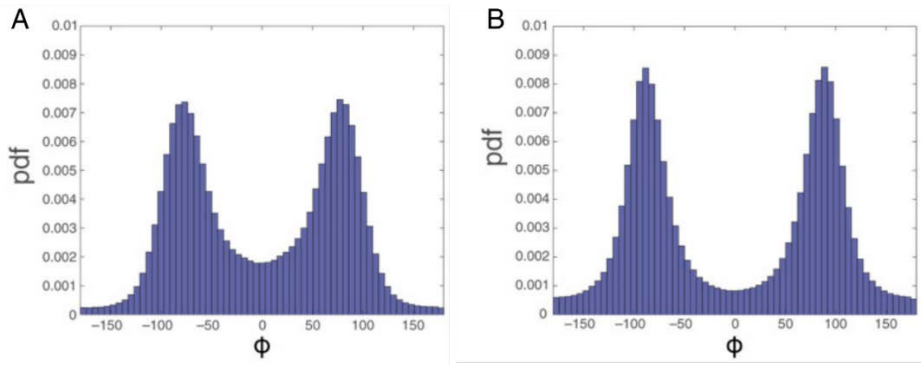

Figure 74: Brownian Dynamics Simulations. (**A**) Probability density function (pdf) for φ, for a catalytic Janus particle in a shear flow with $\dot{\gamma}R/U_0 = 0.1$. (**B**) Probability density function for the same particle with $\dot{\gamma}R/U_0 = 0.5$.

As a further exploration, we consider the effect of thermal noise on the particle orientation by performing Brownian dynamics simulations. In Figure 74A, we show the probability distribution functions for the φ obtained for a Janus particle driven by shear flow at dimensionless inverse temperature Pe_p = 500 and shear rate $\dot{\gamma}R/U_0 = 0.1$. The distribution is symmetric and has two peaks near the steady angle φ* = ±80.9° predicted by the deterministic model (Figure 74A). For a higher shear rate $\dot{\gamma}R/U_0 = 0.5$, we find that the peaks in φ are sharper (Figure 74B), in qualitative agreement with the experiments, with the peaks shifted near the deterministic prediction for this shear rate, φ* = ±88.2°.

4.4 Concluding remarks

In this chapter I have described how we use catalytic Janus particles as a well-controlled model experimental system to study spherical active particles in confined flows. We demonstrate that spherical active particles near surfaces, when exposed to external flows, can exhibit robust alignment and motion along the cross-stream direction. Our model reveals how this behaviour arises from the interplay of shear flow and swimming in confinement. The steady orientation is determined by a balance of contributions to the angular velocity of the particle from shear flow, bottom heaviness, and swimming near a planar substrate. Near-surface swimming introduces an effective friction opposing the rotation of the particle away from the preferred orientation. The

mechanism is generic in the sense that it can occur for any spherical micro swimmer with axisymmetric actuation and is not specific to a particular mechanism of propulsion (for example, chemical or mechanical). As a consequence of the alignment, the particles migrate across the streamlines of the external flow as they are carried downstream.

To the best of our knowledge, our results are the first to demonstrate that swimmer/surface interactions (for example, hydrodynamic interactions) can drive a rich directional response of spherical particles to external flows. This is in contrast with previous works on natural micro swimmers (for example, bacteria), where complex body shapes and flagellar beat patterns were implicated in directional response[196,199]. In addition, we have obtained semiquantitative agreement between particle orientational statistics obtained from the experiments and from the theoretical model.

For lab-on-a-chip devices that use continuous flows and artificial micro swimmers, our findings imply that the micro swimmers would have a tendency to migrate to the confining side walls of the device. Our findings additionally raise the possibility that in dense suspensions of micro swimmers, for which fluid flows are self-generated, the collective behaviour of the suspension may be sensitive to the detailed interactions between individual micro swimmers and bounding surfaces.

4.5 Appendix A: Tracking of Janus particles

Particle tracking was performed using an automated tracking program developed in-house. The Python-based program uses OpenCV library for image processing and NumPy for data handling. In source videos filmed in grayscale, each frame was first cleaned of noise by using blurring techniques, which substituted each pixel with an average of its surroundings. The particles were then separated from the background by using either of the two segmentation methods: threshold and gradient. In the threshold method, given a grayscale image *img*(*x*,*y*) and a threshold value *T*, this operation resulted in a binary image *out*(*x*,*y*) given by

$$out(x,y) = \begin{cases} 1 \; if \; img(x,y) \geq T \\ 0 \; if \; img(x,y) < T \end{cases} \tag{54}$$

The gradient method was used for images with irregular brightness or when the particles were hard to distinguish from the background. In the first step of this method, the gradient of the image($\nabla \mathrm{img} = \left(\frac{\partial \mathrm{img}}{\partial \mathrm{x}}, \frac{\partial \mathrm{img}}{\partial \mathrm{y}}\right)$) is approximated by convolving the original frame with a Sobel operator. This results in two images, one that is the derivative along the *x* axis and another that is along the *y* axis. These images are then thresholded and joined together to obtain the segmented image. The final result has the edges of the detected particles.

The centre of each particle was approximated as the centre of mass of the contours obtained after segmentation. Particle trajectories were calculated using Bayesian decision-making, linking every particle centre with the previous

closest one. Intermediate missing positions, if any, were interpolated using cubic or linear splines.

To calculate the **p** vector, a line of predefined radius (approximately equal to the particle radius) was drawn through the centre at a test angle. The SD of the pixel values along the test line was calculated and stored. The process was repeated multiple times, and the SDs were compared. The test angle with the least SD was assumed to correspond to the separator between the silica and Pt halves and the vector orthogonal to it, the orientation vector (Figure 75).

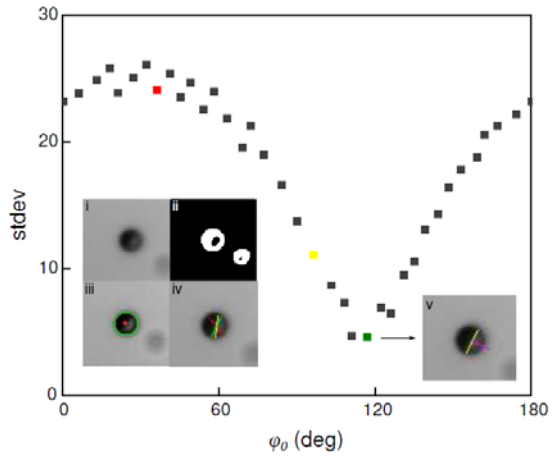

Figure 75: Automated tracking of the orientation angle of Janus particles. The plot shows the standard deviation of the grey scale values along different lines (l = 2r) crossing the particle through the centre. Each line is defined by an angle (ϕ_0), calculated from the reference system of the image. The angle with lowest standard deviation corresponds to the direction that separates the black and white halves of the Janus particle. The insets show the process of centre and angle detection. i) Original image, ii) binary image that results from applying adaptive thresholding, iii) Contour taken from the binary image, and centre computed from the centre of mass, iv) Different test lines used for the grey scale standard deviation calculation. Each one corresponds to a similarly coloured point in the graph, v) The line with lowest standard deviation is

selected and the final orientation (ϕ) is taken to be the one perpendicular to that (pink), pointing towards the bright half of the Janus particle.

4.6 Appendix B: Theoretical calculation of particle velocity

These calculations were performed by William Uspal

Here, we presented our model for the calculation of the particle velocities **U** and Ω as a function of h and **p**. We took the instantaneous position of the particle to be $\mathbf{x}_p = (x_p, y_p, h)$ in a stationary reference frame. The catalytic cap emitted a product molecule at a constant and uniform rate κ. We took the solute number density $c(\mathbf{x})$ to be quasi-static, that is, it obeyed the equation $\nabla^2 c = 0$ with boundary conditions $-D\hat{n} \cdot \nabla c = \kappa$ on the cap, $\hat{n} \cdot \nabla c = 0$ on the inert region of the particle surface, and $\hat{n} \cdot \nabla c = 0$ on the wall. Here, D is the diffusion coefficient of the solute molecule, **x** is a location in the fluid, and $\hat{n}$ and is the normal vector pointing from a surface into the liquid. For each instantaneous configuration (h, **p**), this set of equations can be solved for $c(\mathbf{x})$, for example, numerically by using the boundary element method[223,227].

We took the velocity $\mathbf{u}(\mathbf{x})$ in the fluid solution to obey the Stokes equation $-\nabla P + \eta\nabla^2\mathbf{u} = 0$, where η is the solution viscosity and $P(\mathbf{x})$ is the pressure in the solution. In addition, the fluid was incompressible so that $\nabla \cdot \mathbf{u} = 0$. The Stokes equation is a linear equation. Therefore, the contributions to **U** and Ω from various boundary conditions for **u**, and from various external forces and torques, can be calculated individually as the solution to separate subproblems and then superposed. Hence, we write $\mathbf{U} = \mathbf{U}^{(f)} + \mathbf{U}^{(ax)}$ and $\Omega = \Omega^{(f)} + \Omega^{(ax)}$, where ($f$)

indicates the contributions of the external flow, and the axisymmetric (*ax*) contributions are from gravity (*g*) and swimming (*s*) activity: $\mathbf{U}^{(ax)} = \mathbf{U}^{(g)} + \mathbf{U}^{(s)}$ and $\Omega^{(ax)} = \Omega^{(g)} + \Omega^{(s)}$. For each subproblem, the fluid is governed by the Stokes equation and incompressibility condition.

We first considered the subproblem for the contribution of the external flow. The fluid velocity was subject to no-slip boundary conditions $\mathbf{u} = 0$ on the planar wall and $\mathbf{u} = \mathbf{u}_{ext} + \mathbf{U}^{(f)} + \Omega^{(f)} \times (\mathbf{x} - \mathbf{x}_p)$ on the particle. Here, $\mathbf{u}_{ext}$ is the external flow velocity, $\mathrm{u_{ext}} = \dot{\gamma} z \hat{\mathrm{x}}$. In addition, the particle was free of external forces and torques, closing the system of equations for $\mathbf{U}^{(f)}$ and $\Omega^{(f)}$. The solution of this subproblem is well known [see, for instance, the study of Goldman *et al.*[224]].

The two axisymmetric subproblems were calculated in the primed frame corotating with the particle (Figure 61A). For the subproblem associated with particle activity, we used the classical framework of neutral self-diffusiophoresis. In this subproblem, the self-generated solute gradients drive surface flows on the wall and the particle surface, $\mathbf{v}_s = -b(\mathbf{x}_s')\nabla_{||}c(\mathbf{x}')$, where $\nabla_{\|} \equiv (1 - \hat{\mathrm{n}}\hat{\mathrm{n}})$, and $\mathbf{x}_s'$ is a location on a surface (in the primed frame). The "surface mobility" $b(\mathbf{x}_s')$ encapsulates the details of the molecular interaction between the solute and the bounding surfaces. We wrote the boundary conditions $\mathbf{u} = \mathbf{U}^{(s)} + \Omega^{(s)} \times (\mathbf{x}' - \mathbf{x}_p') + \mathbf{v}_s(\mathbf{x}_s')$ on the particle and $\mathbf{u} = \mathbf{v}_s(\mathbf{x}_s')$ on the wall. Again, specifying that the particle was force- and torque-free closed the system of equations for $\mathbf{U}^{(s)}$ and $\Omega^{(s)}$. This subproblem can be solved numerically using the boundary element method. For the subproblem

associated with gravity, we used the "eggshell" model of Campbell and Ebbens[194] for the shape of the cap, taking the cap thickness to vary smoothly from zero at the particle "equator" to a maximum thickness of t at the active pole.

In the following, we specify the parameters characterizing the system. We chose to take the inert and catalytic regions of the particle to have different surface mobilities, b_{inert} and b_{cap}, with $b_{\text{inert}}/b_{\text{cap}} = 0.3$ and $b_{\text{cap}} < 0$. For this parameter, a neutrally buoyant Janus particle, when it was far away from bounding surfaces, moves in the **p** direction (that is, away from its cap) with a velocity $U_{fs} = 13/80\ U_0$, where $U_0 = |b_{\text{cap}}|\kappa/D$[228]. The wall was characterized by a surface mobility b_w. We chose $b_w/b_{\text{cap}} = -0.35$. These surface mobility ratios were chosen to be similar to those used in a previous work [where we had $b_{\text{inert}}/b_{\text{cap}} = 0.3$ and $b_w/b_{\text{cap}} = -0.2$[178]], and to give a slightly downstream steady orientation. We nondimensionalized length with R, velocity with U_0, and time with $T_0 = R/U_0$. To nondimensionalize the gravitational and shear contributions, we must estimate U_0 in real, dimensional units. Rather than to calculate U_0 directly, which requires estimates for κ and $|b_{\text{cap}}|$, we used the expression $U_{fs} = 13/80\ U_0$. Knowing that, experimentally, the particle characteristically moves at $U_{fs} \approx 5$ μm/s when it is far from surfaces, we obtained $U_0 \approx 30$ μm/s. The parameters describing the heaviness of the particle are given in the Supplementary Materials. Finally, we considered the shear rate $\dot{\gamma}$. This was not known experimentally but could be roughly

estimated by considering inactive particles to act as passive tracers. From Goldman *et al.*[224], the velocity of a spherical particle driven by shear flow near a wall is $\mathrm{U}_{\mathrm{x}}^{(\mathrm{f})} = \mathrm{g}(\mathrm{h}/\mathrm{R})\dot{\gamma}\mathrm{h}$. Experimentally, inactive particles in a flow were observed to move with $V^* \sim 10$ μm/s. The particle height h is difficult to observe experimentally, but we took it to be set by the balance of gravity and electrostatic forces. Hence, the particle/wall gap δ was on the order of a Debye length $\lambda_D \sim 0.1R$ so that $h \sim 1.1R$. For $h/R \geq 1.05$, the factor $g(h/R) \approx 1$. Therefore, we estimated $\dot{\gamma} \approx 10\,\mathrm{s}^{-1}$ and a typical dimensionless shear rate to be $\dot{\gamma}\mathrm{R}/\mathrm{U}_0 \approx 0.8$. As a reminder, our aim was to establish semiquantitative agreement with experiments, and therefore, we sought only an order of magnitude accuracy in the dimensionless parameters.

In assuming the concentration field to be quasi-static, we neglected the advective effects on the solute field by the external shear flow and by the finite velocity of the particle. These approximations are valid for small Peclet numbers $\mathrm{Pe} \equiv U_{fs}R/D$ and $\mathrm{Pe}_{\dot{\gamma}} \equiv \dot{\gamma}\mathrm{R}^2/\mathrm{D}$. At room temperature, the diffusion coefficient of oxygen was $D \sim 4 \times 10^{-9}\mathrm{m}^2/\mathrm{s}$[229] so that Pe ≈ 0.003 and $\mathrm{Pe}_{\dot{\gamma}} \approx 0.015$. Furthermore, in taking the fluid velocity **u** to be governed by the Stokes equation, we neglected fluid inertia. This approximation is justified for low Reynolds number, $\mathrm{Re} = \rho_{\mathrm{fluid}}U_0R/\eta$, where η is the dynamic viscosity of the solution. Using $\eta \sim 10^{-3}$Pa s for water, we obtained $\mathrm{Re} \approx 10^{-4}$.

5.Conclusions and final remarks

Natural micro swimmers possess a remarkable ability to sense and respond to their local environment through interactions arising from their self-propulsion.[230] This is evident in the tendency of motile microorganisms to actively accumulate close to confining surfaces, which has biological advantages, for example in finding nutrients and in forming stable colonies that enhances their survival.[231] Another set of responses are what have come to be classified under 'taxis', such as chemotaxis[183], phototaxis[232] or gravitaxis[233], the ability of the microorganisms to adjust their self-propulsion in response to local gradients. This enables the swimmers, such as bacteria to migrate towards nutrient rich areas and away from toxic ones (chemotaxis) or phytoplankton to swim towards areas with greater exposure to light (phototaxis).

It has been of great interest to understand these effects, and to determine if they originate due to some complex physiological mechanism specific to the concerned micro-organism or are a general consequence of self-propulsion. It has been suggested for example that near field hydrodynamic effects cause by the beating flagella of micro-organisms close to surfaces[214,234] and direct ciliary contact dominates the accumulation effects observed in micro-organisms[235]. In this thesis, by using simple, spherical active particles as a model active matter system, we have sought to address if similar effects can also be observed in artificial active matter systems that lack the physiological complexity of biological micro-swimmers[178].

We have shown that spherical self-phoretic particles also have a strong tendency to accumulate close to surfaces. This effect originates from the modification of the hydrodynamic and phoretic fields created by the self-propelling particles close to surfaces[180]. We have described how these interactions lead to orientational quenching, effectively restricting the active particle trajectory close to the confining surface. The torques arising from the interactions with the surface counter-act any rotation away from a stable orientation due to thermal noise. We have in fact used this tendency of the active particles to attain stable orientation to demonstrate a guidance system for self-propelled particles by introducing topographical patterns.

5.1 Towards understanding chemiosmotic flows

Topographical patterns however are not the only way to control active particle trajectories through surface interactions. Self-phoretic particles close to surfaces create a gradient in the chemical composition of the solution along the surface. This gradient leads to a chemiosmotic flow which couples back to the particle and provides an additional component to its self-motility. Now, this chemiosmotic flow along the surface is dependent on the material properties of the surface. Uspal *et al.* showed in simulations that this property can be exploited to guide catalytically active particles by creating a surface with chemically patterned walls, such that an inhomogeneous mobility exists along the surface[236]. Popescu *et al.* extended these results to show that it is possible to achieve directed migration of active particles near osmotic

responsive walls with surface chemistry gradients (thigmotaxis)[237]. It should be possible to test these results experimentally by using standard lithography techniques to create chemically patterned surfaces. However, understanding the relation between the material properties of a surface and the 'surface mobility' it presents for a catalytically active particle will require very through and exhaustive experimental approach.

We have recently begun some experimental studies to try and sketch out the characteristics of these chemiosmotic flows. Our initial experiments have involved studying the dynamics of passive particles around motile active particles. Typically, this sort of an experiment is performed by trapping the swimmer with an optical tweezer or a micro manipulator and measuring the trajectories of passive particles around it. However, since the Janus particles are very small and coated with a metal cap, it is not feasible to use these techniques here. We instead carry out our measurements through a particle detection algorithm. Briefly, we suspend a few active particles in a solution of sparsely distributed smaller passive particles (silica colloids). Both the active and passive particles are density mismatched and sediment close to the surface. After we add H_2O_2, the active particles swim close to the surface due to the orientational quenching effect described in Chapter 2.

We track the position and the in-plane orientation angle of the active particle in every frame. With this information, we can recreate a movie from the particle 'frame of reference' where the active particle has a constant position and orientation, and we can measure the trajectories of the passive particles relative to the active particle. An example of the kind of interaction that would be captured in this analysis is shown in Figure 76A.

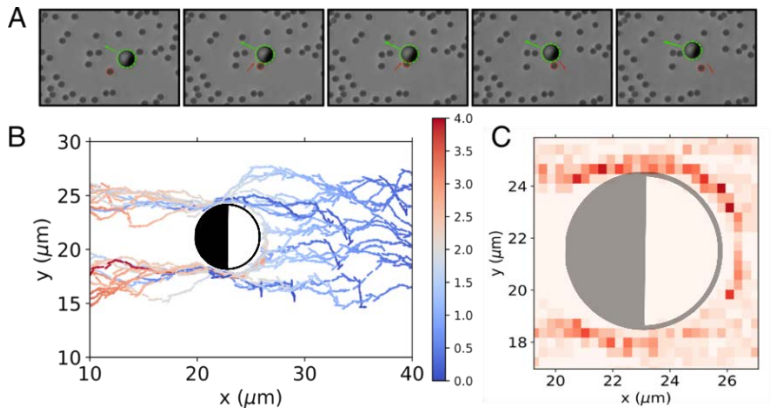

Figure 76: Interactions of passive particles with motile active particles. (A) Snapshots of a passive particle being drawn in close to the equator of the active particle and being repelled at the back. (B) Tracked trajectories of passive particles relative to the active particle. (C) Position probability distribution of passive particles around an active particle.

It can be clearly seen from the trajectories in Figure 76B that the passive particles get drawn in towards the active particle near the equator of the active particle (where the Pt and silica halves meet) and are repelled near the Pt cap. Figure 76C shows the probability distribution of the passive particles around

the active particles and it is clear that the passive particles predominantly get drawn in near the equator and do not make any contact at Pt cap.

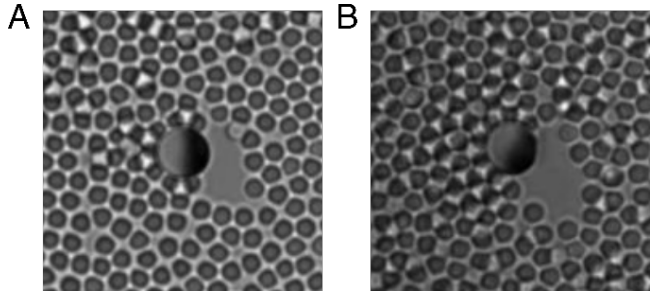

Figure 77: Depletion zones formed behind an active particle in dense suspensions of passive particles. (A) 3%H2O2, (B) 5%H2O2.

In order to ensure that an effective repulsion effect did exist on the Pt side, and our data was not simply an indication of the active particle moving away with a high velocity from the 'drawn in' passive particle, we repeat these experiments in a high density of passive particles. At high enough densities where the passive particles crystallize into a monolayer, upon addition of H_2O_2, the active particles do change their orientation from cap-down to cap-parallel but are unable to move. Very quickly we see that a depletion region forms behind the Pt cap of the active particle. The area of this depletion region fluctuates around a constant value and is dependent on the activity in the system ([H_2O_2]). Figure 77 shows snapshots of these depletion regions at two different H_2O_2 concentrations (3% and 5%).

Now, to determine the effect the orientation of the active particle has on the flows that it sets up around it, we performed experiments where the particle was fixed in a cap down orientation. Intrinsically, our active particles are bottom heavy because of the metal coating. For a metal (density ρ_m) coated particle of radius *r*, such that the cap thickness $\delta << r$, the gravitational potential difference between the cap up configuration and the cap down configuration is given by:

$$\Delta U = 2\pi r^3 \delta(\rho_m - \rho_s)g$$

For a Pt coating of δ = 10 nm and r = 2.5 μm particles, this would lead to a gravitational potential difference of several k_BT, making the cap down configuration much more likely.

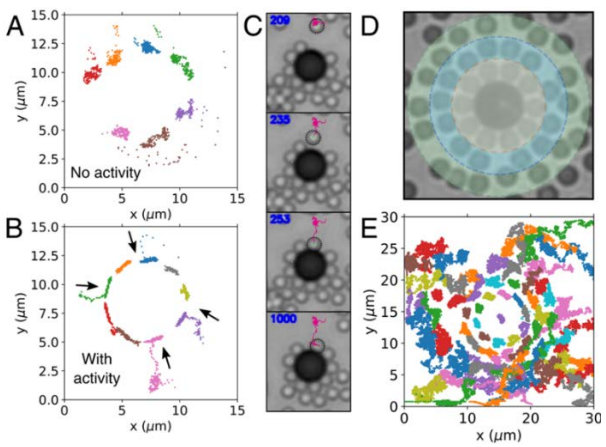

Figure 78: Interactions of passive particles with active particles in a cap-down orientation. (A) Trajectories of passive particles around silica-Pt particles without activity. (B) Trajectories of the same particles with activity. (C) Snapshots of passive particle interacting with an active particle in the cap down orientation. (D) Layers of passive particles drawn in towards the active particle. (E) Trajectories of passive

particles around an active particle. The further away the passive particles are from the active particle, higher the diffusivity.

We allow the active particles to sediment onto a glass slide and dry off the liquid through quick evaporation. During this process the active colloids get stuck to the glass surface in, presumably, the cap down orientation. We then introduce on this glass slide a suspension of passive particles in water and track the interactions. Without H_2O_2, we see that the passive particles simply diffuse around the stuck active particle (Figure 78A). Based on our previous experiments of the tracked trajectories and depletion zones in the cap-parallel configuration, we would expect the passive particles to repel away from the active particle. However as shown in Figure 78B, C, we see that the passive particles get drawn in close to the active particle and can form multiple layers around the active particle (Figure 78D). The diffusivity of the passive particles clearly gets lower the closer it is to the active particle as the attractive component of the force from the active particle restricts their motion (Figure 78E).

We do not currently fully understand these results yet, especially the seemingly different effects that the two active particle orientations cause, and our theoretical collaborators (M. Popescu, W. Uspal, MPI) are in the process of developing a theory for both the experimentally tested configurations. However, we can make the following qualitative hypothesis. Close to the active

particle near a confining surface, flows originate from a combination of hydrodynamic and phoretic effects of the active particle itself and a chemiosmotic effect along the surface set up due to the gradient in chemical composition. If the surface has the same mobility as the inert part of the active particle, as we have in our system with silica based active particles on a glass surface, the flow originating from the chemiosmotic effect is in the opposite direction as the flow generated by the particle, i.e., pointing inwards. It is plausible that the orientation of the active particle determines which of the two effects, the particles originated effects or the surface originated effects, dominate.

I must point out here that we have assumed the cap-down orientation of the particle solely from a mechanics perspective (bottom heaviness), which ignores particle surface interactions (electrostatics, van der Waal' s etc.) that could well have an effect on the configuration that the active particle settles into. In fact, if the active particle were to be in the cap-up configuration, which would look identical to Figure 78C in an optical microscope, we would not have to invoke any surface flow effects to explain the observed results. We are, at the time of writing, also in the process of acquiring direct experimental evidence for the configuration of the active particle.

5.2 Assembling colloidal crystals with active particles

After the observation of alignment effects of active particles close to topographical patterns we went on to design structures that could generate directed flows of active particles at a population level. The inherently random motion of these active particles can be rectified in the presence of local and periodic asymmetric cues given that a non-trivial interaction exists between the self-propelled particle and the cues. Since the hydrodynamic and phoretic effects introduce a strong alignment effect in our system, this can be used in conjugation with asymmetrically shaped topographical patterns to break the time reversal symmetry and direct a flow of particles. We also used this system to concentrate naturally diffusing active particles in confined spaces and identified the interactions responsible for this effect.

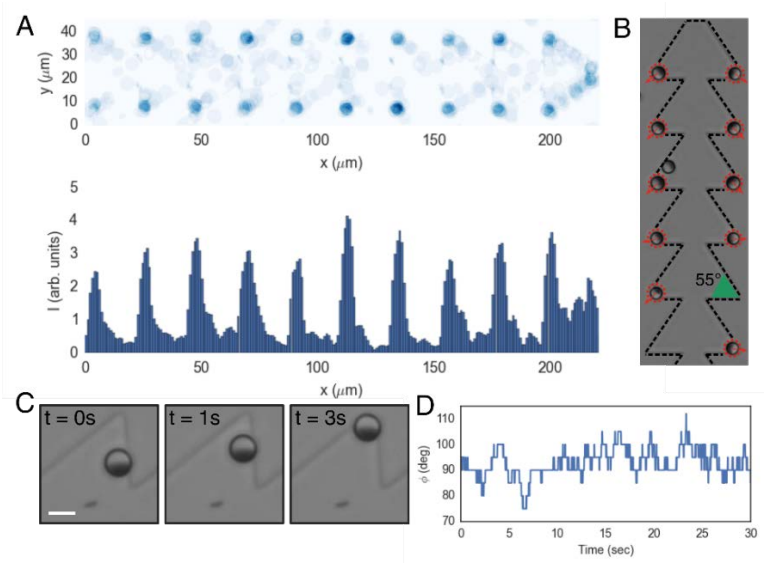

Figure 79: Towards colloidal crystals using topographical structures. (A) Probability density of active particle positions in channels with triangular structures. (B) Snapshot of active particles in triangular channels. (C) Snapshots of an active particle approaching a corner in the triangular channels. (D) Evolution of the orientation angle of the active particle in a triangle corner.

During these experiments we noticed that certain configurations of topographical patterns can lead to not only a strong angular confinement but a positional confinement as well (Figure 79A, B). V shaped structures with an acute angle between the two edges for example can trap the particles, since each edge introduces an alignment effect when the particle tries to diffuse away from the corner (Figure 79C, D). This observation can potentially be used to create surfaces which restrict colloidal particles at certain positions leading to a new way of assembling colloidal crystal structures with a finite and controllable unit lengths. To date, this is typically achieved either by tailoring particle-particle interactions, which while effective, often involves sophisticated chemistry and has limitations in the range of unit lengths that can be achieved or by creating surfaces with predefined patterns and using external pressure gradients to flow active particles over this pattern[238,239]. Our method will avoid the need to use external flows or large numbers of particles as the active particles naturally diffuse in a system and will 'seek out' the positions pre-determined for the formation of a colloidal crystal.

5.3 Engineering new responses of active particles

Finally, we studied the effect of imposing an external flow on a system of active particles[240]. For natural micro swimmers, the interplay of swimming activity and

external flow can promote robust directed motion, for example, propulsion against the direction of flow (upstream rheotaxis). These effects are generally attributed to their complex body shapes and flagellar beat patterns. In our experiments using spherical self-phoretic particles, we showed that a strong directional response can indeed arise even for simple artificial systems. We found that the particles align their propulsion axes to be nearly perpendicular to both the direction of flow and the normal vector of a nearby bounding surface leading to the cross-stream migration of active particles.

Besides our observation of directional response of active particles in flows, several studies have shown that artificial active particle can indeed respond to external gradients through purely physical mechanisms.[190,193,194,207,241] However there exist a set of responses in natural micro swimmer systems that are difficult to replicate as they necessarily involve a complex physiological process. While it is comparatively easy to introduce geometric complexity in colloidal systems that can evoke a new physical response, to be able to capture the complexity of a sensory response is rather difficult. It is because of this that convincing experiments demonstrating effects such as chemotaxis remain out of reach. How one would achieve such a response in artificial systems remains an open question.

Unlike in the case of biological active matter systems, it is possible to design new responses in the case of artificial self-propelled particles. The self-phoretic particles for example have a velocity dependent on the surface properties of the colloidal particle. By modifying the surface of the particle, it is possible to change its propulsion behavior and therefore its response to external fields. Using a different set of parameters for catalytic coverages and surface mobilities, it has been shown that these particles can show rheotaxis in an imposed flow as opposed to the cross-stream migration that we observe[223]. It should also be possible to engineer new responses of active by combining different interactions, for example to flow and to topographical patterns. By carefully designing the ratchet structures that we have used in Chapter 3, and directing them against the flow direction, active particles could be caused to migrate against the flow direction at moderate flow rates.

Overall artificial active matter systems display an ability to respond to external fields and gradients much like their biological counterparts but owing the versatility in modifying their physical properties could allow for us to engineer an even range of directional responses than exist in biological systems

5.4 Beyond solid interfaces

Apart from solid interfaces, it is also interesting to consider the effects of liquid interfaces where several additional effects are likely to come into play[242,243]. The angular confinement that we observe close to solid surfaces originates

from to the accumulation of the chemical product between the catalytic cap and the solid surface. Close to a liquid interface, the chemical product can diffuse into the adjacent medium and affect the angular response of the active particles. Furthermore, capillary effects and Marangoni flows also come into play close to liquid interfaces potentially offering a rich system to be studied experimentally. This system is the primary focus in the PhD work of Lucas Palacios.

6.Resumen en español

Los organismos y sistemas vivos convierten energía almacenada internamente o derivada de sus alrededores en movimiento de forma continua. Esta actividad puede causar una constante auto-propulsión que lleva a estos sistemas a un estado fuera de equilibrio térmico. Gracias a esto, aparecen un gran número de fenómenos exóticos que no son accesibles para un sistema que se encuentra en equilibrio térmico. En los últimos años se ha clasificado a estos sistemas de no equilibro como "*material activa*". La materia activa, por definición, incluye los sistemas compuestos de *unidades activas*, cada una de ellas capaz de convertir la energía almacenada o del entorno en movimiento sistemático. Existen varios ejemplos que van desde la escala sub-micrométrica, donde podemos encontrar a los microtúbulos asociados a proteínas motoras en el citoplasma, a las grandes escalas, donde se encuentran sistemas más familiares como peces o pájaros, pasando por la escala micrométrica, donde nadan las bacterias.

Podemos diferenciar dos temas principales que se manifiestan en todos estos sistemas de materia activa. El primero es la aparición de fenómenos colectivos correlacionados a través de interacciones partícula-partícula, como ocurre en bandadas de pájaros, enjambres bacterianos y la cristalización de partículas auto-propulsadas. El segundo es la capacidad de estas unidades activas de

interaccionar con sus alrededores a través del fenómeno de la auto-propulsión, por ejemplo, a través de quimiotaxia o reotaxia, como se puede observar en muchos sistemas biológicos y que ya han sido reportados en varios estudios. En esta tesis, me he enfocado en el estudio de este último tema principal: la interacción de partículas activas con su entorno local.

Como modelo de sistema de materia activa, usamos partículas activas coloidales que se propulsan gracias al fenómeno de auto-difusoforesis. Estas partículas están recubiertas por dos materiales diferentes en cada unas de sus caras, y son comúnmente llamadas "partículas Janus". Una de sus caras está recubierta de un material que reacciona con H_2O_2 de forma catalítica (Pt), mientras que la otra cara está recubierta de un material inerte (SiO_2). En una solución de H_2O_2, la reacción que ocurre en la parte catalítica produce un gradiente de concentración de producto a lo largo de la superficie de la partícula e induce un deslizamiento forético que la propulsa. Nuestros experimentos incluyen el estudio de la dinámica de estas partículas auto-propulsadas cerca de superficies y las siguientes secciones resumen los resultados principales obtenidos durante la tesis.

1. Caminos topológicos guían a los micro-motores químicos

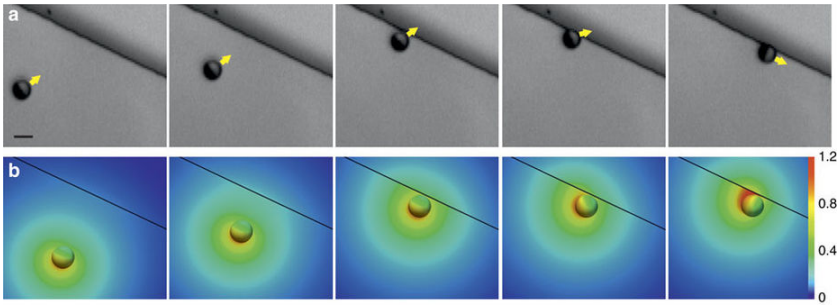

Figura 1: (A) Una partícula activa Janus acercándose a un escalón. Después de entrar en contacto con éste, se reorienta hasta que su eje de propulsión es paralelo al escalón. R=2.5 μm, h_{step}=800 nm, 2.5%vol. H_2O_2. (B) Cálculo numérico de la distribución de productos de reacción c(r) en estado estacionario alrededor de la esfera Janus, con una cara recubierta de material catalítico, en función de la distancia al escalón y su orientación con respecto a éste. El mapa de color muestra c(**r**) en la superficie de la partícula. c(**r**) tiene unidades de c∞. Escala, 5μm.

Nuestro principal interés residía en el estudio de las interacciones de estas partículas con superficies cercanas. Se ha observado en un número de sistemas biológicos de materia activa que las superficies producen un efecto de acumulación. Éste puede surgir debido a efectos de mecánica estadística (las partículas auto-propulsadas tienen una velocidad menor cuando se encuentran cerca de una superficie en comparación con el volumen de la solución, aumentando así su función de densidad de probabilidad cerca de la superficie) o debido a interacciones activas que ocurren, por ejemplo, a causa de efectos hidrodinámicos que restringen los grados de libertad de orientación cerca de una superficie y "atrapa" las partículas ahí.

En nuestros experimentos, encontramos que los efectos hidrodinámicos y foréticos se unen para restringir fuertemente la orientación de las partículas

de forma paralela a la superficie, atrapándolas ahí. Con esto, conseguimos demostrar que los efectos de acumulación causados por paredes, que existen en muchos sistemas biológicos de materia activa, también se pueden encontrar en sistemas artificiales y, además, estos efectos son incluso más fuertes debido a los efectos de alineación ya comentados.

Aprovechamos este efecto de alineamiento para crear un sistema de guía para partículas Janus auto-propulsadas, consiguiendo ganar control sobre la direccionalidad de los coloides, algo esencial para sus aplicaciones prácticas como transportadores de cargas en dispositivos de microfluídica. Hasta ese momento, la dirección de coloides Janus esféricos se obtenía principalmente usando recubrimientos multi-capa magnéticos, creados especialmente para ese fin, combinados con campos magnéticos. Demostramos que se podían añadir pequeños escalones sub-micrométricos que actuaran como guías topográficas que podían ser usadas como zonas de almacenamiento y plataformas de dirección para coloides Janus esféricos. Para varias estructuras topográficas, el ensamblaje de coloides al borde el escalón era robusto y fidedigno. Además, los coloides se movían a lo largo de los bordes durante tiempos significativamente mayores, lo cual aumentaba de forma sistemática con la concentración del combustible. Este fenómeno fue capturado de forma cualitativa a través de un modelo físico continúo basado en auto-difusoforesis cerca de fronteras confinantes, indicando que las principales causas de este

comportamiento experimental yacían en la actividad química e interacciones hidrodinámicas asociadas con la topografía cercana.

Simmchen, J.; Katuri, J.; Uspal, W. E.; Popescu, M. N.; Tasinkevych, M.; Sánchez, S. Topographical Pathways Guide Chemical Microswimmers. Nat. Commun. **2016**, 7, 10598.

2. Flujo direccionado de micro-motores a través de interacciones alineadas con trinquetes micro-estampados

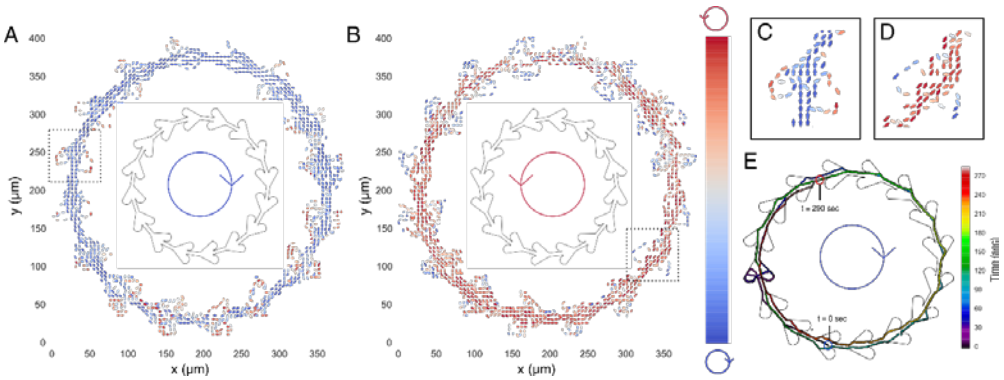

Figura 2: Flujo circular de micro-motores dentro de una estructura periódica de tipo trinquete. (A-B) Mapas de velocidad obtenidos al rastrear micro-motores (n=100; N=6) dentro de las estructuras asimétricas diseñadas para generar flujos en sentido horario y antihorario. La barra de color a la derecha indica la vorticidad. (C-D) Imagen ampliada de celdas individuales marcadas por los recuadros puntuados en A, B. (E) Ejemplo de trayectoria de un micro-motor durante t = 290 s dentro de la estructura asimétrica. La barra de color a derecha indica el paso del tiempo.

Uno de los mayores desafíos en física de la materia activa es obtener control sobre sistemas difusivos fuera de equilibrio compuestos de partículas auto-propulsadas, como células o coloides auto-foréticos. El movimiento aleatorio inherente en estas partículas activas puede ser rectificado en presencia de señales asimétricas periódicas que dan lugar a interacciones no triviales entre las partículas auto-propulsadas y tales señales. En este estudio, aprovechamos las interacciones foréticas e hidrodinámicas entre micro-motores sintéticos y señales topográficas para romper la simetría de inversión de tiempo en las trayectorias de las partículas y, finalmente, dirigir un flujo de micro-motores a

nivel macroscópico. Mostramos que el alineamiento direccional inducido por las señales topográficas, junto con la asimetría geométrica, son cruciales para generar un flujo de partículas. En particular, tomamos en consideración este efecto de alineación para diseñar señales topográficas asimétricas que generaran flujos de partículas específicos. Igualmente, demostramos que nuestro sistema podía ser usado para concentrar micro-motores en espacios confinados e identificamos las interacciones responsables de este efecto. Finalmente, desarrollamos un modelo mínimo que identificaba los principales parámetros involucrados en esta rectificación observada experimentalmente.

Katuri, J.; Caballero, D.; Voituriez, R.; Samitier, J.; Sánchez, S. Directed flow of micromotors through alignment interactions with micropatterned ratchets, ACS Nano, 2018 (under revision)

3. Flujo cruzado migratorio de partículas activas

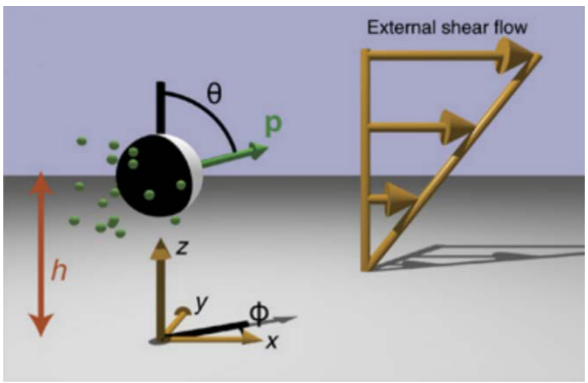

Figura 3: Una partícula (esfera blanca) con un recubrimiento asimétrico de un material catalítico (parte negra) es llevada por un flujo cortante externo (flechas doradas) en la dirección $\hat{x}$ cerca de un muro plano (gris). La partícula está suspendida a una altura h sobre el muro y con un vector de orientación **p**, que se puede especificar por los ángulos

θ and φ. Cuando la partícula está activa, la parte catalítica emite moléculas de soluto (esferas verdes).

Para micro-nadadores naturales, la interacción entre su actividad y un flujo externo puede causar un movimiento direccionado robusto, como ocurre por ejemplo con la propulsión contra (reotaxis a contracorriente) o perpendicular a la dirección del flujo. Estos efectos generalmente se atribuyen a las formas complejas de sus cuerpos y a los patrones de movimiento flagelar. Usando partículas Janus catalíticas como sistema modelo, observamos una fuerte respuesta direccional en partículas activas esféricas en un micro-canal con flujo. Las partículas alinean sus ejes de propulsión de forma casi perpendicular tanto a la dirección del flujo como al vector normal de una superficie cercana. Por tanto, desarrollamos un modelo teórico determinista de micro-nadadores esféricos cerca de una superficie plana que capturara las observaciones experimentales. Gracias a este modelo, demostramos que la respuesta direccional emerge de la interacción entre el flujo cortante y la actividad propulsiva cerca de la superficie. Finalmente, añadiendo efectos de ruido térmico, obtuvimos distribuciones de orientación que coincidían de forma semi-cuantitativa con las distribuciones experimentales.

Katuri, J.; Uspal, W. E.; Simmchen, J.; Miguel-López, A.; Sánchez, S. Cross-Stream Migration of Active Particles. Sci. Adv. **2018**, 4 (1), eaao1755.

Conclusiones

En esta tesis, me he enfocado en el estudio de la dinámica de partículas activas auto-foréticas cerca de superficies. Hemos demostrado que las partículas esféricas auto-foréticas, al igual que los micro-nadadores biológicos, muestran una fuerte tendencia a acumularse cerca de superficies. Este efecto se origina de las modificaciones de los campos hidrodinámicos y foréticos creadas por estas partículas auto-propulsadas cerca de superficies. Los momentos de fuerza que surgen de las interacciones con la superficie contrarrestan las rotaciones debidas a fluctuaciones térmicas que intentan alejar a las partículas de su orientación estable. Aprovechamos esta tendencia de las partículas activas de adquirir una orientación estable para demostrar sistemas de guía para partículas auto-propulsadas gracias a la introducción de patrones topográficos. Igualmente, usamos estas observaciones para diseñar estructuras que podían generar flujos direccionados de partículas activas a nivel de población. El movimiento estocástico inherente de estas partículas podía ser rectificado en presencia de señales asimétricas locales y periódicas debido a la interacción no trivial que existe entre las partículas auto-propulsadas y las superficies. Finalmente, estudiamos el efecto de imponer un flujo externo en un sistema de partículas activas. En nuestros experimentos usando partículas esféricas auto-foréticas, mostramos la posibilidad de crear una respuesta robusta y direccional incluso en sistemas artificiales carentes de la complejidad fisiológica de los micro-nadadores naturales. Encontramos que las partículas alinean su eje de propulsión hasta ser casi perpendicular tanto a la dirección del flujo como al vector normal de una superficie cercana, dando

lugar a una migración cruzada de partículas activas. En general, estos resultados mejoran nuestro conocimiento sobre los efectos inducidos por superficies en sistemas de materia activa y abre nuevas posibilidades para su aplicación en dispositivos de microfluídica.

7.References

1. Ramaswamy, S. The Mechanics and Statistics of Active Matter. *Annu. Rev. Condens. Matter Phys.* **1,** 323–345 (2010).

2. Fletcher, D. A. & Geissler, P. L. Active Biological Materials. *Annu. Rev. Phys. Chem.* **60,** 469–486 (2009).

3. MacKintosh, F. C. & Schmidt, C. F. Active cellular materials. *Curr. Opin. Cell Biol.* **22,** 29–35 (2010).

4. Czirók, A., Ben-Jacob, E., Cohen, I. & Vicsek, T. Formation of complex bacterial colonies via self-generated vortices. *Phys. Rev. E* **54,** 1791–1801 (1996).

5. Dombrowski, C., Cisneros, L., Chatkaew, S., Goldstein, R. E. & Kessler, J. O. Self-Concentration and Large-Scale Coherence in Bacterial Dynamics. *Phys. Rev. Lett.* **93,** 098103 (2004).

6. Sokolov, A., Aranson, I. S., Kessler, J. O. & Goldstein, R. E. Concentration Dependence of the Collective Dynamics of Swimming Bacteria. *Phys. Rev. Lett.* **98,** 158102 (2007).

7. Becco, C., Vandewalle, N., Delcourt, J. & Poncin, P. Experimental evidences of a structural and dynamical transition in fish school. *Phys. Stat. Mech. Its Appl.* **367,** 487–493 (2006).

8. Partridge, B. L. The Structure and Function of Fish Schools. *Sci. Am.* **246,** 114–123 (1982).

9. Cambuí, D. S. & Rosas, A. Density induced transition in a school of fish. *Phys. Stat. Mech. Its Appl.* **391,** 3908–3914 (2012).

10. Emlen, J. T. Flocking Behavior in Birds. *The Auk* **69,** 160–170 (1952).

11. Potts, W. K. The chorus-line hypothesis of manoeuvre coordination in avian flocks. *Nature* **309,** 344–345 (1984).

12. Ballerini, M. *et al.* Interaction ruling animal collective behavior depends on topological rather than metric distance: Evidence from a field study. *Proc. Natl. Acad. Sci.* **105,** 1232–1237 (2008).

13. AOKI, I. A Simulation Study on the Schooling Mechanism in Fish. *NIPPON SUISAN GAKKAISHI* **48,** 1081–1088 (1982).

14. Huth, A. & Wissel, C. The simulation of the movement of fish schools. *J. Theor. Biol.* **156,** 365–385 (1992).

15. Couzin, I. D., Krause, J., James, R., Ruxton, G. D. & Franks, N. R. Collective Memory and Spatial Sorting in Animal Groups. *J. Theor. Biol.* **218,** 1–11 (2002).

16. Inada, Y. & Kawachi, K. Order and Flexibility in the Motion of Fish Schools. *J. Theor. Biol.* **214,** 371–387 (2002).

17. Kunz, H. & Hemelrijk, C. K. Artificial Fish Schools: Collective Effects of School Size, Body Size, and Body Form. *Artif. Life* **9,** 237–253 (2003).

18. Vicsek, T., Czirók, A., Ben-Jacob, E., Cohen, I. & Shochet, O. Novel Type of Phase Transition in a System of Self-Driven Particles. *Phys. Rev. Lett.* **75,** 1226–1229 (1995).

19. Czirók, A., Barabási, A.-L. & Vicsek, T. Collective Motion of Self-Propelled Particles: Kinetic Phase Transition in One Dimension. *Phys. Rev. Lett.* **82,** 209–212 (1999).

20. Grégoire, G., Chaté, H. & Tu, Y. Moving and staying together without a leader. *Phys. Nonlinear Phenom.* **181,** 157–170 (2003).

21. Grégoire, G. & Chaté, H. Onset of Collective and Cohesive Motion. *Phys. Rev. Lett.* **92,** 025702 (2004).

22. Buhl, J. *et al.* From Disorder to Order in Marching Locusts. *Science* **312,** 1402–1406 (2006).

23. College, O. Wikimedia: Large fish school [https://commons.wikimedia.org/wiki/File:Large_fish_school.png]. (2011).

24. Aranson, I. Viewpoint: The Aquatic Dance of Bacteria. *Physics* **6,** (2013).

25. Angelini, T. E. *et al.* Glass-like dynamics of collective cell migration. *Proc. Natl. Acad. Sci.* **108,** 4714–4719 (2011).

26. Ganguly, S., Williams, L. S., Palacios, I. M. & Goldstein, R. E. Cytoplasmic streaming in Drosophila oocytes varies with kinesin activity and correlates with the microtubule cytoskeleton architecture. *Proc. Natl. Acad. Sci.* **109,** 15109–15114 (2012).

27. Keber, F. C. *et al.* Topology and dynamics of active nematic vesicles. *Science* **345,** 1135–1139 (2014).

28. *Intracellular Transport*. (Elsevier, 1966). doi:10.1016/C2013-0-07957-1

29. Poujade, M. *et al.* Collective migration of an epithelial monolayer in response to a model wound. *Proc. Natl. Acad. Sci.* **104,** 15988–15993 (2007).

30. Martin, P. & Parkhurst, S. M. Parallels between tissue repair and embryo morphogenesis. *Development* **131,** 3021–3034 (2004).

31. Lecaudey, V. & Gilmour, D. Organizing moving groups during morphogenesis. *Curr. Opin. Cell Biol.* **18,** 102–107 (2006).

32. Friedl, P. & Wolf, K. Tumour-cell invasion and migration: diversity and escape mechanisms. *Nat. Rev. Cancer* **3,** 362–374 (2003).

33. Riedel, I. H., Kruse, K. & Howard, J. A Self-Organized Vortex Array of Hydrodynamically Entrained Sperm Cells. *Science* **309,** 300–303 (2005).

34. Vicsek, T. & Zafeiris, A. Collective motion. *Phys. Rep.* **517,** 71–140 (2012).

35. Ginelli, F. The Physics of the Vicsek model. *Eur. Phys. J. Spec. Top.* **225,** 2099–2117 (2016).

36. Chaté, H., Ginelli, F., Grégoire, G. & Raynaud, F. Collective motion of self-propelled particles interacting without cohesion. *Phys. Rev. E* **77,** 046113 (2008).

37. Giomi, L., Hawley-Weld, N. & Mahadevan, L. Swarming, swirling and stasis in sequestered bristle-bots. *Proc R Soc A* **469,** 20120637 (2013).

38. Kumar, N., Soni, H., Ramaswamy, S. & Sood, A. K. Flocking at a distance in active granular matter. *Nat. Commun.* **5,** 4688 (2014).

39. Thutupalli, S., Seemann, R. & Herminghaus, S. Swarming behavior of simple model squirmers. *New J. Phys.* **13,** 073021 (2011).

40. Bricard, A., Caussin, J.-B., Desreumaux, N., Dauchot, O. & Bartolo, D. Emergence of macroscopic directed motion in populations of motile colloids. *Nature* **503,** 95–98 (2013).

41. Sanchez, T., Chen, D. T. N., DeCamp, S. J., Heymann, M. & Dogic, Z. Spontaneous motion in hierarchically assembled active matter. *Nature* **491,** 431–434 (2012).

42. Palacci, J., Sacanna, S., Steinberg, A. P., Pine, D. J. & Chaikin, P. M. Living Crystals of Light-Activated Colloidal Surfers. *Science* **339,** 936–940 (2013).

43. Buttinoni, I. *et al.* Dynamical Clustering and Phase Separation in Suspensions of Self-Propelled Colloidal Particles. *Phys. Rev. Lett.* **110,** 238301 (2013).

44. Theurkauff, I., Cottin-Bizonne, C., Palacci, J., Ybert, C. & Bocquet, L. Dynamic Clustering in Active Colloidal Suspensions with Chemical Signaling. *Phys. Rev. Lett.* **108,** 268303 (2012).

45. Singh, D. P., Choudhury, U., Fischer, P. & Mark, A. G. Non-Equilibrium Assembly of Light-Activated Colloidal Mixtures. *Adv. Mater.* **29,** n/a-n/a (2017).

46. Ginot, F., Theurkauff, I., Detcheverry, F., Ybert, C. & Cottin-Bizonne, C. Aggregation-fragmentation and individual dynamics of active clusters. *Nat. Commun.* **9,** 696 (2018).

47. Elgeti, J. & Gompper, G. Microswimmers near surfaces. *Eur. Phys. J. Spec. Top.* **225,** 2333–2352 (2016).

48. O' Toole, G. A. & Kolter, R. Flagellar and twitching motility are necessary for Pseudomonas aeruginosa biofilm development. *Mol. Microbiol.* **30,** 295–304

49. Donlan, R. M. Biofilms: Microbial Life on Surfaces. *Emerg. Infect. Dis.* **8,** 881–890 (2002).

50. Yanagimachi, R. *et al.* Sperm Attractant in the Micropyle Region of Fish and Insect Eggs. *Biol. Reprod.* **88,** (2013).

51. Miki, K. & Clapham, D. E. Rheotaxis Guides Mammalian Sperm. *Curr. Biol.* **23,** 443–452 (2013).

52. Rothschild. Non-random Distribution of Bull Spermatozoa in a Drop of Sperm Suspension. *Nature* **198,** 1221–1222 (1963).

53. Li, G. & Tang, J. X. Accumulation of Microswimmers near a Surface Mediated by Collision and Rotational Brownian Motion. *Phys. Rev. Lett.* **103,** 078101 (2009).

54. Frymier, P. D., Ford, R. M., Berg, H. C. & Cummings, P. T. Three-dimensional tracking of motile bacteria near a solid planar surface. *Proc. Natl. Acad. Sci.* **92,** 6195–6199 (1995).

55. Berke, A. P., Turner, L., Berg, H. C. & Lauga, E. Hydrodynamic Attraction of Swimming Microorganisms by Surfaces. *Phys. Rev. Lett.* **101,** 038102 (2008).

56. Li, G. *et al.* Accumulation of swimming bacteria near a solid surface. *Phys. Rev. E* **84,** 041932 (2011).

57. Elgeti, J. & Gompper, G. Self-propelled rods near surfaces. *EPL Europhys. Lett.* **85,** 38002 (2009).

58. Marx, K. Self-propelled rod-like swimmers near surfaces. (Universität zu Köln, 2011).

59. Lauga, E. & Powers, T. R. The hydrodynamics of swimming microorganisms. *Rep. Prog. Phys.* **72,** 096601 (2009).

60. Drescher, K., Dunkel, J., Cisneros, L. H., Ganguly, S. & Goldstein, R. E. Fluid dynamics and noise in bacterial cell–cell and cell–surface scattering. *Proc. Natl. Acad. Sci.* **108,** 10940–10945 (2011).

61. Harris, E. H. The Chlamydomonas Sourcebook: Introduction to Chlamydomonas and Its Laboratory Use. (Academic Press, 2009).

62. Polin, M., Tuval, I., Drescher, K., Gollub, J. P. & Goldstein, R. E. Chlamydomonas Swims with Two "Gears" in a Eukaryotic Version of Run-and-Tumble Locomotion. *Science* **325,** 487–490 (2009).

63. Elgeti, J., Winkler, R. G. & Gompper, G. Physics of microswimmers—single particle motion and collective behavior: a review. *Rep. Prog. Phys.* **78,** 056601 (2015).

64. Spagnolie, S. E., Moreno-Flores, G. R., Bartolo, D. & Lauga, E. Geometric capture and escape of a microswimmer colliding with an obstacle. *Soft Matter* **11,** 3396–3411 (2015).

65. Takagi, D., Palacci, J., Braunschweig, A. B., Shelley, M. J. & Zhang, J. Hydrodynamic capture of microswimmers into sphere-bound orbits. *Soft Matter* **10,** 1784–1789 (2014).

66. Peng, C., Turiv, T., Guo, Y., Wei, Q.-H. & Lavrentovich, O. D. Command of active matter by topological defects and patterns. *Science* **354,** 882–885 (2016).

67. Guillamat, P., Ignés-Mullol, J. & Sagués, F. Control of active liquid crystals with a magnetic field. *Proc. Natl. Acad. Sci.* **113,** 5498–5502 (2016).

68. Einstein, A. Investigations on the Theory of the Brownian Movement. (Dover Publications, 1956).

69. Purcell, E. M. Life at low Reynolds number. *Am. J. Phys.* **45,** 3–11 (1977).

70. L.Vector:Urutseg, O. Wikimedia: Flagellum - beating pattern of flagellum and cilia [https://commons.wikimedia.org/wiki/File:Flagellum-beating.svg]. (2011).

71. AJC1. E. coli with flagella. (2013).

72. Strain, D. & Writer459-2495, G. Cholera bacteria show adaptability to changing environments. *UC Santa Cruz News* Available at: https://news.ucsc.edu/2009/12/3429.html. (Accessed: 31st May 2018)

73. Algae 'breaststroke' is synchronized from within. *Physics World* (2015). Available at: https://physicsworld.com/a/algae-breaststroke-is-synchronized-from-within/. (Accessed: 31st May 2018)

74. Wikipedia, B. at the E. Wikimedia: Paramecium [https://commons.wikimedia.org/wiki/File:Paramecium.jpg?uselang=en-gb]. (2003).

75. Dreyfus, R. *et al.* Microscopic artificial swimmers. *Nature* **437,** 862–865 (2005).

76. Williams, B. J., Anand, S. V., Rajagopalan, J. & Saif, M. T. A. A self-propelled biohybrid swimmer at low Reynolds number. *Nat. Commun.* **5,** 3081 (2014).

77. Zhang, L. *et al.* Characterizing the Swimming Properties of Artificial Bacterial Flagella. *Nano Lett.* **9,** 3663–3667 (2009).

78. Ghosh, A. & Fischer, P. Controlled Propulsion of Artificial Magnetic Nanostructured Propellers. *Nano Lett.* **9,** 2243–2245 (2009).

79. Tottori, S. *et al.* Magnetic Helical Micromachines: Fabrication, Controlled Swimming, and Cargo Transport. *Adv. Mater.* **24,** 811–816 (2012).

80. Anderson, J. L. Colloid Transport by Interfacial Forces. *Annu. Rev. Fluid Mech.* **21,** 61–99 (1989).

81. Palacci, J. Manipulation of Colloids by Osmotic Forces. (Université Claude Bernard - Lyon I, 2010).

82. Tiselius, A. A new apparatus for electrophoretic analysis of colloidal mixtures. *Trans. Faraday Soc.* **33,** 524–531 (1937).

83. Hunter, R. J., Ottewill, R. H. & Rowell, R. L. *Zeta Potential in Colloid Science: Principles and Applications*. (Elsevier Science, 2013).

84. Hiemenz, P. C. Principles of colloid and surface chemistry. (M. Dekker, 1986).

85. Morrison, F. A. Electrophoresis of a particle of arbitrary shape. *J. Colloid Interface Sci.* **34,** 210–214 (1970).

86. Poon, W. C. K. From Clarkia to Escherichia and Janus: the physics of natural and synthetic active colloids. *ArXiv13064799 Cond-Mat Physicsphysics Q-Bio* (2013).

87. Anderson, J. L. & Prieve, D. C. Diffusiophoresis: Migration of Colloidal Particles in Gradients of Solute Concentration. *Sep. Purif. Methods* **13,** 67–103 (1984).

88. Abécassis, B., Cottin-Bizonne, C., Ybert, C., Ajdari, A. & Bocquet, L. Boosting migration of large particles by solute contrasts. *Nat. Mater.* **7,** 785–789 (2008).

89. Golestanian, R., Liverpool, T. B. & Ajdari, A. Propulsion of a molecular machine by asymmetric distribution of reaction products. *Phys. Rev. Lett.* **94,** 220801–220801 (2005).

90. Shan, J. *et al.* Janus Particle Synthesis and Assembly. *Adv. Mater.* **22,** 1060–1071

91. Hong, L., Jiang, S. & Granick, S. Simple Method to Produce Janus Colloidal Particles in Large Quantity. *Langmuir* **22,** 9495–9499 (2006).

92. Ebbens, S., Tu, M.-H., Howse, J. R. & Golestanian, R. Size dependence of the propulsion velocity for catalytic Janus-sphere swimmers. *Phys. Rev. E* **85,** 020401 (2012).

93. Paxton, W. F. *et al.* Catalytic Nanomotors: Autonomous Movement of Striped Nanorods. *J. Am. Chem. Soc.* **126,** 13424–13431 (2004).

94. Palacci, J. *et al.* Light-activated self-propelled colloids. *Phil Trans R Soc A* **372,** 20130372 (2014).

95. Volpe, G., Buttinoni, I., Vogt, D., Kümmerer, H.-J. & Bechinger, C. Microswimmers in patterned environments. *Soft Matter* **7,** 8810–8815 (2011).

96. Buttinoni, I., Volpe, G., Kümmel, F., Volpe, G. & Bechinger, C. Active Brownian motion tunable by light. *J. Phys. Condens. Matter* **24,** 284129 (2012).

97. Ma, X., Hortelão, A. C., Patiño, T. & Sánchez, S. Enzyme Catalysis To Power Micro/Nanomachines. *ACS Nano* **10,** 9111–9122 (2016).

98. Moran, J. L. & Posner, J. D. Phoretic Self-Propulsion. *Annu. Rev. Fluid Mech.* **49,** 511–540 (2017).

99. Ma, X. *et al.* Enzyme-Powered Hollow Mesoporous Janus Nanomotors. *Nano Lett.* **15,** 7043–7050 (2015).

100. Sánchez, S., Soler, L. & Katuri, J. Chemically Powered Micro- and Nanomotors. *Angew. Chem. Int. Ed.* **54,** 1414–1444 (2015).

101. Wang, W., Duan, W., Ahmed, S., Mallouk, T. E. & Sen, A. Small power: Autonomous nano- and micromotors propelled by self-generated gradients. *Nano Today* **8,** 531–554 (2013).

102. Aubret, A., Ramananarivo, S. & Palacci, J. Eppur si muove, and yet it moves: Patchy (phoretic) swimmers. *Curr. Opin. Colloid Interface Sci.* **30,** 81–89 (2017).

103. Bechinger, C. *et al.* Active Particles in Complex and Crowded Environments. *Rev. Mod. Phys.* **88,** (2016).

104. Howse, J. R. *et al.* Self-Motile Colloidal Particles: From Directed Propulsion to Random Walk. *Phys. Rev. Lett.* **99,** 048102 (2007).

105. Elgeti, J. & Gompper, G. Microswimmers near surfaces. *Eur. Phys. J. Spec. Top.* **225,** 2333–2352 (2016).

106. Pratt, L. A. & Kolter, R. Genetic analysis of Escherichia coli biofilm formation: roles of flagella, motility, chemotaxis and type I pili. *Mol. Microbiol.* **30,** 285–293 (1998).

107. Quill, T. A. *et al.* Hyperactivated sperm motility driven by CatSper2 is required for fertilization. *Proc. Natl. Acad. Sci. U. S. A.* **100,** 14869–14874 (2003).

108. Li, G. & Tang, J. X. Accumulation of microswimmers near a surface mediated by collision and rotational Brownian motion. *Phys. Rev. Lett.* **103,** 078101 (2009).

109. Kantsler, V., Dunkel, J., Polin, M. & Goldstein, R. E. Ciliary contact interactions dominate surface scattering of swimming eukaryotes. *Proc. Natl. Acad. Sci. U. S. A.* **110,** 1187–1192 (2013).

110. Schaar, K., Zöttl, A. & Stark, H. Detention Times of Microswimmers Close to Surfaces: Influence of Hydrodynamic Interactions and Noise. *Phys. Rev. Lett.* **115,** 038101 (2015).

111. Drescher, K., Dunkel, J., Cisneros, L. H., Ganguly, S. & Goldstein, R. E. Fluid dynamics and noise in bacterial cell-cell and cell-surface scattering. *Proc. Natl. Acad. Sci. U. S. A.* **108,** 10940–10945 (2011).

112. Berke, A. P., Turner, L., Berg, H. C. & Lauga, E. Hydrodynamic attraction of swimming microorganisms by surfaces. *Phys. Rev. Lett.* **101,** 038102 (2008).

113. Spagnolie, S. E. & Lauga, E. Hydrodynamics of self-propulsion near a boundary: predictions and accuracy of far-field approximations. *J. Fluid Mech.* **700,** 105–147 (2012).

114. Contino, M., Lushi, E., Tuval, I., Kantsler, V. & Polin, M. Microalgae Scatter off Solid Surfaces by Hydrodynamic and Contact Forces. *Phys. Rev. Lett.* **115,** 258102 (2015).

115. Spagnolie, S. E., Moreno-Flores, G. R., Bartolo, D. & Lauga, E. Geometric capture and escape of a microswimmer colliding with an obstacle. *Soft Matter* **11,** 3396–3411 (2015).

116. Leonardo, R. D. *et al.* Bacterial ratchet motors. *Proc. Natl. Acad. Sci.* **107,** 9541–9545 (2010).

117. Rothschild. Non-random Distribution of Bull Spermatozoa in a Drop of Sperm Suspension. *Nature* **198,** 1221–1222 (1963).

118. Lauga, E., DiLuzio, W. R., Whitesides, G. M. & Stone, H. A. Swimming in Circles: Motion of Bacteria near Solid Boundaries. *Biophys. J.* **90,** 400–412 (2006).

119. DiLuzio, W. R. *et al. Escherichia coli* swim on the right-hand side. *Nature* **435,** 1271–1274 (2005).

120. Elgeti, J. & Gompper, G. Run-and-tumble dynamics of self-propelled particles in confinement. *EPL Europhys. Lett.* **109,** 58003 (2015).

121. Ezhilan, B., Alonso-Matilla, R. & Saintillan, D. On the distribution and swim pressure of run-and-tumble particles in confinement. *J. Fluid Mech.* **781,** (2015).

122. Sipos, O., Nagy, K., Di Leonardo, R. & Galajda, P. Hydrodynamic Trapping of Swimming Bacteria by Convex Walls. *Phys. Rev. Lett.* **114,** 258104 (2015).

123. Bianchi, S., Saglimbeni, F. & Di Leonardo, R. Holographic Imaging Reveals the Mechanism of Wall Entrapment in Swimming Bacteria. *Phys. Rev. X* **7,** 011010 (2017).

124. Uspal, W. E., Popescu, M. N., Dietrich, S. & Tasinkevych, M. Self-propulsion of a catalytically active particle near a planar wall: from reflection to sliding and hovering. *Soft Matter* **11,** 434–438 (2014).

125. Simmchen, J. *et al.* Topographical pathways guide chemical microswimmers. *Nat. Commun.* **7,** 10598 (2016).

126. Das, S. *et al.* Boundaries can steer active Janus spheres. *Nat. Commun.* **6,** 8999 (2015).

127. Wang, W., Duan, W., Ahmed, S., Mallouk, T. E. & Sen, A. Small power: Autonomous nano- and micromotors propelled by self-generated gradients. *Nano Today* **8,** 531–554 (2013).

128. Sánchez, S., Soler, L. & Katuri, J. Chemically Powered Micro- and Nanomotors. *Angew. Chem. Int. Ed.* **54,** 1414–1444 (2015).

129. Guix, M., Mayorga-Martinez, C. C. & Merkoçi, A. Nano/Micromotors in (Bio)chemical Science Applications. *Chem. Rev.* **114,** 6285–6322 (2014).

130. Wang, J. Nanomachines: Fundamentals and Applications. (Wiley, 2013).

131. Gao, W. & Wang, J. The Environmental Impact of Micro/Nanomachines: A Review. *ACS Nano* **8,** 3170–3180 (2014).

132. Soler, L. & Sánchez, S. Catalytic nanomotors for environmental monitoring and water remediation. *Nanoscale* **6,** 7175–7182 (2014).

133. Moo, J. G. S. & Pumera, M. Chemical Energy Powered Nano/Micro/Macromotors and the Environment. *Chem. – Eur. J.* **21,** 58–72 (2015).

134. Baraban, L. *et al.* Transport of cargo by catalytic Janus micro-motors. *Soft Matter* **8,** 48–52 (2011).

135. Baylis, J. R. *et al.* Self-propelled particles that transport cargo through flowing blood and halt hemorrhage. *Sci. Adv.* **1,** e1500379 (2015).

136. Sundararajan, S., Lammert, P. E., Zudans, A. W., Crespi, V. H. & Sen, A. Catalytic Motors for Transport of Colloidal Cargo. *Nano Lett.* **8,** 1271–1276 (2008).

137. Esteban-Fernández de Ávila, B. *et al.* Acoustically Propelled Nanomotors for Intracellular siRNA Delivery. *ACS Nano* **10,** 4997–5005 (2016).

138. Ma, X., Hahn, K. & Sanchez, S. Catalytic Mesoporous Janus Nanomotors for Active Cargo Delivery. *J. Am. Chem. Soc.* **137,** 4976–4979 (2015).

139. Sattayasamitsathit, S. *et al.* Fully loaded micromotors for combinatorial delivery and autonomous release of cargoes. *Small Weinh. Bergstr. Ger.* **10,** 2830–2833, 2743 (2014).

140. Baraban, L., Harazim, S. M., Sanchez, S. & Schmidt, O. G. Chemotactic Behavior of Catalytic Motors in Microfluidic Channels. *Angew. Chem. Int. Ed.* **52,** 5552–5556 (2013).

141. Hong, Y., Blackman, N. M. K., Kopp, N. D., Sen, A. & Velegol, D. Chemotaxis of Nonbiological Colloidal Rods. *Phys. Rev. Lett.* **99,** 178103 (2007).

142. Peng, F., Tu, Y., van Hest, J. C. M. & Wilson, D. A. Self-Guided Supramolecular Cargo-Loaded Nanomotors with Chemotactic Behavior towards Cells. *Angew. Chem. Int. Ed.* **54,** 11662–11665 (2015).

143. Saha, S., Golestanian, R. & Ramaswamy, S. Clusters, asters, and collective oscillations in chemotactic colloids. *Phys. Rev. E* **89,** 062316 (2014).

144. Dey, K. K., Bhandari, S., Bandyopadhyay, D., Basu, S. & Chattopadhyay, A. The pH taxis of an intelligent catalytic microbot. *Small Weinh. Bergstr. Ger.* **9,** 1916–1920 (2013).

145. Kline, T. R., Paxton, W. F., Mallouk, T. E. & Sen, A. Catalytic Nanomotors: Remote-Controlled Autonomous Movement of Striped Metallic Nanorods. *Angew. Chem. Int. Ed.* **44,** 744–746 (2005).

146. Solovev, A. A., Sanchez, S., Pumera, M., Mei, Y. F. & Schmidt, O. G. Magnetic Control of Tubular Catalytic Microbots for the Transport, Assembly, and Delivery of Micro-objects. *Adv. Funct. Mater.* **20,** 2430–2435 (2010).

147. Khalil, I. S. M., Magdanz, V., Sanchez, S., Schmidt, O. G. & Misra, S. Three-dimensional closed-loop control of self-propelled microjets. *Appl. Phys. Lett.* **103,** 172404 (2013).

148. Albrecht, M. *et al.* Magnetic multilayers on nanospheres. *Nat. Mater.* **4,** 203–206 (2005).

149. Günther, C. M. *et al.* Microscopic reversal behavior of magnetically capped nanospheres. *Phys. Rev. B* **81,** 064411 (2010).

150. Baraban, L. *et al.* Catalytic Janus Motors on Microfluidic Chip: Deterministic Motion for Targeted Cargo Delivery. *ACS Nano* **6,** 3383–3389 (2012).

151. Ulbrich, T. C. *et al.* Effect of magnetic coupling on the magnetization reversal in arrays of magnetic nanocaps. *Phys. Rev. B* **81,** 054421 (2010).

152. Maggi, C. *et al.* Self-Assembly of Micromachining Systems Powered by Janus Micromotors. *Small* **12,** 446–451 (2016).

153. Golestanian, R., Liverpool, T. B. & Ajdari, A. Propulsion of a molecular machine by asymmetric distribution of reaction products. *Phys. Rev. Lett.* **94,** 220801–220801 (2005).

154. Golestanian, R. Anomalous Diffusion of Symmetric and Asymmetric Active Colloids. *Phys. Rev. Lett.* **102,** 188305 (2009).

155. Anderson, J. L. Colloid Transport by Interfacial Forces. *Annu. Rev. Fluid Mech.* **21,** 61–99 (1989).

156. Campbell, A. I. & Ebbens, S. J. Gravitaxis in spherical Janus swimming devices. *Langmuir ACS J. Surf. Colloids* **29,** 14066–14073 (2013).

157. Popescu, M. N., Dietrich, S., Tasinkevych, M. & Ralston, J. Phoretic motion of spheroidal particles due to self-generated solute gradients. *Eur. Phys. J. E Soft Matter* **31,** 351–367 (2010).

158. Tu, Z. C. Efficiency at maximum power of Feynman's ratchet as a heat engine. *J. Phys. Math. Theor.* **41,** 312003 (2008).

159. The Feynman Lectures on Physics Vol. I Ch. 46: Ratchet and pawl. Available at: http://www.feynmanlectures.caltech.edu/I_46.html. (Accessed: 17th July 2017)

160. Doering, C. R., Horsthemke, W. & Riordan, J. Nonequilibrium fluctuation-induced transport. *Phys. Rev. Lett.* **72,** 2984–2987 (1994).

161. Millonas, M. M. & Dykman, M. I. Transport and current reversal in stochastically driven ratchets. *Phys. Lett. A* **185,** 65–69 (1994).

162. Rousselet, J., Salome, L., Ajdari, A. & Prostt, J. Directional motion of brownian particles induced by a periodic asymmetric potential. *Nature* **370,** 446–447 (1994).

163. Faucheux, L. P., Bourdieu, L. S., Kaplan, P. D. & Libchaber, A. J. Optical Thermal Ratchet. *Phys. Rev. Lett.* **74,** 1504–1507 (1995).

164. Astumian, R. D. & Bier, M. Fluctuation driven ratchets: Molecular motors. *Phys. Rev. Lett.* **72,** 1766–1769 (1994).

165. Astumian, R. D. Thermodynamics and Kinetics of a Brownian Motor. *Science* **276,** 917–922 (1997).

166. Magnasco, M. O. Forced thermal ratchets. *Phys. Rev. Lett.* **71,** 1477–1481 (1993).

167. Bartussek, R., Hänggi, P. & Kissner, J. G. Periodically Rocked Thermal Ratchets. *EPL Europhys. Lett.* **28,** 459 (1994).

168. Reimann, P., Bartussek, R., Häußler, R. & Hänggi, P. Brownian motors driven by temperature oscillations. *Phys. Lett. A* **215,** 26–31 (1996).

169. Jung, P., Kissner, J. G. & Hänggi, P. Regular and Chaotic Transport in Asymmetric Periodic Potentials: Inertia Ratchets. *Phys. Rev. Lett.* **76,** 3436–3439 (1996).

170. Mateos, J. L. Chaotic Transport and Current Reversal in Deterministic Ratchets. *Phys. Rev. Lett.* **84,** 258–261 (2000).

171. Borromeo, M., Costantini, G. & Marchesoni, F. Deterministic ratchets: Route to diffusive transport. *Phys. Rev. E* **65,** 041110 (2002).

172. Marchesoni, F., Savel' ev, S. & Nori, F. Achieving optimal rectification using underdamped rocked ratchets. *Phys. Rev. E* **73,** 021102 (2006).

173. Koumakis, N., Lepore, A., Maggi, C. & Leonardo, R. D. Targeted delivery of colloids by swimming bacteria. *Nat. Commun.* **4,** ncomms3588 (2013).

174. Galajda, P., Keymer, J., Chaikin, P. & Austin, R. A Wall of Funnels Concentrates Swimming Bacteria. *J. Bacteriol.* **189,** 8704–8707 (2007).

175. Wan, M. B., Olson Reichhardt, C. J., Nussinov, Z. & Reichhardt, C. Rectification of Swimming Bacteria and Self-Driven Particle Systems by Arrays of Asymmetric Barriers. *Phys. Rev. Lett.* **101,** 018102 (2008).

176. Tailleur, J. & Cates, M. E. Sedimentation, trapping, and rectification of dilute bacteria. *EPL Europhys. Lett.* **86,** 60002 (2009).

177. Ghosh, P. K., Misko, V. R., Marchesoni, F. & Nori, F. Self-Propelled Janus Particles in a Ratchet: Numerical Simulations. *Phys. Rev. Lett.* **110,** 268301 (2013).

178. Simmchen, J. *et al.* Topographical pathways guide chemical microswimmers. *Nat. Commun.* **7,** 10598 (2016).

179. Das, S. *et al.* Boundaries can steer active Janus spheres. *Nat. Commun.* **6,** 8999 (2015).

180. Uspal, W. E., Popescu, M. N., Dietrich, S. & Tasinkevych, M. Self-propulsion of a catalytically active particle near a planar wall: from reflection to sliding and hovering. *Soft Matter* **11,** 434–438 (2014).

181. Ghosh, P. K. Communication: Escape kinetics of self-propelled Janus particles from a cavity: Numerical simulations. *J. Chem. Phys.* **141,** 061102 (2014).

182. Katuri, J., Seo, K. D., Kim, D. S. & Sanchez, S. Artificial micro-swimmers in simulated natural environments. *Lab. Chip* (2016). doi:10.1039/C6LC90022D

183. Adler, J. Chemotaxis in Bacteria. *Science* **153,** 708–716 (1966).

184. Team:Technion Israel/Chemotaxis - 2016.igem.org. Available at: http://2016.igem.org/Team:Technion_Israel/Chemotaxis. (Accessed: 31st May 2018)

185. Kohlasz21. Wikimedia: Chemotaxis Asp receptor in bacteria. (2006).

186. L, K. Wikimedia: Signaling in bacterial chemotaxis. (2006).

187. Bren, A. & Eisenbach, M. How Signals Are Heard during Bacterial Chemotaxis: Protein-Protein Interactions in Sensory Signal Propagation. *J. Bacteriol.* **182,** 6865–6873 (2000).

188. Turner, L., Ryu, W. S. & Berg, H. C. Real-Time Imaging of Fluorescent Flagellar Filaments. *J. Bacteriol.* **182,** 2793–2801 (2000).

189. Berg, H. C. & Brown, D. A. Chemotaxis in Escherichia coli analysed by Three-dimensional Tracking. *Nature* **239,** 500–504 (1972).

190. Lozano, C., ten Hagen, B., Löwen, H. & Bechinger, C. Phototaxis of synthetic microswimmers in optical landscapes. *Nat. Commun.* **7,** (2016).

191. Roberts, A. M. The mechanics of gravitaxis in Paramecium. *J. Exp. Biol.* **213,** 4158–4162 (2010).

192. Kessler, J. O. Hydrodynamic focusing of motile algal cells. *Nature* **313,** 17 (1985).

193. Hagen, B. ten *et al.* Gravitaxis of asymmetric self-propelled colloidal particles. *Nat Commun* **5,** 4829 (2014).

194. Campbell, A. I. & Ebbens, S. J. Gravitaxis in Spherical Janus Swimming Devices. *Langmuir* **29,** 14066–14073 (2013).

195. Rusconi, R. & Stocker, R. Microbes in flow. *Curr. Opin. Microbiol.* **25,** 1–8 (2015).

196. Bukatin, A., Kukhtevich, I., Stoop, N., Dunkel, J. & Kantsler, V. Bimodal rheotactic behavior reflects flagellar beat asymmetry in human sperm cells. *Proc Natl Acad Sci* **112,** 15904–15909 (2015).

197. Pedley, T. J. & Kessler, J. O. Hydrodynamic Phenomena in Suspensions of Swimming Microorganisms. *Ann Rev Fluid Mech* **24,** 313 – 358 (1992).

198. Guasto, J. S., Rusconi, R. & Stocker, R. Fluid Mechanics of Planktonic Microorganisms. *Ann Rev Fluid Mech* **44,** 373 – 400 (2012).

199. Marcos, Fu, H. C., Powers, T. R. & Stocker, R. Bacterial rheotaxis. *Proc. Natl. Acad. Sci.* **109,** 4780–4785 (2012).

200. Chengala, A., Hondzo, M. & Sheng, J. Microalga propels along vorticity direction in a shear flow. *Phys Rev E* **87,** 052704 (2013).

201. Sokolov, A. & Aranson, I. S. Rapid expulsion of microswimmers by a vortical flow. *Nat Commun* **7,** 11114 (2016).

202. Pedley, T. J. & Kessler, J. O. The orientation of spheroidal microorganisms swimming in a flow field. *Proc R Soc Lond. Ser B* **231,** 47 (1987).

203. Thorn, G. J. & Bearon, R. N. Transport of spherical gyrotactic organisms in general three-dimensional flow fields. *Phys Fluids* **22,** 041902 (2010).

204. Durham, W. H., Climent, E. & Stocker, R. Gyrotaxis in a Steady Vortical Flow. *Phys Rev Lett* **106,** 238102 (2011).

205. Durham, W. H., Kessler, J. O. & Stocker, R. Disruption of vertical motility by shear triggers formation of thin phytoplankton layers. *Science* **1067,** 323 (2009).

206. Kaya, T. & Koser, H. Direct Upstream Motility in Escherichia coli. *Biophys. J.* **102,** 1514–1523 (2012).

207. Palacci, J. *et al.* Artificial rheotaxis. *Sci. Adv.* **1,** e1400214 (2015).

208. Bretherton, F. P. & Rothschild. Rheotaxis of Spermatozoa. *Proc. R. Soc. Lond. B Biol. Sci.* **153,** 490–502 (1961).

209. Hill, J., Kalkanci, O., McMurry, J. L. & Koser, H. Hydrodynamic Surface Interactions Enable Escherichia Coli to Seek Efficient Routes to Swim Upstream. *Phys Rev Lett* **98,** 068101 (2007).

210. Kantsler, V., Dunkel, J., Blayney, M. & Goldstein, R. E. Rheotaxis facilitates upstream navigation of mammalian sperm cells. *eLife* **3,** e02403 (2014).

211. Figueroa-Morales, N. *et al.* Living on the edge: transfer and traffic of E. coli in a confined flow. *Soft Matter* **11,** 6284–6293 (2015).

212. Omori, T. & Ishikawa, T. Upward swimming of a sperm cell in shear flow. *Phys Rev E* **93,** 032402 (2016).

213. Bianchi, S., Saglimbeni, F. & Di Leonardo, R. Holographic Imaging Reveals the Mechanism of Wall Entrapment in Swimming Bacteria. *Phys. Rev. X* **7,** 011010 (2017).

214. Sipos, O., Nagy, K., Di Leonardo, R. & Galajda, P. Hydrodynamic Trapping of Swimming Bacteria by Convex Walls. *Phys. Rev. Lett.* **114,** 258104 (2015).

215. Schaar, K., Zöttl, A. & Stark, H. Detention Times of Microswimmers Close to Surfaces: Influence of Hydrodynamic Interactions and Noise. *Phys. Rev. Lett.* **115,** 038101 (2015).

216. Shen, Y., Siryaporn, A., Lecuyer, S., Gitai, Z. & Stone, H. A. Flow Directs Surface-Attached Bacteria to Twitch Upstream. *Biophys. J.* **103,** 146–151 (2012).

217. Golestanian, R., Liverpool, T. B. & Ajdari, A. Designing phoretic micro- and nano-swimmers. *New J Phys* **9,** 126 (2007).

218. Brown, A. & Poon, W. Ionic effects in self-propelled Pt-coated Janus swimmers. *Soft Matter* **10,** 4016–4027 (2014).

219. Brown, A. T., Poon, W. C. K., Holm, C. & Graaf, J. de. Ionic screening and dissociation are crucial for understanding chemical self-propulsion in polar solvents. *Soft Matter* **13,** 1200–1222 (2017).

220. Brown, A. T. *et al.* Swimming in a crystal. *Soft Matter* **12,** 131–140 (2015).

221. Ebbens, S. *et al.* Electrokinetic effects in catalytic platinum-insulator Janus swimmers. *EPL Europhys. Lett.* **106,** 58003 (2014).

222. Bruus, H. *Theoretical Microfluidics*. (Oxford University Press, 2008).

223. Uspal, W. E., Popescu, M. N., Dietrich, S. & Tasinkevych, M. Rheotaxis of spherical active particles near a planar wall. *Soft Matter* **11,** 6613–6632 (2015).

224. Goldman, A. J., Cox, R. G. & Brenner, H. Slow viscous motion of a sphere parallel to a plane wall–II Couette Flow. *Chem Eng Sci* **22,** 653 – 660 (1967).

225. Mozaffari, A., Sharifi-Mood, N., Koplik, J. & Maldarelli, C. Self-diffusiophoretic colloidal propulsion near a solid boundary. *Phys Fluids* **28,** 053107 (2016).

226. Ibrahim, Y. & Liverpool, T. B. How walls affect the dynamics of self-phoretic microswimmers. *Eur Phys J Spec. Top.* **225,** 1843–1874 (2016).

227. Pozrikidis, C. A Practical Guide to Boundary Element Methods with the Software Library BEMLIB. (CRC Press, 2002).

228. Michelin, S. & Lauga, E. Phoretic self-propulsion at finite Péclet numbers. *J Fluid Mech* **747,** 572–604 (2014).

229. Popescu, M. N., Dietrich, S., Tasinkevych, M. & Ralston, J. Phoretic motion of spheroidal particles due to self-generated solute gradients. *Eur Phys J E* **31,** 351–367 (2010).

230. Armitage, J. P. Bacterial Tactic Responses. in *Advances in Microbial Physiology* (ed. Poole, R. K.) **41,** 229–289 (Academic Press, 1999).

231. Conrad, J. C. Physics of bacterial near-surface motility using flagella and type IV pili: implications for biofilm formation. *Res. Microbiol.* **163,** 619–629 (2012).

232. Schmidt, J. A. & Eckert, R. Calcium couples flagellar reversal to photostimulation in Chlamydomonas reinhardtii. *Nature* **262,** 713–715 (1976).

233. Roberts, A. M. & Deacon, F. M. Gravitaxis in motile micro-organisms: the role of fore–aft body asymmetry. *J Fluid Mech* **452,** 405–423 (2002).

234. Vigeant, M. A.-S., Ford, R. M., Wagner, M. & Tamm, L. K. Reversible and Irreversible Adhesion of Motile Escherichia coli Cells Analyzed by Total Internal Reflection Aqueous Fluorescence Microscopy. *Appl. Environ. Microbiol.* **68,** 2794–2801 (2002).

235. Kantsler, V., Dunkel, J., Polin, M. & Goldstein, R. E. Ciliary contact interactions dominate surface scattering of swimming eukaryotes. *Proc. Natl. Acad. Sci.* **110,** 1187–1192 (2013).

236. Uspal, W. E., Popescu, M. N., Dietrich, S. & Tasinkevych, M. Guiding Catalytically Active Particles with Chemically Patterned Surfaces. *Phys. Rev. Lett.* **117,** 048002 (2016).

237. Popescu, M. N., Uspal, W. E. & Dietrich, S. Chemically active colloids near osmotic-responsive walls with surface-chemistry gradients. *J. Phys. Condens. Matter* **29,** 134001 (2017).

238. Li, B., Zhou, D. & Han, Y. Assembly and phase transitions of colloidal crystals. *Nat. Rev. Mater.* **1,** 15011 (2016).

239. van Dommelen, R., Fanzio, P. & Sasso, L. Surface self-assembly of colloidal crystals for micro- and nano-patterning. *Adv. Colloid Interface Sci.* **251,** 97–114 (2018).

240. Katuri, J., Uspal, W. E., Simmchen, J., Miguel-López, A. & Sánchez, S. Cross-stream migration of active particles. *Sci. Adv.* **4,** eaao1755 (2018).

241. Dai, B. *et al.* Programmable artificial phototactic microswimmer. *Nat. Nanotechnol.* **11,** 1087–1092 (2016).

242. Wang, X., In, M., Blanc, C., Nobili, M. & Stocco, A. Enhanced active motion of Janus colloids at the water surface. *Soft Matter* **11,** 7376–7384 (2015).

243. Dietrich, K. *et al.* Two-dimensional nature of the active Brownian motion of catalytic microswimmers at solid and liquid interfaces. *New J. Phys.* **19,** 065008 (2017).